UNIVERSIDAD NACIONAL AUTÓNOMA DE MÉXICO

Maestría en Ciencias (Física)

Estudio Experimental y Teórico de la Transición de Dos Fotones
$5S_{1/2} \rightarrow 5P_{1/2} \rightarrow 5D_{5/2}$ en Átomos Fríos de Rubidio

Tesis
QUE PARA OPTAR POR EL GRADO DE:
MAESTRO EN CIENCIAS (FÍSICA)

PRESENTA:
OSCAR GERARDO LAZO ARJONA

TUTOR: FERNANDO RAMÍREZ MARTÍNEZ
INSTITUTO DE CIENCIAS NUCLEARES

MÉXICO, D. F. ABRIL 2016

Experimental and Theoretical Study of the Two-Photon Transition $5S_{1/2} \rightarrow 5P_{3/2} \rightarrow 5D_{5/2}$ in Cold Rubidium Atoms

by

Oscar Gerardo Lazo Arjona

To be submitted to the
Posgrado en Ciencias Físicas of the
National Autonomous University of Mexico
as part of the requirements for the degree of
Mestro en Ciencias (Física)

Abstract

En este trabajo se presenta un sistema experimental para medir espectros de fluorescencia espontánea generada a partir de la excitación de dos fotones $5S_{1/2} \rightarrow 5P_{3/2} \rightarrow 5D_{5/2}$ en átomos fríos en una trampa magneto-óptica (MOT). Estos espectros se obtienen como función de la desintonía de la segunda excitación con respecto a la resonancia atómica, y muestran la estructura hiperfina del multiplete $5D_{5/2}$. También se presenta un modelo basado en la evolución temporal de la matriz de densidad de un sistema atómico multinivel interactuando con múltiples componentes de radiación, y se usa para calcular espectros teóricos utilizando los parámetros experimentales como entradas. Los espectros experimentales y teóricos obtenidos en un rango de parámetros coinciden dentro del error experimental. Gracias a este buen acuerdo, la inspección cuidadosa de los resultados obtenidos mediante el análisis teórico permite extraer información detallada tanto de la dinámica atómica como de la variación de los parámetros experimentales, como la amplitud del campo eléctrico y la desintonía. Estas variaciones de los parámetros experimentales están más allá de la resolución de lo que los errores asociados a los aparatos de medición permiten. A partir de este análisis es posible separar diferentes componentes del ancho de las líneas espectrales y usar el ancho Doppler para estimar la temperatura de la nube atómica.

Thesis Supervisor: Dr. Fernando Ramírez Martínez
Title: Associate Professor

Experimental and Theoretical Study of the Two-Photon Transition $5S_{1/2} \rightarrow 5P_{3/2} \rightarrow 5D_{5/2}$ in Cold Rubidium Atoms

by

Oscar Gerardo Lazo Arjona

To be submitted to the
Posgrado en Ciencias Físicas of the
National Autonomous University of Mexico
as part of the requirements for the degree of
Mestro en Ciencias (Física)

Abstract

An experimental system to measure spontaneous fluorescence spectra generated as a result of the $5S_{1/2} \rightarrow 5P_{3/2} \rightarrow 5D_{5/2}$ two-photon excitation in rubidium atoms in a magneto-optical trap (MOT) is presented. These spectra are obtained as a function of the second-excitation detuning respect o the atomic resonance, and exhibit the hyperfine structure of the $5D_{5/2}$ multiplet. A theoretical model based on the time evolution of the density matrix of a multilevel atomic system interacting with multiple radiation components is presented and used to calculate theoretical spectra with the experiment parameters as input. The experimental and theoretical spectra are obtained through a range of parameters and found to agree to within experimental error. Thanks to this good agreement, a careful inspection of the results obtained through the theoretical analysis allows detailed information to be extracted about both the atomic dynamics and the variation of experimental parameters like the electric field amplitude and the detuning. This variations of the experimental parameters are beyond the resolution that the errors associated to the measurement apparatus allow. This analysis allows different components of the spectral linewidths to be separated, and to use the Doppler width to estimate the temperature of atomic cloud.

Thesis Supervisor: Dr. Fernando Ramírez Martínez
Title: Associate Professor

Contents

Chapter 1

Introduction

1.1 Previous Developments

Spectroscopy, the study of light absorption and emission by matter (and specially its dependance on the frequency of the radiation field) has been at the forefront of atomic physics since the fluorescence spectrum of hydrogen was first observed in the XIX century [22, 74]. This was before even the existence of atoms had been well established by Einstein in his 1905 article on Brownian motion [18]. The study of the fluorescence spectra of elements led to the development in 1913 of the Bohr model [51, 52], which was the first approximation to a quantum theory of atoms.

Through the XX century fluorescence and absorption spectroscopy was used to discover and eventually explain the fine and hyperfine structure of atoms. In particular, the invention of the laser in 1958 [62], and the subsequent development of single-mode and narrow-linewidth lasers provided the tools for developing high-precision laser spectroscopy techniques for atomic and molecular vapours beyond the Doppler broadening limit relying on ingenious techniques such as saturated absorption by counter-propagating pump and probe beams [28, 67]. These experiments were later used to develop laser frequency stabilization techniques [11]. Spectroscopies based on polarization-dependant non-linearities [73] and stabilization techniques based on them [50] followed.

Before these high-precision methods were established however, Autler and Townes discovered the splitting of spectral lines in carbonyl sulfide (OCS) due to the interaction with intense and rapidly varying radio-frequency electromagnetic fields [4]. It is now well known that this effect, called *Autler-Townes Splitting* (ATS), is a dynamic Stark effect by the electromagnetic field.

Another important effect was theoretically predicted in [29] after noticing that the dressed states produced by ATS were analogous to auto ionizing Fano states that had previously been observed to exhibit destructive interference. The interference between excitation paths to dressed states were predicted to inhibit the first order susceptibility while enhancing the third order susceptibility of

optically thick media. This phenomenon, known as Electromagnetically Induced Transparency (EIT) was first observed in strontium [8]. These are coherent effects in the sense that their description requires the preservation of information in the phases between state amplitudes. In other words, these are quantum phenomena, and require a state vector or density matrix treatment. The distinction and interpretation of ATS and EIT is developed theoretically in [20] and experimentally in [77].

The discovery of EIT together with high-precision spectroscopy prompted a cascade of experiments, theory developments and applications of two-photon spectroscopies for alkali atoms spanning from the early 1990s to this day. Early examples include the use of a single 778 nm laser to non-resonantly excite the $5S_{1/2} \rightarrow 5P_{3/2} \rightarrow 5D_{5/2}$ transition in rubidium [57], and more complete and practical theoretical descriptions of EIT [23,24]. Applications include slow light [75], absolute optical frequency measurement [40,68], and frequency up-conversion [1,43].

One of the configurations studied throughout this period has been fluorescence spectroscopy of the $5S_{1/2} \rightarrow 5P_{3/2} \rightarrow 5D_{5/2}$ two-photon transition driven by two close-to-resonant laser fields. An easy to detect fluorescence wavelength commonly measured in these experiments is the visible 420 nm from the $6P_{3/2} \rightarrow 5S_{1/2}$ decay. The spontaneous fluorescence of this transition was used to study the broadening effects of collisions due to different atomic densities [27]. In contrast, the stimulated emission was used to produce spectra of the $5P_{3/2}$ multiplet [59]. A combined measurement of absorption and spontaneous fluorescence was developed in [39]. All of these two-photon experiments were performed in room-temperature vapour cells.

Trapping devices based on the electromagnetic interaction of charged particles (such as the Paul trap [49] and the Penning trap [42], [48]) were developed as early 1946 and 1959. However, trapping neutral species was not achieved until much later. The cooling of neutral sodium atoms by the optical molasses technique was first demonstrated in 1985 [15], and the first example of an optical dipole trap by an intensely focused laser shortly after [14]. The most widely adopted trap for neutral atoms employs both optical and magnetic fields and is known as the magneto-optical trap (MOT), first demonstrated in 1987 [54]. The MOT has the advantage of not being very sensitive to errors in the power balancing of counter-propagating beams or their polarization. Another advantage is that they are capable of easily cooling and trapping of the order of 10^6 atoms directly from a vapour at room temperature and reach temperatures below 1 mK. The use of low cost diode lasers is also a common reason of choice for this method for some alkali atoms [63].

Using cold atoms to measure spectroscopic phenomena allows a better control of the internal and movement states of atoms, and the corresponding spectroscopies do not directly require the room-temperature sub-Doppler techniques mentioned above. Early examples of this approach include the 1997 studies by Catalioti et al [12,13] on cesium lambda and ladder systems observing ATS and EIT. The first of these involve the use of a high power pump laser to obtain extreme ATS that resolves the various magnetic level paths through their different ATS couplings. EIT in a rubidium lambda

system was reported shortly after in [35].

The 2005 study [40] of the $5S_{1/2} \rightarrow 5P_{3/2} \rightarrow 5P_{5/2}$ in cold rubidium atoms through 420 nm spontaneous fluorescence is particularly close to this thesis. This work measures the absolute frequencies of transitions using a frequency comb. The 2015 study [35] makes use of this same spectroscopy to measure effective Rabi frequencies associated to the field that couples the first step excitation.

1.2 Contribution

The Cold Atoms Laboratory of the Institute for Nuclear Science (LAF-ICN) has studied this transition both through absorption and spontaneous fluorescence and observed both EIT and ATS as described in [39]. Mastering this experiments is a requirement to complete a three photon spectroscopy $5S_{1/2} \rightarrow 5P_{3/2} \rightarrow 5D_{5/2} \rightarrow NP_J, NF_J$ aimed at high-N Rydberg states. A review of the properties of Rydberg atoms (and in particular cold Rydberg atoms) and their applications can be found in [38], and recent work in this direction in the LAF-ICN is detailed in [31].

An extensive characterization of the MOT in the LAF-ICN is made in [61]. The next natural step in this direction is to **implement a spectroscopy of the $5S_{1/2} \rightarrow 5P_{3/2} \rightarrow 5D_{5/2}$ two-photon transition in cold rubidium atoms**, and this is the objective of this thesis.

All previously reported cold atom spectroscopies have been realized in the absence of all MOT optical and magnetic fields. This requires the use of elaborate time sequences to cool and trap atoms, release them, perform measurements in time lapses of the order of μs, and record the results. A much simpler scheme with the MOT fields in continuous operation is developed in this thesis, with spectroscopies realized in approximately 160 ms. The main reason to turn off the MOT fields in previous studies is that the theoretical treatment of the excitations (particularly for the coherent phenomena of interest) is more complicated in the presence of the many fields the MOT requires.

In this thesis, the density matrix dynamics of the complete hyperfine and magnetic structure of the rubidium atom states participating in these processes is calculated according to optical Bloch equations. To the best of my knowledge this extensive calculation has never been done before, and neither has the corresponding generalized theory been published. Related software has been developed for smaller systems [56], and it is my intention to similarly release my implementation for public use.

1.3 On this thesis

Chapter 2 develops the theory of generalized optical Bloch equations from first principles. These are the dynamic equations of the density matrix of an arbitrary number of atomic states driven by an arbitrary number of classical light fields. Optical Bloch equations are well suited to describe

coherent phenomena in atomic physics while considering the spontaneous decay of excited states without a more complicated quantum electrodynamic treatment. In other words, they are the simplest equations that can describe the spectra that concern this thesis. Two simple examples are presented: the two level system, that is useful in describing the cooling mechanism; and the three level ladder system that is the simplest system that can qualitatively describe the spectra in this thesis.

Chapter 3 deals with the application of these equations to rubidium. The hyperfine structure of the atomic states is obtained from a combination of theory and experiment. The light-atom interaction hamiltonian is calculated from measurements of the life times of the fine-structure multiplets, as well as the decay rates among pairs of magnetic states (the branching ratios in magnetic detail). The calculation of theoretical fluorescence spectra is also explained in this chapter.

A description of the physics underlying the magneto-optical trap is given in chapter 4 from the point of view of optical Bloch equations. The optical molasses technique, the Doppler cooling limit, and the role of the magnetic field are explained and the propper configuration of all components is presented.

The experimental realization of the $5S_{1/2} \rightarrow 5P_{3/2} \rightarrow 5D_{5/2}$ two-photon spectroscopy in cold atoms is described in chapter 5. The MOT is used to cool and trap both ^{85}Rb and ^{87}Rb, and a probe beam is used to produce the second step excitation. The excited states in $5D5/2$ spontaneously decay to $6P_{3/2}$ states, and the fluorescence from the decay $6P_{3/2} \rightarrow 5S_{1/2}$ is recorded in a photomultiplier tube as a function of the frequency of the probe beam. All measurements performed are explained in detail, as well as the experimental errors associated to these measurements and how they are used to complete the parameters that the optical Bloch equations require.

The physical quantities obtained in chapters 3 and 5 are then introduced to the equations derived in chapter 2. The software and hardware used to solve these equations is described in chapter 6. Approximations to reduce the complexity of the equations are presented and justified. A procedure to fit the model to the experimental data is presented, and an error associated to the fit is defined.

The combined experimental and theoretical results are discussed in chapter 7. The power and detuning of the first step transition are varied to observe the dependance of the spectra on those parameters. Two models are used to describe the resulting spectra: the three level ladder system derived in chapter 2, and the model describing the complete structure of the atom. The spectra obtained from the numerical simulations are compared to the experimental spectra, and a theoretical interpretation of the variations of the spectra is given using the model.

Lastly, conclusions and perspectives for future work are presented in chapter 8.

Chapter 2

Optical Bloch Equations

The purpose of this chapter is to develop the dynamic equations for the quantum state of a generic alkali atom as described by the density matrix $\hat{\rho}$ of the internal states. The Hamiltonian that describes the interaction between the atom and electromagnetic fields is derived, followed by the equations it induces from the Liouville-von Neumann equation under several useful approximations. The dissipation Lindblad terms are also derived for spontaneous decay. This results in *generalized optical Bloch equations*. The equations for two simple systems of interest are obtained explicitly and examined.

2.1 The Interaction Hamiltonian

Let us consider a hydrogen-like atom whose nucleus (together with the filled orbitals) has mass m_n and position $\vec{r}_n$ with respect to an arbitrary origin and the electron has mass m_e and position $\vec{r}_e$. The position $\vec{R}$ of the centre of mass and the position $\vec{r}$ of the electron relative to the nucleus are

$$\vec{R} = \frac{m_n\vec{r}_n + m_e\vec{r}_e}{m_n + m_e}, \qquad \vec{r} = \vec{r}_e - \vec{r}_n.$$

and conversely

$$\vec{r}_n = \vec{R} - \frac{m_e}{m_e + m_n}\vec{r}, \qquad \vec{r}_e = \vec{R} + \frac{m_n}{m_e + m_n}\vec{r}.$$

This can be written as a coordinate transformation $q^{i'} = \sum_i \Lambda_i^{i'} q^i$ and $q^i = \sum_{i'} \Lambda_{i'}^i q^{i'}$. Where the components of the direct and inverse transformation are respectively

$$\Lambda_i^{i'} = \begin{pmatrix} \frac{m_n}{m_n+m_e} & \frac{m_e}{m_n+m_e} \\ -1 & 1 \end{pmatrix}, \qquad \Lambda_{i'}^i = \begin{pmatrix} 1 & -\frac{m_e}{m_n+m_e} \\ 1 & \frac{m_n}{m_n+m_e} \end{pmatrix}.$$

The classical Lagrangian of this system (without external electromagnetic fields) can be expressed in these coordinate systems in the following way

$$L_0 = \frac{m_n \dot{\vec{r}}_n^2}{2} + \frac{m_e \dot{\vec{r}}_e^2}{2} - V(\vec{r}_n, \vec{r}_e) = \frac{M\dot{\vec{R}}^2}{2} + \frac{\mu \dot{\vec{r}}^2}{2} - V(\vec{r}),$$

where $M = m_n + m_e$ is the total mass of the atom, $\mu = m_n m_e/(m_n + m_e)$ is the reduced mass, and $V(\vec{r}_n, \vec{r}_e) = V(\vec{r})$ is the interaction potential between the nucleus and the outer electron. The generalized momenta in each coordinate system are $p_i \equiv \partial L_0/\partial \dot{q}^i$, that is

$$\vec{p}_n = m_n \dot{\vec{r}}_n, \qquad \vec{p}_e = m_e \dot{\vec{r}}_e, \qquad \vec{P} = M\dot{\vec{R}}, \qquad \vec{p} = \mu \dot{\vec{r}}.$$

The relation between generalized momenta in the different coordinates are $p_{i'} = \sum_i \Lambda^i_{i'} p_i$ and $p_i = \sum_{i'} \Lambda^{i'}_i p_{i'}$, that is

$$\vec{P} = \vec{p}_n + \vec{p}_e, \qquad \vec{p} = \frac{m_e}{m_n + m_e}\vec{p}_n + \frac{m_n}{m_n + m_e}\vec{p}_e,$$

$$\vec{p}_n = \frac{m_n}{m_n + m_e}\vec{P} - \vec{p}, \qquad \vec{p}_e = \frac{m_e}{m_n + m_e}\vec{P} + \vec{p}.$$

The corresponding Hamiltonian can be calculated as $H_0 = \sum_i \dot{q}^i p_i - L_0(p_i, q^i)$

$$H_0 = \frac{\vec{p}_n^2}{2m_n} + \frac{\vec{p}_e^2}{2m_e} + V(\vec{r}_n, \vec{r}_e) = \frac{\vec{P}^2}{2M} + \frac{\vec{p}^2}{2\mu} + V(\vec{r}).$$

The classical prescription to obtain the Hamiltonian of a charged particle is to replace $H \to H + q\phi$, and $\vec{p} \to \vec{p} - q\vec{A}$ where ϕ and $\vec{A}$ are the scalar and vector potentials respectively. This is known as [**?**] schleich2011quantum and it also works in quantum mechanics. Promoting the Hamiltonian to a linear operator acting on the Hilbert space of the quantum system (all of these operators are denoted with a circumflex ˆ), we obtain the Hamiltonian operator of our quantum system.

$$\begin{aligned}
\hat{H} &= \frac{(\widehat{\vec{p}}_n - e\widehat{\vec{A}}(\vec{r}_n, t))^2}{2m_n} + \frac{(\widehat{\vec{p}}_e + e\widehat{\vec{A}}(\vec{r}_e, t))^2}{2m_e} + V(\vec{r}_n, \vec{r}_e) - e\hat{\phi}(\vec{r}_n) + e\hat{\phi}(\vec{r}_e) \\
&= \frac{\widehat{\vec{p}}_n^2}{2m_n} - \frac{e\widehat{\vec{p}}_n \cdot \widehat{\vec{A}}(\vec{r}_n) + e\widehat{\vec{A}}(\vec{r}_n) \cdot \widehat{\vec{p}}_n}{2m_n} + \frac{e^2\widehat{\vec{A}}(\vec{r}_n)^2}{2m_n} - e\hat{\phi}(\vec{r}_n) \\
&+ \frac{\widehat{\vec{p}}_e^2}{2m_e} + \frac{e\widehat{\vec{p}}_e \cdot \widehat{\vec{A}}(\vec{r}_e) + e\widehat{\vec{A}}(\vec{r}_e) \cdot \widehat{\vec{p}}_e}{2m_e} + \frac{e^2\widehat{\vec{A}}(\vec{r}_e)^2}{2m_e} + e\hat{\phi}(\vec{r}_e) + V(\vec{r}_n, \vec{r}_e)
\end{aligned}$$

In the Coulomb gauge $\nabla \cdot \vec{A} = 0$ and in the absence of sources $\phi = 0$, and therefore $\widehat{\vec{p}} \cdot (\widehat{\vec{A}}\psi) = \psi(\widehat{\vec{p}} \cdot \widehat{\vec{A}}) + \widehat{\vec{A}} \cdot (\widehat{\vec{p}}\psi) = \widehat{\vec{A}} \cdot (\widehat{\vec{p}}\psi)$, that is $\widehat{\vec{p}} \cdot \widehat{\vec{A}}(\vec{r}) = \widehat{\vec{A}}(\vec{r}) \cdot \widehat{\vec{p}}$. The terms with $\widehat{\vec{A}}^2$ are proportional to $e^2 = 4\pi\varepsilon_0\hbar c\alpha$, where α is the fine-structure constant. In Plank units this is $e^2 = \alpha \simeq 1/137$, which

allows us to dismiss these terms, and therefore the Hamiltonian is reduced to

$$\hat{H} \simeq \frac{\widehat{\vec{p}}_n^{\,2}}{2m_n} + \frac{\widehat{\vec{p}}_e^{\,2}}{2m_e} + V(\vec{r}_n, \vec{r}_e) - \frac{e\widehat{\vec{A}}(\vec{r}_n)\cdot\widehat{\vec{p}}_n}{m_n} + \frac{e\widehat{\vec{A}}(\vec{r}_e)\cdot\widehat{\vec{p}}_e}{m_e}.$$

The term with $\widehat{\vec{A}}(\vec{r}_n)\cdot\widehat{\vec{p}}_n$ is proportional to $1/m_n$, and the term with $\widehat{\vec{A}}(\vec{r}_e)\cdot\widehat{\vec{p}}_e$ is proportional to $1/m_e$. In table 2.1 the ratios between these factors are shown for alkali atoms.

	m_e/m_n	M (kg)
H	5.4452×10^{-4}	1.6738×10^{-27}
Li	7.9052×10^{-5}	1.1524×10^{-26}
Na	2.3862×10^{-5}	3.8176×10^{-26}
K	1.4030×10^{-5}	6.4928×10^{-26}
Rb	6.4184×10^{-6}	1.4192×10^{-25}
Cs	4.1274×10^{-6}	2.2070×10^{-25}
Fr	2.4597×10^{-6}	3.7034×10^{-25}

Table 2.1: Mass ratios for alkali atoms.

If the variations of the field are small through the extension of the atom (which is of the order of 1nm) then $\widehat{\vec{A}}(\vec{r}_n)$ and $\widehat{\vec{A}}(\vec{r}_e)$ are of the same order of magnitude. If we replace the velocities $\vec{v}_{\rm cm} \equiv \vec{P}/M$ and $\vec{v}_{\rm rel} \equiv \vec{p}/\mu$ of the mass centre and the relative distance in the momenta we obtain

$$\begin{aligned}
\frac{\vec{p}_n}{m_n} &= \frac{1}{m_n}\left(\frac{m_n}{m_n+m_e}\vec{P} - \vec{p}\right) = \vec{v}_{\rm cm} - \vec{v}_{\rm rel}\frac{m_e}{m_n+m_e} \simeq \vec{v}_{\rm cm} \\
\frac{\vec{p}_e}{m_e} &= \frac{1}{m_e}\left(\frac{m_e}{m_n+m_e}\vec{P} + \vec{p}\right) = \vec{v}_{\rm cm} + \vec{v}_{\rm rel}\frac{m_n}{m_n+m_e} \simeq \vec{v}_{\rm rel}
\end{aligned}$$

Where approximations have been made considering the mass ratios and the fact that at room temperature $\vec{v}_{\rm cm} \approx 300m/s$, while $\vec{v}_{\rm rel}$ is comparable to the speed of light. This way the term $\widehat{\vec{A}}(\vec{r}_n)\cdot\widehat{\vec{p}}_n/m_n$ is much smaller than $\widehat{\vec{A}}(\vec{r}_e)\cdot\widehat{\vec{p}}_e/m_e$, and we can write the Hamiltonian as

$$\begin{aligned}
\hat{H} &\simeq \frac{\widehat{\vec{p}}_n^{\,2}}{2m_n} + \frac{\widehat{\vec{p}}_e^{\,2}}{2m_e} + V(\vec{r}_n, \vec{r}_e) + \frac{e\widehat{\vec{A}}(\vec{r}_e)\cdot\widehat{\vec{p}}_e}{m_e} \\
&= \frac{\widehat{\vec{P}}^{\,2}}{2M} + \frac{\widehat{\vec{p}}^{\,2}}{2\mu} + V(\vec{r}) + \frac{e\widehat{\vec{A}}(\vec{r}_e)\cdot\widehat{\vec{P}}}{M} + \frac{e\widehat{\vec{A}}(\vec{r}_e)\cdot\widehat{\vec{p}}}{m_e}.
\end{aligned}$$

Once more, since $M \gg m_e$ we get

$$\hat{H} \simeq \frac{\widehat{\vec{P}}^{\,2}}{2M} + \frac{\widehat{\vec{p}}^{\,2}}{2\mu} + V(\vec{r}) + \frac{e\widehat{\vec{A}}(\vec{r}_e)\cdot\widehat{\vec{p}}}{m_e} = \hat{H}_0 + \frac{e\widehat{\vec{A}}(\vec{r}_e)\cdot\widehat{\vec{p}}}{m_e}.$$

2.1.1 Multipole Expansion

For a completely general vector potential, taking the Fourier transform [33]

$$\begin{aligned}
\vec{A}(\vec{r}_e,t) &= \int \widetilde{\vec{A}}(\vec{k},t)e^{i\vec{k}\cdot\vec{r}_e}d^3k \\
&= \int \widetilde{\vec{A}}(\vec{k},t)e^{i\vec{k}\cdot\vec{R}}e^{i\vec{k}\cdot\vec{r}\frac{\mu}{m_e}}d^3k \\
&= \int \widetilde{\vec{A}}(\vec{k},t)e^{i\vec{k}\cdot\vec{R}}\left[\sum_{n=0}^{\infty}\frac{1}{n!}\left(\frac{\mu}{m_e}i\vec{k}\cdot\vec{r}\right)^n\right]d^3k \\
&= \int \widetilde{\vec{A}}(\vec{k},t)e^{i\vec{k}\cdot\vec{R}}\left[\sum_{n=0}^{\infty}\frac{1}{n!}\left(\frac{\mu}{m_e}i(k_xx+k_yy+k_zz)\right)^n\right]d^3k \\
&= \int \widetilde{\vec{A}}(\vec{k},t)e^{i\vec{k}\cdot\vec{R}}\left[\sum_{n=0}^{\infty}\frac{1}{n!}\frac{\mu^n}{m_e^n}i^n\left(\sum_{\substack{i,\,j,\,k\\ a+b+c=n}}\frac{n!}{a!b!c!}(k_xx)^a(k_yy)^b(k_zz)^c\right)\right]d^3k \\
&= \sum_{n=0}^{\infty}\frac{\mu^n}{m_e^n}\sum_{\substack{a,\,b,\,c\\ a+b+c=n}}\frac{x^ay^bz^c}{a!b!c!}\int i^nk_x^ak_y^bk_z^c\widetilde{\vec{A}}(\vec{k},t)e^{i\vec{k}\cdot\vec{R}}d^3k.
\end{aligned}$$

For an infinitely differentiable function $f(x)$, the Fourier transform of the derivatives satisfies $\widetilde{f^{(n)}}(k) = (ik)^n\tilde{f}(k)$, therefore

$$\frac{\partial^n f(x)}{\partial x^n} = \int (ik)^n\tilde{f}(k)e^{ikx}dk.$$

Applying this to the vector field we get

$$\vec{A}(\vec{r}_e,t) = \sum_{n=0}^{\infty}\frac{\mu^n}{m_e^n}\sum_{\substack{a,\,b,\,c\\ a+b+c=n}}\frac{x^ay^bz^c}{a!b!c!}\frac{\partial^n}{\partial X^a\partial Y^b\partial Z^c}\vec{A}(\vec{R},t)$$

The first few terms of this series are

$$\begin{aligned}
\vec{A}_0 &= \vec{A}(\vec{R},t) \\
\vec{A}_1 &= \frac{\mu}{m_e}\left[\hat{x}\frac{\partial}{\partial X}\vec{A}(\vec{R},t) + \hat{y}\frac{\partial}{\partial Y}\vec{A}(\vec{R},t) + \hat{z}\frac{\partial}{\partial Z}\vec{A}(\vec{R},t)\right] \\
&= \frac{\mu}{m_e}\sum_{j=1}^{3}\hat{r}_j\frac{\partial}{\partial R_j}\vec{A}(\vec{R},t) \\
\vec{A}_2 &= \frac{\mu^2}{m_e^2}\left[\frac{x^2}{2}\frac{\partial^2}{\partial X^2}\vec{A}(\vec{R},t) + \frac{y^2}{2}\frac{\partial^2}{\partial Y^2}\vec{A}(\vec{R},t) + \frac{z^2}{2}\frac{\partial^2}{\partial Z^2}\vec{A}(\vec{R},t)\right. \\
&\qquad \left. + yz\frac{\partial^2}{\partial Y\partial Z}\vec{A}(\vec{R},t) + xz\frac{\partial^2}{\partial X\partial Z}\vec{A}(\vec{R},t) + xy\frac{\partial^2}{\partial X\partial Y}\vec{A}(\vec{R},t)\right]
\end{aligned}$$

In this work I will develop the time evolution equations of the system approximating $\vec{A}(\vec{r}_e, t) \simeq \vec{A}_0 = \vec{A}(\vec{R}, t)$. This is known as the *electric-dipole approximation*. In this way, the Hamiltonian becomes

$$\hat{H} \simeq \frac{\widehat{\vec{P}}^2}{2M} + \frac{\widehat{\vec{p}}^2}{2\mu} + \frac{e\vec{A}(\vec{R}, t) \cdot \widehat{\vec{p}}}{m_e}.$$

We can write the interaction Hamiltonian in terms of the $\widehat{\vec{r}}$ operator instead of the $\widehat{\vec{p}}$ operator considering that

$$\widehat{\vec{p}} = \frac{1}{i\hbar}[\widehat{\vec{r}}, \widehat{\vec{p}}]\widehat{\vec{p}} = \frac{1}{2i\hbar}[\widehat{\vec{r}}, \widehat{\vec{p}}^2] = \frac{\mu}{i\hbar}\left[\widehat{\vec{r}}, \frac{\widehat{\vec{p}}^2}{2\mu}\right] = \frac{\mu}{i\hbar}\left[\widehat{\vec{r}}, \frac{\widehat{\vec{p}}^2}{2\mu} + \frac{\widehat{\vec{P}}^2}{2M} + \hat{V}_0(\vec{r})\right] = \frac{i\mu}{\hbar}[\hat{H}_0, \widehat{\vec{r}}],$$

where the fact that $\hat{P}$ and $\hat{V}_0$ commute with $\widehat{\vec{r}}$ has been used.

From now on we will use the base $|i\rangle$ of the eigenstates of the $\hat{H}_0$ Hamiltonian (with eigenvalues $\hbar\omega_i$). We will limit the number of eigenstates to N_e and consider any unused states not to contriubute to the overall state $|\psi\rangle$ at any time. Using this basis to calculate the matrix elements of the Hamiltonian, we get

$$\begin{aligned}
H_{ij} &= \langle i|\hat{H}_0|j\rangle + \frac{ie\mu}{m_e\hbar}\vec{A}(\vec{R}, t) \cdot \langle i|[\hat{H}_0, \widehat{\vec{r}}]|j\rangle \\
&= \hbar\omega_i\delta_{ij} + \frac{ie\mu}{m_e\hbar}\vec{A}(\vec{R}, t) \cdot \langle i|\hat{H}_0\widehat{\vec{r}} - \widehat{\vec{r}}\hat{H}_0|j\rangle \\
&= \hbar\omega_i\delta_{ij} + \frac{ie\mu}{m_e\hbar}\vec{A}(\vec{R}, t) \cdot \left[\hbar\omega_i\langle i|\widehat{\vec{r}}|j\rangle - \hbar\omega_j\langle i|\widehat{\vec{r}}|j\rangle\right] \\
&= \hbar\omega_i\delta_{ij} + \frac{ie\mu}{m_e}\vec{A}(\vec{R}, t) \cdot \langle i|\widehat{\vec{r}}|j\rangle\omega_{ij}.
\end{aligned}$$

Where we have defined $\omega_{ij} \equiv \omega_i - \omega_j$. If we take the Fourier transform of the vector potential we get

$$\begin{aligned}
\vec{A}_0 &= \vec{A}(\vec{R}, t) \\
&= \int \vec{A}(\vec{R}, \omega)e^{i\omega t}d\omega \\
&= \int_{-\infty}^{0} \vec{A}_0(\vec{R}, \omega)e^{i\omega t}d\omega + \int_0^{\infty} \vec{A}_0(\vec{R}, \omega)e^{i\omega t}d\omega \\
&= \int_0^{\infty} \vec{A}_0(\vec{R}, -\omega')e^{-i\omega' t}d\omega' + \int_0^{\infty} \vec{A}_0(\vec{R}, \omega)e^{i\omega t}d\omega \\
&= \int_0^{\infty} [\vec{A}_0(\vec{R}, -\omega)e^{-i\omega t} + \vec{A}_0(\vec{R}, \omega)e^{i\omega t}]d\omega \\
&= \int_0^{\infty} [\vec{A}^{(+)}_{R\omega}e^{-i\omega t} + \vec{A}^{(-)}_{R\omega}e^{i\omega t}]d\omega \\
&= \vec{A}^{(+)}(\vec{R}, t) + \vec{A}^{(-)}(\vec{R}, t).
\end{aligned}$$

Here we have defined the positive and negative frequency components of the vector potential $\vec{A}^{(\pm)}_{R\omega} \equiv \vec{A}(\vec{R}, \mp\omega)$. Since $\vec{A}$ must be a real quantity, necessarily $\vec{A}^{(\pm)*}_{R\omega} = \vec{A}^{(\mp)}_{R\omega}$. From this potential the electric field can be calculated as

$$\begin{aligned}
\vec{E}(\vec{R},t) &= -\partial_t \vec{A}_0 \\
&= \int_0^\infty [i\omega \vec{A}^{(+)}_{R\omega} e^{-i\omega t} - i\omega \vec{A}^{(-)}_{R\omega} e^{i\omega t}] d\omega \\
&\equiv \int_0^\infty [\vec{E}^{(+)}_{R\omega} e^{-i\omega t} + \vec{E}^{(-)}_{R\omega} e^{i\omega t}] d\omega \\
&= \vec{E}^{(+)}(\vec{R},t) + \vec{E}^{(-)}(\vec{R},t),
\end{aligned}$$

which implies that

$$\vec{E}^{(\pm)}_{R\omega} \equiv \pm i\omega \vec{A}^{(\pm)}_{R\omega} \qquad \Rightarrow \qquad \vec{A}^{(\pm)}_{R\omega} = \pm \frac{1}{i\omega} \vec{E}^{(\pm)}_{R\omega}.$$

And therefore $\vec{E}^{(\pm)*}_{R\omega} = \mp i\omega \vec{A}^{(\mp)}_{R\omega} = \vec{E}^{(\mp)}_{R\omega}$. The components of the Hamiltonian can thus be written in terms of the electric field as

$$\begin{aligned}
H_{ij} &= \hbar\omega_i \delta_{ij} + \frac{ie\mu}{m_e} \left[\int_0^\infty [\vec{A}^{(+)}_{R\omega} e^{-i\omega t} + \vec{A}^{(-)}_{R\omega} e^{i\omega t}] d\omega \right] \cdot \langle i|\widehat{\vec{r}}|j\rangle \omega_{ij} \\
&= \hbar\omega_i \delta_{ij} + \frac{e\mu}{m_e} \left[\int_0^\infty \frac{1}{\omega} [\vec{E}^{(+)}_{R\omega} e^{-i\omega t} - \vec{E}^{(-)}_{R\omega} e^{i\omega t}] d\omega \right] \cdot \langle i|\widehat{\vec{r}}|j\rangle \omega_{ij}
\end{aligned} \tag{2.1}$$

In the cases of our interest the resonant frequencies ω_{ij} are of the order of 10^{14} Hz and the detunings of the field frequencies ω with respect to ω_{ij} are at most of 10^8 Hz, in other words $|\omega_{ij}|/\omega \simeq 1$. However, it is important to notice that $\omega_{ij} = -\omega_{ji}$, and therefore

$$\frac{\omega_{ij}}{\omega} \simeq \varepsilon_{ij} = \begin{cases} 1 & \text{if} \quad i > j \\ -1 & \text{if} \quad i < j \\ 0 & \text{if} \quad i = j \end{cases}.$$

If we also take $\mu/m_e \simeq 1$ we get

$$H_{ij} = \hbar\omega_i \delta_{ij} + e \left[\int_0^\infty [\vec{E}^{(+)}_{R\omega} e^{-i\omega t} - \vec{E}^{(-)}_{R\omega} e^{i\omega t}] d\omega \right] \cdot \langle i|\widehat{\vec{r}}|j\rangle \varepsilon_{ij}. \tag{2.2}$$

Since $\vec{E}^{(\pm)*}_{R\omega} = \vec{E}^{(\mp)}_{R\omega}$ it follows that the integral in 2.2 is a purely imaginary vector, and since $\widehat{\vec{r}}$ is hermitian, and ε_{ij} is antisymmetric, it follows that H_{ij} is hermitian as expected. Apart from a relative phase between the positive and negative frequency components, this Hamiltonian is

$$H_{ij} = \hbar\omega_i \delta_{ij} + e \left[\int_0^\infty [\vec{E}^{(+)}_{R\omega} e^{-i\omega t} + \vec{E}^{(-)}_{R\omega} e^{i\omega t}] d\omega \right] \cdot \langle i|\widehat{\vec{r}}|j\rangle = \hbar\omega_i \delta_{ij} + e\vec{E}(\vec{R},t) \cdot \langle i|\widehat{\vec{r}}|j\rangle.$$

We can ignore this relative phase since it is only relevant at time scales comparable to the optical

frequencies, in which it is significantly different if the electric field varies for instance as a sine or as a cosine. We are interested in frequency scales of the order of 10^8 Hz however. This last term is now the usual Hamiltonian found in literature (often without a derivation) as the interaction Hamiltonian between an atom and an electric dipole radiation field.

2.2 Time Evolution Equations

2.2.1 The Rotating Wave Approximation

The electric field can be decomposed in positive and negative frequency terms $\vec{E}^{l(\pm)}$ (see appendix A). The $\widehat{\vec{r}}$ operator can be similarly decomposed. In the interaction picture

$$\widehat{\vec{r}}_I = \exp(i\hat{H}_0 t/\hbar)\widehat{\vec{r}}\exp(-i\hat{H}_0 t/\hbar) = \left(\sum_i e^{i\omega_i t}|i\rangle\langle i|\right)\widehat{\vec{r}}\left(\sum_j e^{-i\omega_j t}|j\rangle\langle j|\right) = \sum_{ij} e^{i\omega_{ij}t}\vec{r}_{ij}|i\rangle\langle j|.$$

If we assume that the ω_i are ordered it follows that $\omega_{ij} \geq 0$ if $i > j$ and vice-versa. It is therefore possible to separate $\widehat{\vec{r}}_I$ in positive and negative frequency components as

$$\widehat{\vec{r}}_I = \sum_{i<j} e^{-i\omega_{ji}}\vec{r}_{ij}|i\rangle\langle j| + \sum_{i>j} e^{i\omega_{ij}}\vec{r}_{ij}|i\rangle\langle j| = \widehat{\vec{r}}_I^{(+)} + \widehat{\vec{r}}_I^{(-)}.$$

The interaction Hamiltonian *in the interaction picture* can be rewritten as

$$-e\vec{E}(\vec{R},t)\cdot\widehat{\vec{r}}_I = -e\sum_l [\vec{E}^{l(+)}(\vec{R},t)\cdot\widehat{\vec{r}}_I^{(+)} + \vec{E}^{l(-)}(\vec{R},t)\cdot\widehat{\vec{r}}_I^{(-)} + \vec{E}^{l(+)}(\vec{R},t)\cdot\widehat{\vec{r}}_I^{(-)} + \vec{E}^{l(-)}(\vec{R},t)\cdot\widehat{\vec{r}}_I^{(+)}],$$

and here it can be seen that the time dependance of the terms $\vec{E}^{l(\pm)}(\vec{R},t)\cdot\widehat{\vec{r}}_I^{(\pm)}$ will have *summed* frequencies $\mp\omega^l \mp \omega_{ij}$, while the time dependance of the terms $\vec{E}^{l(\pm)}(\vec{R},t)\cdot\widehat{\vec{r}}_I^{(\mp)}$ will have *subtracted* frequencies $\mp\omega^l \pm \omega_{ij}$. In our case, the summed frequencies will be of the order of THz, while the subtracted frequencies (the laser detunings) will be of the order of MHz. Since we are interested in examining the course-grained time variation of the states of the atom, we will eliminate the faster summed frequencies. This way the Hamiltonian is reduced to

$$-e\vec{E}(\vec{R},t)\cdot\widehat{\vec{r}}_I = -e[\vec{E}^{(+)}(\vec{R},t)\cdot\widehat{\vec{r}}_I^{(-)} + \vec{E}^{(-)}(\vec{R},t)\cdot\widehat{\vec{r}}_I^{(+)}].$$

This approximation is known as the *rotating wave approximation* (RWA) [**?**]. Going back to the Schrödinger picture, the $\widehat{\vec{r}}$ operator is decomposed as

$$\widehat{\vec{r}} = \sum_{i<j}\vec{r}_{ij}|i\rangle\langle j| + \sum_{i>j}\vec{r}_{ij}|i\rangle\langle j| = \widehat{\vec{r}}^{(+)} + \widehat{\vec{r}}^{(-)}.$$

The complete Hamiltonian becomes

$$\hat{H} = \hat{H}_0 - e[\vec{E}^{(+)}(\vec{R},t)\cdot\hat{\vec{r}}^{(-)} + \vec{E}^{(-)}(\vec{R},t)\cdot\hat{\vec{r}}^{(+)}].$$

The matrix elements of this Hamiltonian are

$$\begin{aligned} H_{ij} &= \hbar\omega_i\delta_{ij} - e(\vec{E}^{(-)}\cdot\vec{r}_{ij}^{(+)} + \vec{E}^{(+)}\cdot\vec{r}_{ij}^{(-)}) \\ &= \hbar\omega_i\delta_{ij} - e\textstyle\sum_l (e^{i\omega^l t}\vec{E}_0^{l(-)}\cdot\vec{r}_{ij}^{(+)} + e^{-i\omega^l t}\vec{E}_0^{l(+)}\cdot\vec{r}_{ij}^{(-)}) \\ &= \hbar\omega_i\delta_{ij} - e\textstyle\sum_l \left(\underset{i<j}{\delta} e^{i\omega^l t}\vec{E}_0^{l(-)}\cdot\vec{r}_{ij} + \underset{i>j}{\delta} e^{-i\omega^l t}\vec{E}_0^{l(+)}\cdot\vec{r}_{ij}\right) \\ &= \hbar\omega_i\delta_{ij} - e\textstyle\sum_l E_0^l \left(\underset{i<j}{\delta} e^{i\omega^l t}\vec{\varepsilon}^{l(-)}\cdot\vec{r}_{ij} + \underset{i>j}{\delta} e^{-i\omega^l t}\vec{\varepsilon}^{l(+)}\cdot\vec{r}_{ij}\right) \end{aligned} \tag{2.3}$$

where $\underset{i>j}{\delta}$ is a symbol similar to Kronecker's delta that is 1 if $i > j$ and 0 otherwise. The polarization vectors $\vec{\varepsilon}^{l(\pm)}$ are defined in appendix A.

The dot products in this expression can be calculated directly from A.1 using the Cartesian base with the usual form of the dot product. However, as mentioned before, we will prefer the helicity basis for the calculation of the matrix elements of $\vec{r}_{ij}$. The dot product in this base is

$$\vec{\varepsilon}^{l(\pm)}\cdot\vec{r}_{ij} = \sum_{p=-1}^{1}(-1)^p T^1_{-p}(\vec{\varepsilon}^{l(\pm)})T^1_p(\vec{r}_{ij}) \equiv \sum_{p=-1}^{1}(-1)^p Y^{l(\pm)}_{-p} r_{pij}, \tag{2.4}$$

where $r_{pij} \equiv T^1_p(\vec{r}_{ij})$ is the p component of $\vec{r}_{ij}$ in the helicity basis, and $Y^{l(\pm)}_p$ are the coefficients of $\vec{\varepsilon}^{l(\pm)}$ in the helicity basis, also defined in appendix A.

2.2.2 The Rotating Frame

If the Hamiltonian 2.3 is used to calculate the time evolution equations of the density matrix $\hat{\rho}$ they will have an explicit time dependance. The derivatives $\dot{\rho}_{ij}$ will have a time dependance $e^{i\omega^l t}$ multiplying each term with ρ_{ij}. In other words, there is no value of t for which all the $\dot{\rho}_{ij}$ become zero, and therefore the density matrix never reaches a steady state. To calculate the dynamics it would be extremely useful to make a variable change that eliminates the explicit time dependance of the equations, so the equations reduce to a system of first-order differential equations with constant coefficients. The general theory for this kind of equations is much simpler than that for variable coefficients (which is what we have so far).

This can be achieved by making a *phase transformation* $|\psi\rangle = \sum_i c_i(t)|i\rangle = \sum_i e^{i\theta_i t}\tilde{c}_i(t)|i\rangle$.

Introducing this into Schrödinger's equation for our Hamiltonian we get

$$\begin{aligned} i\hbar\partial_t|\psi\rangle &= \hat{H}|\psi\rangle \\ i\hbar\sum_i(e^{i\theta_i t}\dot{\tilde{c}}_i + i\theta_i e^{i\theta_i t}\tilde{c}_i)|i\rangle &= \sum_{ia} H_{ia}|i\rangle\langle a|\left(\sum_j e^{i\theta_j t}\tilde{c}_j|j\rangle\right) \\ \hbar\sum_i(ie^{i\theta_i t}\dot{\tilde{c}}_i - \theta_i e^{i\theta_i t}\tilde{c}_i)|i\rangle &= \sum_{iaj} H_{ia}e^{i\theta_j t}\tilde{c}_j|i\rangle\langle a||j\rangle \\ &= \sum_{ij} H_{ij}e^{i\theta_j t}\tilde{c}_j|i\rangle \end{aligned}$$

multiplying by $e^{-i\theta_i t}\langle i|$ and adding $\hbar\theta_i\tilde{c}_i$ we get

$$i\hbar\dot{\tilde{c}}_i = \hbar\theta_i\tilde{c}_i + \sum_j H_{ij}e^{i(\theta_j-\theta_i)t}\tilde{c}_j,$$

and substituting the Hamiltonian 2.3 these equations become

$$\begin{aligned} i\hbar\dot{\tilde{c}}_i = &\sum_j\left[\hbar\omega_i\delta_{ij} - e\sum_l E_0^l\left(\underset{i<j}{\delta}e^{i\omega^l t}\vec{\varepsilon}^{\,l(-)}\cdot\vec{r}_{ij} + \underset{i>j}{\delta}e^{-i\omega^l t}\vec{\varepsilon}^{\,l(+)}\cdot\vec{r}_{ij}\right)\right]e^{i(\theta_j-\theta_i)t}\tilde{c}_j. \\ &+\hbar\theta_i\tilde{c}_i \\ &= -e\sum_j\sum_l E_0^l\left(\underset{i<j}{\delta}e^{i(\omega^l+\theta_j-\theta_i)t}\vec{\varepsilon}^{\,l(-)}\cdot\vec{r}_{ij} + \underset{i>j}{\delta}e^{-i(\omega^l+\theta_i-\theta_j)t}\vec{\varepsilon}^{\,l(+)}\cdot\vec{r}_{ij}\right)\tilde{c}_j. \\ &+\hbar(\omega_i+\theta_i)\tilde{c}_i. \end{aligned}$$

Here we can see that the conditions to eliminate the explicit time dependance are

$$\omega^l + \theta_j - \theta_i = 0 \qquad \forall\ \ i<j\ \ \&\ \ \forall\ \ l.$$

Notice that equations $\omega^l+\theta_i-\vartheta_j=0$ with $i>j$ are equivalent. These are $N_l N_e(N_e-1)/2$ equations, which in general are impossible to solve for the N_e phase changes θ_i.

There is hope though. The selection rules couple only some pairs of states, making the $\widehat{\vec{r}}$ operator very sparse (in the matrix sense). If a component $\vec{r}_{ij}$ equals zero the N_l terms $e^{i(\omega^l+\theta_j-\theta_i)t}\vec{\varepsilon}^{\,l(\pm)}\cdot\vec{r}_{ij}$ in Schrödingers' equations are zero, and the equations $\omega^l+\theta_j-\theta_i=0$ are not necessary. This way the number of equations is reduced to $D(\widehat{\vec{r}})N_l N_e(N_e-1)/2$ where $D(\widehat{\vec{r}})$ is the density of the $\widehat{\vec{r}}$ operator (in the matrix sense).

We can also make the approximation (very realistic in the cases of interest) of assuming that each transition is driven only by one of the N_l radiation fields, or at least not by all of them. In each component of the Hamiltonian there are N_l terms corresponding to the excitation produced by each field on the i,j transition. We can define L_{ij} as the set of fields that are considered to excite

the i, j transition. Therefore the Hamiltonian becomes

$$H_{ij} = \hbar\omega_i\delta_{ij} - e\sum_{l\in L_{ij}} E_0^l \left(\underset{i<j}{\delta} e^{i\omega^l t}\vec{\varepsilon}^{\,l(-)}\cdot\vec{r}_{ij} + \underset{i>j}{\delta} e^{-i\omega^l t}\vec{\varepsilon}^{\,l(+)}\cdot\vec{r}_{ij} \right)$$

and the necessary conditions are reduced to

$$\omega^l + \theta_j - \theta_i = 0 \qquad \forall i \;\mid\; i<j,\;\; \vec{r}_{ij}\neq 0 \;\;\&\;\; \forall \;\; l\in L_{ij}.$$

If this system of equations has at least one solution, then replacing any of them in Schrödinger's equation leads to

$$\begin{aligned} i\hbar\dot{\tilde{c}}_i &= \hbar(\omega_i+\theta_i)\tilde{c}_i - e\sum_j\sum_{l\in L_{ij}} E_0^l \left(\underset{i<j}{\delta}\vec{\varepsilon}^{\,l(-)}\cdot\vec{r}_{ij} + \underset{i>j}{\delta}\vec{\varepsilon}^{\,l(+)}\cdot\vec{r}_{ij} \right)\tilde{c}_j \\ &= \sum_j \left[\hbar(\omega_i+\theta_i)\delta_{ij} - e\sum_{l\in L_{ij}} E_0^l \left(\underset{i<j}{\delta}\vec{\varepsilon}^{\,l(-)}\cdot\vec{r}_{ij} + \underset{i>j}{\delta}\vec{\varepsilon}^{\,l(+)}\cdot\vec{r}_{ij} \right) \right]\tilde{c}_j. \end{aligned}$$

This equations have no explicit time dependance. For a two level system, if the state $|\psi\rangle$ is represented by a Bloch vector, this transformation is equivalent to changing the Bloch vector to a frame that rotates with frequency $\omega^1 - \omega_{21}$, this is why this technique is known as going to the *rotating frame*. This is the Schrödinger equation corresponding to an *effective Hamiltonian* whose matrix elements are

$$\tilde{H}_{ij} = \hbar(\omega_i+\theta_i)\delta_{ij} - e\sum_{l\in L_{ij}} E_0^l \left(\underset{i<j}{\delta}\vec{\varepsilon}^{\,l(-)}\cdot\vec{r}_{ij} + \underset{i>j}{\delta}\vec{\varepsilon}^{\,l(+)}\cdot\vec{r}_{ij} \right). \tag{2.5}$$

The tilde~has been added here to denote an effective operator in the rotating frame. This should not be confused with similar notation in other sources where the tilde denotes operators in the interaction picture (both uses are common).

We can now use this Hamiltonian to derive the explicit form of the time evolution equations of

the density matrix for the components of an *effective density matrix* $\tilde{\rho}_{ij} = e^{-i(\theta_i - \theta_j)t}\rho_{ij}$.

$$
\begin{aligned}
\dot{\tilde{\rho}}_{ij} &= \frac{i}{\hbar}\sum_k [\tilde{\rho}_{ik}\tilde{H}_{kj} - \tilde{H}_{ik}\tilde{\rho}_{kj}] \\
&= -\frac{ie}{\hbar}\sum_k \left[\tilde{\rho}_{ik} \sum_{l\in L_{kj}} E_0^l \left(\underset{k<j}{\delta}\vec{\varepsilon}^{\,l(-)}\cdot\vec{r}_{kj} + \underset{k>j}{\delta}\vec{\varepsilon}^{\,l(+)}\cdot\vec{r}_{kj} \right) \right. \\
&\qquad \left. - \sum_{l\in L_{ik}} E_0^l \left(\underset{i<k}{\delta}\vec{\varepsilon}^{\,l(-)}\cdot\vec{r}_{ik} + \underset{i>k}{\delta}\vec{\varepsilon}^{\,l(+)}\cdot\vec{r}_{ik} \right) \tilde{\rho}_{kj} \right] \\
&+ \frac{i}{\hbar}\sum_k [\tilde{\rho}_{ik}\hbar(\omega_k + \theta_k)\delta_{kj} - \hbar(\omega_i + \theta_i)\delta_{ik}\tilde{\rho}_{kj}] \\
&= \frac{ie}{\hbar}\sum_k \left[\sum_{l\in L_{ik}} E_0^l \left(\underset{i<k}{\delta}\vec{\varepsilon}^{\,l(-)}\cdot\vec{r}_{ik} + \underset{i>k}{\delta}\vec{\varepsilon}^{\,l(+)}\cdot\vec{r}_{ik} \right) \tilde{\rho}_{kj} \right. \\
&\qquad \left. - \sum_{l\in L_{kj}} E_0^l \left(\underset{k<j}{\delta}\vec{\varepsilon}^{\,l(-)}\cdot\vec{r}_{kj} + \underset{k>j}{\delta}\vec{\varepsilon}^{\,l(+)}\cdot\vec{r}_{kj} \right) \tilde{\rho}_{ik} \right] \\
&+ i[\theta_j - \theta_i - \omega_{ij}]\tilde{\rho}_{ij}
\end{aligned}
$$

2.2.3 Spontaneous Decay

Because of the interaction of the atom with the vacuum of the surrounding elecromagnetic field, each state $|i\rangle$ has a decay frequency γ_{ij} towards the $|j\rangle$ state. Since each $|i\rangle \to |j\rangle$ decay implies loss of population in $|i\rangle$ and gain in $|j\rangle$, it follows that $\gamma_{ij} = -\gamma_{ji}$. Each of these decays is described in the equations by a Lindblad operator

$$\dot{\hat{\rho}} = \frac{i}{\hbar}[\hat{\rho}, \hat{H}] + \sum_{a>b}\gamma_{ab}\mathcal{L}(\hat{\sigma}_{ab})\hat{\rho}$$

where

$$
\begin{aligned}
\gamma_{ab}\mathcal{L}(\hat{\sigma}_{ab})\hat{\rho} &= \gamma_{ab}\mathcal{L}\left(|b\rangle\langle a|\right)\hat{\rho} \\
&= \gamma_{ab}\left[|b\rangle\langle a|\hat{\rho}|a\rangle\langle b| - \frac{1}{2}\left[|a\rangle\langle b|b\rangle\langle a|\hat{\rho} + \hat{\rho}|a\rangle\langle b|b\rangle\langle a|\right]\right] \\
&= \gamma_{ab}\left[|b\rangle\langle a|\sum_{cd}\rho_{cd}|c\rangle\langle d||a\rangle\langle b| - \frac{1}{2}\left[|a\rangle\langle b|b\rangle\langle a|\sum_{cd}\rho_{cd}|c\rangle\langle d| + \sum_{cd}\rho_{cd}|c\rangle\langle d||a\rangle\langle b|b\rangle\langle a|\right]\right] \\
&= \sum_{cd}\gamma_{ab}\left[\rho_{cd}|b\rangle\langle a||c\rangle\langle d||a\rangle\langle b| - \frac{1}{2}\left[\rho_{cd}|a\rangle\langle b|b\rangle\langle a||c\rangle\langle d| + \rho_{cd}|c\rangle\langle d||a\rangle\langle b|b\rangle\langle a|\right]\right] \\
&= \sum_{cd}\gamma_{ab}\left[\rho_{cd}\delta_{ac}\delta_{da}|b\rangle\langle b| - \frac{1}{2}\left[\rho_{cd}\delta_{ac}|a\rangle\langle d| + \rho_{cd}\delta_{da}|c\rangle\langle a|\right]\right] \\
&= \gamma_{ab}\left[\rho_{aa}|b\rangle\langle b| - \frac{1}{2}\left[\sum_{d}\rho_{ad}|a\rangle\langle d| + \sum_{c}\rho_{ca}|c\rangle\langle a|\right]\right] \\
&= \gamma_{ab}\left[\rho_{aa}\left(|b\rangle\langle b| - |a\rangle\langle a|\right) - \frac{1}{2}\left[\sum_{d\neq a}\rho_{ad}|a\rangle\langle d| + \sum_{c\neq a}\rho_{ca}|c\rangle\langle a|\right]\right].
\end{aligned}
$$

The matrix elements of the equations corresponding to each decay are

$$
\begin{aligned}
\langle i|\gamma_{ab}\mathcal{L}(\hat{\sigma}_{ab})\hat{\rho}|j\rangle &= \gamma_{ab}\left[\rho_{aa}\left(\langle i|b\rangle\langle b|j\rangle - \langle i|a\rangle\langle a|j\rangle\right) - \frac{1}{2}\left[\sum_{d\neq a}\rho_{ad}\langle i|a\rangle\langle d|j\rangle + \sum_{c\neq a}\rho_{ca}\langle i|c\rangle\langle a|j\rangle\right]\right] \\
&= \gamma_{ab}\left[\rho_{aa}(\delta_{ib}\delta_{bj} - \delta_{ia}\delta_{aj}) - \frac{1}{2}\left[\sum_{d\neq a}\rho_{ad}\delta_{ia}\delta_{dj} + \sum_{c\neq a}\rho_{ca}\delta_{ic}\delta_{aj}\right]\right],
\end{aligned}
$$

so the equations become

$$
\begin{aligned}
\dot{\tilde{\rho}}_{ij} \quad &= \tfrac{ie}{\hbar}\Big[\textstyle\sum_k\sum_{l\in L_{ik}} E_0^l\left(\delta_{k>j}\left(\delta_{k>i}\vec{\varepsilon}^{\,l(-)}\cdot\vec{r}_{ik} + \delta_{k<i}\vec{\varepsilon}^{\,l(+)}\cdot\vec{r}_{ik}\right)\tilde{\rho}_{kj} + \delta_{k<j}(\vec{\varepsilon}^{\,l(+)}\cdot\vec{r}_{ik})\tilde{\rho}^*_{jk}\right) \\
&\quad - \textstyle\sum_k\sum_{l\in L_{kj}} E_0^l\left(\delta_{k<i}\left(\delta_{k<j}\vec{\varepsilon}^{\,l(-)}\cdot\vec{r}_{kj} + \delta_{k>j}\vec{\varepsilon}^{\,l(+)}\cdot\vec{r}_{kj}\right)\tilde{\rho}_{ik} + \delta_{k>i}(\vec{\varepsilon}^{\,l(+)}\cdot\vec{r}_{kj})\tilde{\rho}^*_{ki}\right) \\
&\quad + \textstyle\sum_{l\in L_{ij}} E_0^l(\vec{\varepsilon}^{\,l(+)}\cdot\vec{r}_{ij}\rho_{jj} - \vec{\varepsilon}^{\,l(+)}\cdot\vec{r}_{ij}\rho_{ii})\Big] \\
&\quad + i\Theta_{ij}\tilde{\rho}_{ij} \\
&\quad + \textstyle\sum_{a>b}\gamma_{ab}\left[\rho_{aa}(\delta_{ib}\delta_{bj} - \delta_{ia}\delta_{aj}) - \frac{1}{2}\left[\sum_{d\neq a}\rho_{ad}\delta_{ia}\delta_{dj} + \sum_{c\neq a}\rho_{ca}\delta_{ic}\delta_{aj}\right]\right]
\end{aligned}
\tag{2.6}
$$

with $i > j$. Here we have defined $\Theta_{ij} \equiv \theta_j - \theta_i - \omega_{ij}$. This is the only part of the equations in which optical frequencies appear. Whenever possible this will be expressed in terms of detunings $\delta^l_{ij} \equiv \omega^l - \omega_{ij}$. The *detuning knobs* δ^l are defined as the δ^l_{ij} for the smallest ω_{ij} such that field l couples the $|i\rangle \to |j\rangle$ transition.

2.2.4 Reduction of the number of variables

We can make a few important simplifications to make the calculations more efficient. Firstly, since $\tilde{\rho}_{ij} = \tilde{\rho}^*_{ji}$ then $\dot{\tilde{\rho}}_{ij} = \dot{\tilde{\rho}}^*_{ji}$, so we can use only the equations $\dot{\tilde{\rho}}_{ij}$ with $i \geq j$ expressing them purely in terms of the $\tilde{\rho}_{ij}$ with $i \geq j$

$$\begin{aligned}
\dot{\tilde{\rho}}_{ij} \quad &= \tfrac{ie}{\hbar}\Bigg[\textstyle\sum_k \sum_{l\in L_{ik}} E_0^l \left(\delta_{k>j}\left(\delta_{k>i}\vec{\varepsilon}^{\,l(-)}\cdot\vec{r}_{ik} + \delta_{k<i}\vec{\varepsilon}^{\,l(+)}\cdot\vec{r}_{ik}\right)\tilde{\rho}_{kj} + \delta_{k<j}(\vec{\varepsilon}^{\,l(+)}\cdot\vec{r}_{ik})\tilde{\rho}^*_{jk}\right) \\
&\quad - \textstyle\sum_k \sum_{l\in L_{kj}} E_0^l \left(\delta_{k<i}\left(\delta_{k<j}\vec{\varepsilon}^{\,l(-)}\cdot\vec{r}_{kj} + \delta_{k>j}\vec{\varepsilon}^{\,l(+)}\cdot\vec{r}_{kj}\right)\tilde{\rho}_{ik} + \delta_{k>i}(\vec{\varepsilon}^{\,l(+)}\cdot\vec{r}_{kj})\tilde{\rho}^*_{ki}\right) \\
&\quad + \textstyle\sum_{l\in L_{ij}} E_0^l(\vec{\varepsilon}^{\,l(+)}\cdot\vec{r}_{ij}\rho_{jj} - \vec{\varepsilon}^{\,l(+)}\cdot\vec{r}_{ij}\rho_{ii})\Bigg] \\
&+ i\Theta_{ij}\tilde{\rho}_{ij} \\
&+ \textstyle\sum_{a>b}\gamma_{ab}\left[\rho_{aa}(\delta_{ib}\delta_{bj} - \delta_{ia}\delta_{aj}) - \frac{1}{2}\left[\sum_{d\neq a}\rho_{ad}\delta_{ia}\delta_{dj} + \sum_{c\neq a}\rho_{ca}\delta_{ic}\delta_{aj}\right]\right].
\end{aligned} \tag{2.7}$$

Secondly, the trace of the density matrix is normalized to 1, therefore we can avoid calculating one of the equations along the diagonal of $\dot{\tilde{\rho}}_{ij}$. We choose $\rho_{11} = 1 - \sum_{k=2}^{N_e}\rho_{kk}$. To implement this formula in programming it is convenient to use an exception for the terms that depend on $\tilde{\rho}_{11}$. These terms are in equations $\dot{\tilde{\rho}}_{i1}$ with $i \neq 1$, shown in blue in 2.7.

Since the populations are always real, we are thus left with

$$N_\rho \equiv N_e^2 - 1$$

real numbers to characterize the density matrix, instead of all $2N_e^2$ real and imaginary parts of the matrix elements.

2.3 The Steady State

Solving these optical Bloch equations one obtains the time evolution of the density matrix. However, in the present work the detailed time evolution of the density matrix is not necessary. Instead, the atoms are given enough time to reach a state in which $\dot{\tilde{\rho}}_{ij} = 0$, known as the *steady state*. Under typical experimental conditions the steady state is reached in times comparable to the inverse $(2\pi \cdot 667\,\mathrm{KHz})^{-1} \approx 238\,\mathrm{ns}$. Therefore, under variations of experimental conditions that occur in time scales longer than this, the density matrix can be considered to always be in a steady state.

Furthermore, although the equations in the form obtained so far may be used to calculate time evolution by integrating numerically (for instance with Runge-Kutta methods) this is far from the best approach. Instead, both the time evolution and the steady state can be calculated with methods far more reliable and efficient that exploit the linearity of the equations to attack the problem with advanced software for linear algebra.

Given arbitrary initial conditions the density matrix will evolve according to equations 2.7 until

it reaches the steady state. Since all the terms in these equations depend at most linearly in some $\tilde{\rho}_{ab}$, this defines a system of linear equations. If one were not to replace $\tilde{\rho}_{11} = 1 - \sum_{i=2}^{N_l} \tilde{\rho}_{ii}$ all of the terms would be linear in some $\tilde{\rho}_{ab}$, but the 1 in this substitution gives rise to terms that have no dependance on density matrix components. If we now think of the density matrix as a vector in a vector space whose dimension is the number of independent real components of the density matrix ($N_\rho \equiv N_e^2 - 1$) the equations can be seen to be of the form

$$\dot{\vec{\tilde{\rho}}} = \hat{A}\vec{\tilde{\rho}} - \vec{b}, \tag{2.8}$$

where $\hat{A}$ is a matrix whose components are the coefficients of the linear combinations of $\tilde{\rho}_{ab}$ in the equations and $\vec{b}$ is a vector whose components are the independent terms in each equation (if any). The equations in the steady state are therefore

$$\hat{A}\vec{\tilde{\rho}} = \vec{b}.$$

Thus the steady state can be found by solving this system of linear algebraic equations. However, the challenge now is to produce the $\hat{A}$ matrix and the $\vec{b}$ vector from the experimental parameters $E_0^l, \delta^l, \omega_{ij}, \gamma_{ij}$ and r_{pij}.

To write the system of equations in matrix form some order for the components must be established. We will define an index $\mu(i,j)$ in the following way

$$\mu = \underbrace{1, 2, \ldots N_e - 1}_{\text{Populations}}, \underbrace{N_e, \ldots \frac{N_e^2 + N_e}{2} - 1}_{\text{Real parts of coherences}}, \underbrace{\frac{N_e^2 + N_e}{2}, \ldots N_e^2 - 1}_{\text{Imaginary parts of coherences}}$$

to label the components of the density matrix in the following way

1. The first $N_e - 1$ indices correspond to the populations $\rho_{22}, \ldots \rho_{N_e N_e}$.
2. The next $\frac{N_e(N_e-1)}{2}$ indices correspond to the real parts of the coherences $\tilde{\rho}_{ij}$ with $i > j$ ordered by columns left to right and in descending order.
3. The next $\frac{N_e(N_e-1)}{2}$ indices correspond to the imaginary parts of coherences $\tilde{\rho}_{ij}$ with $i > j$ ordered in the same way.

This way, μ can be calculated as

$$\mu(i,j,s) = \begin{cases} i - 1 & \text{if} i = j \\ i - j + \sum_{k=1}^{j-1}(N_e - k) & \text{if} i \neq j \quad \& \quad s = +1 \\ N_e(N_e-1)/2 + i - j + \sum_{k=1}^{j-1}(N_e - k) & \text{if} i \neq j \quad \& \quad s = -1 \end{cases}$$

Once established this correspondence the functions $i(\mu)$ and $j(\mu)$ are also defined. Also, to simplify

the notation, we will define a *part* operator that extracts the real or imaginary part of a complex number

$$\mathfrak{Pa}(s,z) = \begin{cases} \Re\mathfrak{e}(z) & \text{if} s = +1 \\ \Im\mathfrak{m}(z) & \text{if} s = -1 \end{cases}.$$

A detailed derivation of the independent vector is given in appendix C that results in

$$b^{\nu(i,1,s)} = -s\frac{e}{\hbar}\sum_{l\in L_{i1}} E_0^l \mathfrak{Pa}(-s, \vec{\varepsilon}^{\,l(+)}\cdot\vec{r}_{i1}) \tag{2.9}$$

The components of the $\hat{A}$ operator can be obtained from

$$\begin{aligned}
\dot{\tilde{\rho}}_{\mu(i,j,s)} \quad = \tfrac{se}{\hbar}\Big[\textstyle\sum_k \sum_{l\in L_{kj}} E_0^l \Big(&\delta_{k<ik<j}(\mathfrak{Pa}(-s,\vec{\varepsilon}^{\,l(-)}\cdot\vec{r}_{kj})\tilde{\rho}_{\nu(i,k,1)} + s\mathfrak{Pa}(s,\vec{\varepsilon}^{\,l(-)}\cdot\vec{r}_{kj})\tilde{\rho}_{\nu(i,k,-1)}) \\
&+\delta_{k<ik>j}(\mathfrak{Pa}(-s,\vec{\varepsilon}^{\,l(+)}\cdot\vec{r}_{kj})\tilde{\rho}_{\nu(i,k,1)} + s\mathfrak{Pa}(s,\vec{\varepsilon}^{\,l(+)}\cdot\vec{r}_{kj})\tilde{\rho}_{\nu(i,k,-1)}) \\
&+\delta_{k>i}\quad(\mathfrak{Pa}(-s,\vec{\varepsilon}^{\,l(+)}\cdot\vec{r}_{kj})\tilde{\rho}_{\nu(k,i,1)} - s\mathfrak{Pa}(s,\vec{\varepsilon}^{\,l(+)}\cdot\vec{r}_{kj})\tilde{\rho}_{\nu(k,i,-1)})\Big) \\
-\textstyle\sum_{l\in L_{ik}} E_0^l \Big(&\delta_{k>jk>i}(\mathfrak{Pa}(-s,\vec{\varepsilon}^{\,l(-)}\cdot\vec{r}_{ik})\tilde{\rho}_{\nu(k,j,1)} + s\mathfrak{Pa}(s,\vec{\varepsilon}^{\,l(-)}\cdot\vec{r}_{ik})\tilde{\rho}_{\nu(k,j,-1)}) \\
&+\delta_{k>jk<i}(\mathfrak{Pa}(-s,\vec{\varepsilon}^{\,l(+)}\cdot\vec{r}_{ik})\tilde{\rho}_{\nu(k,j,1)} + s\mathfrak{Pa}(s,\vec{\varepsilon}^{\,l(+)}\cdot\vec{r}_{ik})\tilde{\rho}_{\nu(k,j,-1)}) \\
&+\delta_{k<j}\quad(\mathfrak{Pa}(-s,\vec{\varepsilon}^{\,l(+)}\cdot\vec{r}_{ik})\tilde{\rho}_{\nu(j,k,1)} - s\mathfrak{Pa}(s,\vec{\varepsilon}^{\,l(+)}\cdot\vec{r}_{ik})\tilde{\rho}_{\nu(j,k,-1)})\Big) \\
+\textstyle\sum_{l\in L_{ij}} E_0^l \mathfrak{Pa}(-s,\vec{\varepsilon}^{\,l(+)}\cdot\vec{r}_{ij})&(\rho_{\nu(i,i)} - \rho_{\nu(j,j)})\Big] \\
-s\Theta_{ij}\tilde{\rho}_{\nu(i,j,-s)} - \tfrac{\gamma_{ij}}{2}&\tilde{\rho}_{\nu(i,j,s)} \\
+\textstyle\sum_{a>b}\gamma_{ab}\Big[(\delta_{ib}\delta_{bj} - \delta_{ia}\delta_{aj})\rho_{\nu(a,a,s)} - \tfrac{1}{2}\Big[\sum_{d\neq a}\delta_{ia}\delta_{dj}\tilde{\rho}_{\nu(a,d,s)} + \sum_{c\neq a}\delta_{ic}\delta_{aj}\tilde{\rho}_{(c,a,s)}\Big]\Big]&.
\end{aligned} \tag{2.10}$$

which is also derived in detail in appendix C.

2.4 The Two Level System

The simplest version of these equations is that for a two level system coupled by a single radiation field. In other words $N_e = 2, N_l = 1$. Assuming that the light is taken to be linearly polarized along the $\hat{z}$ axis, the effective Hamiltonian as given by 2.5 is

$$\widehat{\widetilde{H}} = \begin{pmatrix} \hbar(\omega_1 + \omega^1) & \frac{1}{2}eE_0^1 r_{012} \\ \frac{1}{2}eE_0^1 r_{021} & \hbar\omega_2 \end{pmatrix}.$$

We can change the zero of our energy without changing any of the physics by subtracting $\hbar(\omega_1+\omega^1)I_2$ from this Hamiltonian (with I_2 the 2×2 identity matrix). We define a generalized Rabi frequency as

$$\Omega_{lij} = \frac{e}{\hbar}\vec{E}_0^l\cdot\vec{r}_{ij},$$

so we can take $\Omega_1 = eE_0^1 r_{021}/\hbar$ and rewrite the Hamiltonian more conveniently as

$$\widehat{\tilde{H}} = \hbar \begin{pmatrix} 0 & \frac{1}{2}\Omega_1 \\ \frac{1}{2}\Omega_1 & -\delta^1 \end{pmatrix}$$

Laser fields will be labelled with superindices and subindices somewhat interchangeably in this section and the next. If we now consider a decay frequency $\gamma = \gamma_{21}$ from the higher state, the time evolution equations in their matrix form as described in section 2.3

$$\dot{\vec{\rho}} = \begin{pmatrix} -\gamma & 0 & -\Omega_1 \\ 0 & -\frac{\gamma}{2} & -\delta^1 \\ \Omega_1 & \delta^1 & \frac{\gamma}{2} \end{pmatrix} \vec{\rho} - \begin{pmatrix} 0 \\ 0 \\ \frac{\Omega_1}{2} \end{pmatrix}.$$

which are found in many textbooks [44], [21] written in slightly different terms, often called *the* optical Bloch equations. The steady state for this equations is

$$\vec{\rho} = \begin{pmatrix} \rho_{22} \\ \Re\mathfrak{e}\rho_{21} \\ \Im\mathfrak{m}\rho_{21} \end{pmatrix} = \begin{pmatrix} \frac{2\Omega_1\delta_1}{(2\Omega_1^2+\gamma^2+4\delta_1^2)} \\ \frac{\Omega_1^2}{(2\Omega_1^2+\gamma^2+4\delta_1^2)} \\ \frac{-\Omega_1\gamma}{(2\Omega_1^2+\gamma^2+4\delta_1^2)} \end{pmatrix}.$$

which will be of use in chapter 4. Figure 2-1a) shows the dependance of ρ_{22} on the Rabi frequency Ω_1. As the power increases, the population in the excited state grows, and in resonance it asymptotically approaches 1/2. The full width at half maximum (FWHM) is shown as horizontal bars. It can be easily shown that FWHM $= \sqrt{2\Omega_1^2 + \gamma^2}$. It can be seen that this grows with power, which is known as *power broadening.*

Figure 2-1b) shows the real part of $\tilde{\rho}_{21}$ with dashed lines and the imaginary part as solid lines of the same colour. The imaginary part is proportional to the absorption coefficient of the atomic medium, and the real part is the electric susceptibility [47].

2.5 The Three Level Ladder System

Another less trivial example that will be of use in this thesis as a simple approximation to the experimental spectroscopy described in chapter 5 is the three level ladder system. This system is dicussed in detail in [76]. Consider this same two level system, with one more state with energy higher than the other two. This third state is coupled by a second laser field to the *higher energy* lower state. This particular choice of coupling leaves levels 1-3 decoupled ($\vec{r}_{13} = \vec{r}_{31} = 0$), which defines the *ladder* system, as opposed to the *lambda* and *V* systems that leave levels 1-2 and 2-3 decoupled respectively. This three configurations are sometimes called Ξ, Λ, V respectively, since

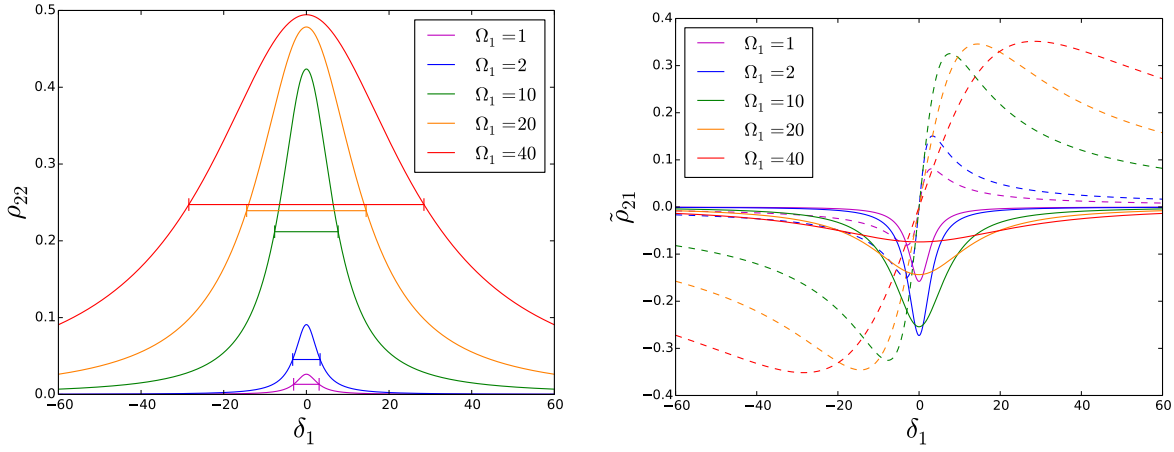

(a) (b)

Figure 2-1: The overall tendency of the density matrix for $\gamma = 6$. a) The excited state population ρ_{22} b) The real part of the coherence ρ_{21} in dashed lines and the imaginary part of the coherence ρ_{21} in dashed lines.

those characters somehow depict the couplings [23].

These are the most simple systems for which eliminating the explicit time dependance from the equations is not trivial. For the Ladder system it is necessary to approximate field 1 as coupling *only* levels 1-2, and field 2 as coupling *only* levels 2-3. In other words, it is necessary to consider

$$L_{ij} = \begin{pmatrix} \{\} & \{1\} & \{\} \\ \{1\} & \{\} & \{2\} \\ \{\} & \{2\} & \{\} \end{pmatrix}$$

in expression 2.5 for the effective Hamiltonian. With this consideration, and taking both fields to be linearly polarized along the $\hat{z}$ axis the effective Hamiltonian is

$$\hat{\tilde{H}} = \begin{pmatrix} \hbar(\omega_1 + \omega^1 + \omega^2) & \frac{1}{2}eE_0^1 r_{012} & 0 \\ \frac{1}{2}eE_0^1 r_{021} & \hbar(\omega_2 + \omega^2) & \frac{1}{2}eE_0^2 r_{023} \\ 0 & \frac{1}{2}eE_0^2 r_{032} & \hbar\omega_3 \end{pmatrix}.$$

Substracting $\hbar(\omega_1 + \omega^1 + \omega^2)I_3$ (with I_3 the 3×3 identity matrix) and defining $\Omega_1 = eE_0^1 r_{021}/\hbar$ and $\Omega_2 = eE_0^2 r_{032}/\hbar$ the Hamiltonian becomes

$$\hat{\tilde{H}} = \hbar \begin{pmatrix} 0 & \frac{1}{2}\Omega_1 & 0 \\ \frac{1}{2}\Omega_1 & -\delta^1 & \frac{1}{2}\Omega_2 \\ 0 & \frac{1}{2}\Omega_2 & -\delta^1 - \delta^2 \end{pmatrix}. \tag{2.11}$$

where $\delta^1 = \omega^1 - \omega_2 + \omega_1$ and $\delta^2 = \omega^2 - \omega_3 + \omega_2$. Considering decay frequencies γ_{21} and γ_{32} we get

the following optical Bloch equations in matrix form

$$\dot{\vec{\rho}} = \begin{pmatrix} -\gamma_{21} & \gamma_{32} & 0 & 0 & 0 & -\Omega^1 & 0 & \Omega_2 \\ 0 & -\gamma_{32} & 0 & 0 & 0 & 0 & 0 & -\Omega_2 \\ 0 & 0 & -\frac{\gamma_{21}}{2} & 0 & 0 & -\delta^1 & \frac{\Omega_2}{2} & 0 \\ 0 & 0 & 0 & -\gamma_{32} & 0 & \frac{\Omega_2}{2} & -\delta^1-\delta^2 & -\frac{\Omega_1}{2} \\ 0 & 0 & 0 & 0 & -\frac{\gamma_{21}+\gamma_{32}}{2} & 0 & -\frac{\Omega_1}{2} & -\delta^2 \\ \Omega_1 & \frac{\Omega_1}{2} & \delta^1 & -\frac{\Omega_2}{2} & 0 & -\gamma_{21} & 0 & 0 \\ 0 & 0 & -\frac{\Omega_2}{2} & \delta^1+\delta^2 & \frac{\Omega_1}{2} & 0 & -\gamma_{32} & 0 \\ -\frac{\Omega_2}{2} & \frac{\Omega_2}{2} & 0 & \frac{\Omega_1}{2} & \delta^2 & 0 & 0 & -\frac{\gamma_{21}+\gamma_{32}}{2} \end{pmatrix} \begin{pmatrix} \rho_{22} \\ \rho_{33} \\ \Re\mathfrak{e}\rho_{21} \\ \Re\mathfrak{e}\rho_{31} \\ \Re\mathfrak{e}\rho_{32} \\ \Im\mathfrak{m}\rho_{21} \\ \Im\mathfrak{m}\rho_{31} \\ \Im\mathfrak{m}\rho_{32} \end{pmatrix} - \begin{pmatrix} 0 \\ 0 \\ 0 \\ 0 \\ 0 \\ 0 \\ \frac{1}{2}\Omega_1 \\ 0 \\ 0 \end{pmatrix}.$$

The steady state solution of this equations has complicated expressions, and they will not be shown here.

2.5.1 Autler-Townes Splitting

Let us separate the Hamiltonian 2.11 in three parts

$$\hat{\tilde{H}} = \hat{\tilde{H}}_0 + \hat{\tilde{H}}_1 + \hat{\tilde{H}}_2 = \hbar \begin{pmatrix} 0 & 0 & 0 \\ 0 & \omega_2-\omega_1 & 0 \\ 0 & 0 & \omega_3-\omega_1 \end{pmatrix} + \hbar \begin{pmatrix} 0 & \frac{1}{2}\Omega_1 & 0 \\ \frac{1}{2}\Omega_1 & -\omega^1 & 0 \\ 0 & 0 & -\omega^1 \end{pmatrix} + \hbar \begin{pmatrix} 0 & 0 & 0 \\ 0 & 0 & \frac{1}{2}\Omega_2 \\ 0 & \frac{1}{2}\Omega_2 & -\omega^2 \end{pmatrix}$$

associated with the atom, the first field and the second field respectively. We may thus consider the second field to be a perturbation (not necessarily small) to a Hamiltonian $\hat{\tilde{H}}_0' = \hat{\tilde{H}}_0 + \hat{\tilde{H}}_1$. The energies of the eigenstates of this Hamiltonian (that the ω^2 frequency will probe) are

$$E_- = \hbar\left(\frac{-\delta_1 - \sqrt{\Omega_1^2+\delta_1^2}}{2}\right), \qquad E_+ = \hbar\left(\frac{-\delta_1 + \sqrt{\Omega_1^2+\delta_1^2}}{2}\right), \qquad E_3 = -\hbar(\omega^1-\omega_3+\omega_1) = \hbar(\omega_{32}-\delta_1).$$

Figure 2-2a shows the overall dependance of these eigenvalues. For a given Ω_1 the detuning $\delta_1 > 0$ leads to a negative E_- and zero E_+, and the converse for $\delta_1 < 0$ (very high E_+ and zero E_-). The corresponding eigenvectors are

$$|-\rangle = \begin{pmatrix} \frac{\Omega_1^2}{2\left(\Omega_1^2+\delta_1^2-\delta_1\sqrt{\Omega_1^2+\delta_1^2}\right)} \\ \frac{-\Omega_1\left(\delta_1-\sqrt{\Omega_1^2+\delta_1^2}\right)}{2\left(\Omega_1^2+\delta_1^2-\delta_1\sqrt{\Omega_1^2+\delta_1^2}\right)} \\ 0 \end{pmatrix}, \qquad |+\rangle = \begin{pmatrix} \frac{\Omega_1^2}{2\left(\Omega_1^2+\delta_1^2+\delta_1\sqrt{\Omega_1^2+\delta_1^2}\right)} \\ \frac{-\Omega_1\left(\delta_1+\sqrt{\Omega_1^2+\delta_1^2}\right)}{2\left(\Omega_1^2+\delta_1^2+\delta_1\sqrt{\Omega_1^2+\delta_1^2}\right)} \\ 0 \end{pmatrix}, \qquad |3\rangle = \begin{pmatrix} 0 \\ 0 \\ 1 \end{pmatrix}.$$

These $|\pm\rangle$ are called *Autler-Townes doublets* [65]. This means that the second field will be resonant with transitions $|\pm\rangle \to |3\rangle$ when

$$\omega^2 = \omega_\pm^2 = (E_3 - E_\pm)/\hbar = \omega_{32} - \delta_1 - \frac{-\delta_1 \pm \sqrt{\Omega_1^2 + \delta_1^2}}{2} = \omega_{32} - \frac{\delta_1}{2} \mp \frac{\sqrt{\Omega_1^2 + \delta_1^2}}{2}$$

subtracting ω_{32} from this equation gives us what the detunings δ_2 must be

$$\delta_\pm^2 = -\frac{\delta_1}{2} \mp \frac{\sqrt{\Omega_1^2 + \delta_1^2}}{2}.$$

The more intuitive picture that the second field is in resonance when $\omega^2 = \omega_3 - \omega_2$ ($\delta_2 = 0$) is thus valid when $\delta_1 = \Omega_1 = 0$. This is a good approximation in many cases in spectroscopy, but in this thesis the dependance of spectra on these parameters will be explored.

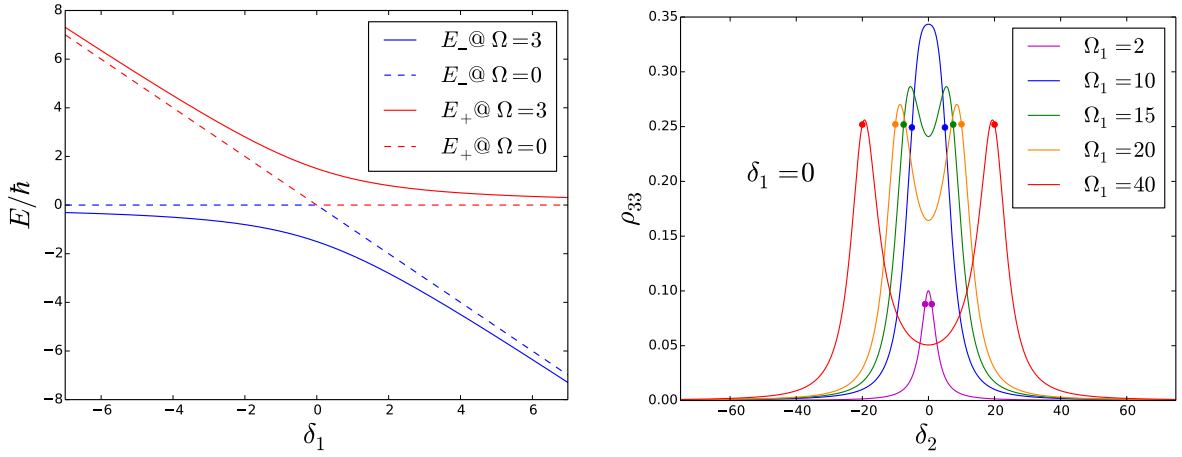

Figure 2-2: The overall tendency of spectra for $\gamma_{21} = 6,\ \gamma_{32} = 1,\ \Omega_2 = 5$.

In figure 2-2b) ρ_{33} in the steady state is shown for various parameter combinations. At this point ρ_{33} will be regarded directly as a *spectrum*, this will be justified in section 3.3. For each of these spectra the position of each peak as predicted above is shown as a point. Notice that the $|+\rangle \to |3\rangle$ peak has the smallest resonant frequency, and thus will appear to the left of the $|-\rangle \to |3\rangle$ peak. As the power (represented by Ω_1) grows, the peak becomes higher and at some point it splits into two peaks. This is known as *Autler-Townes Splitting* or the *AC Stark effect* (ATS).

Figure 2-3a) shows how ATS behaves when $\delta_1 < 0$. As the power increases, the peak grows, but instead of being split, it develops a *shoulder* that eventually becomes a second peak. The peaks start with different heights, and as power goes up they become more symmetric.

On figure 2-3b) the dependance on δ_1 is examined leaving Ω_1 unchanged. At zero detuning both peaks are of the same height, and as it increases the $|-\rangle \to |3\rangle$ peak becomes higher and the $|+\rangle \to |3\rangle$ peak becomes smaller. Also, the midpoint of the peaks is displaced and is always at

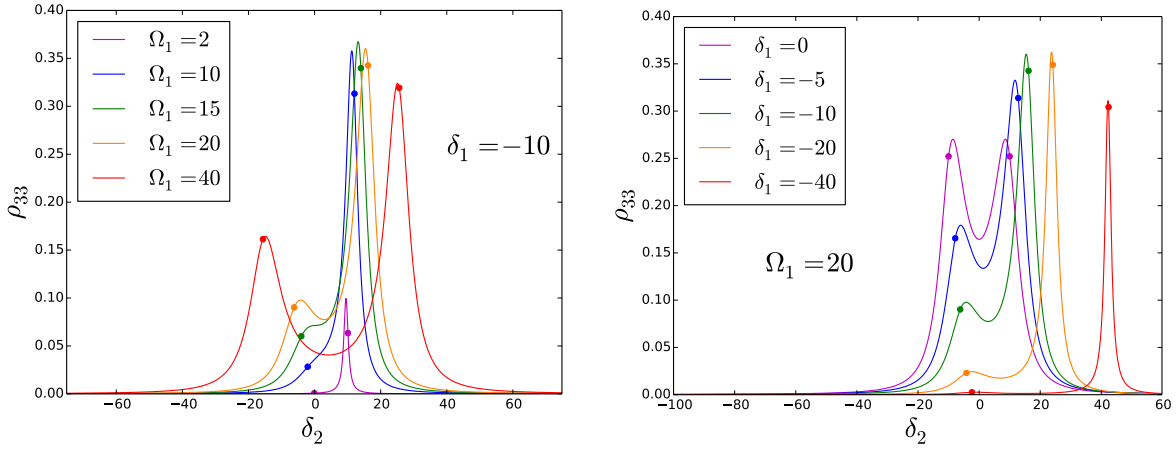

Figure 2-3: The overall tendency of spectra for $\gamma_{21} = 6,\ \gamma_{32} = 1,\ \Omega_2 = 5$.

$(\delta_+^2 + \delta_-^2)/2 = -\delta_1/2$ just as the theory shows.

Chapter 3

The Rubidium Atom

The previous chapter dealt with a generic hydrogen-like atom, however the quantities that describe the atom: energy levels ω_i, the transition frequencies ω_{ij}, the matrix elements of the dipole operator er_{pij}, and the decay frequencies γ_{ij} were not specified. These quantities are calculated from various other measured quantities.

In order to refer to individual atomic states, a mixed notation will be used from now on. In the previous chapter a single index i (or j) was used to label the states according to their energy. Since the atom has a structure that is better described by quantum numbers, quantum numbers $|N_i L_i S_i J_i I_i F_i M_i\rangle$ will be used to make reference to this structure while keeping in mind a global i index.

3.1 Atomic Structure

Since the rubidium atom has all the lower shells filled and only a single valence electron, as a first approximation it can be treated as hydrogen-like system. In other words, interactions of the electrons in the lower shells with the radiation fields will not be considered. The states can be labelled using quantum numbers of the valence electron only

$$|\psi\rangle_{\text{atom}} = |N, L, S, J, I, F, M_F\rangle.$$

For alkali atoms S is always $\frac{1}{2}$, so from now on it will not be shown explicitly in Dirac notation unless it is needed. The nuclear angular momentum $I = 5/2, (3/2)$ for ^{85}Rb (^{87}Rb) will also be left implicit in most cases from now on. Other quantum numbers may also be ignored when states are referenced collectively.

States are commonly abbreviated using Russel-Saunders notation, which states first N^{2S+1}, then L in spectroscopic notation $L = S, P, D, F, G, \ldots \equiv 0, 1, 2, 3, 4, \ldots$ followed by J as a subindex [37].

For instance, the ground state of rubidium is

$$|N=5, L=0, S=\frac{1}{2}, J=\frac{1}{2}\rangle = 5^2S_{1/2}.$$

However, the superindex will not be shown from now on, since it is always 2 for alkali atoms.

The energy of these states may be calculated numerically from first principles, but this is outside the scope of this thesis. Instead, we will directly use experimental data to model the atomic structure. The spin-orbit interaction Hamiltonian breaks the degeneration of $|N, L\rangle$ states and produces different energies for $|N, L, J\rangle$ that are known as the *fine structure*. These values are taken from [60].

The coupling with the nucleus spin further breaks degeneration and produces the *hyperfine structure* through the Hamiltonian [16] [3] [5] [25]

$$\hat{H}_{\text{hfs}} = A_{\text{hfs}} \vec{I} \cdot \vec{J} + B_{\text{hfs}} \frac{3(\vec{I} \cdot \vec{J})^2 + \frac{3}{2}(\vec{I} \cdot \vec{J}) - I(I+1)J(J+1)}{2I(2I-1)J(2J-1)} + \dots$$

Where A_{hfs} and B_{hfs} are respectively known as the magnetic dipole constant and the electric quadrupole constant for a particular fine structure energy level and isotope. This Hamiltonian produces energy shifts

$$\Delta E_{\text{hfs}} = A_{\text{hfs}} K + B_{\text{hfs}} \frac{\frac{3}{2}K(K+1) - 2I(I+1)J(J+1)}{2I(2I-1)J(2J-1)} + \dots$$

where

$$K = F(F+1) - I(I+1) - J(J+1).$$

The values of A_{hfs} and B_{hfs} are taken from [60] and [3]. In this manner the energy $\hbar\omega_i$ of each $|N_i, L_i, J_i, I_i, F_i\rangle$ can be calculated. The structure of ^{85}Rb (^{87}Rb) is shown in figure 3-1 (3-2). Each hyperfine multiplet is shown labelled by the corresponding F. The frequency differences between hyperfine levels are indicated between them (in absolute frequency). Whenever possible, this differences are shown with distances in proportion.

The Autler-Townes splitting from the high intensity of the field driving the transition $5S_{1/2}F = 3(2) \rightarrow 5P_{3/2}F = 4(3)$ is shown schematically as split levels displaced by $-\delta^1/2$ as explained in section 2.5.1.

The excitations driven by the laser fields of the experiment described in 5 are shown as arrows. The transitions allowed by the electric dipole selection rules (derived in appendix F) are shown as wavy lines connecting fine-structure multiplets. The light from the spontaneous decay shown in purple has a wavelength of 420 nm. Other spontaneous decays of importance are shown in red, and the rest in gray to indicate that they occur.

From these energies, the $\omega_{ij} = \omega_i - \omega_j$ matrix required by the theory derived in chapter 2 can be

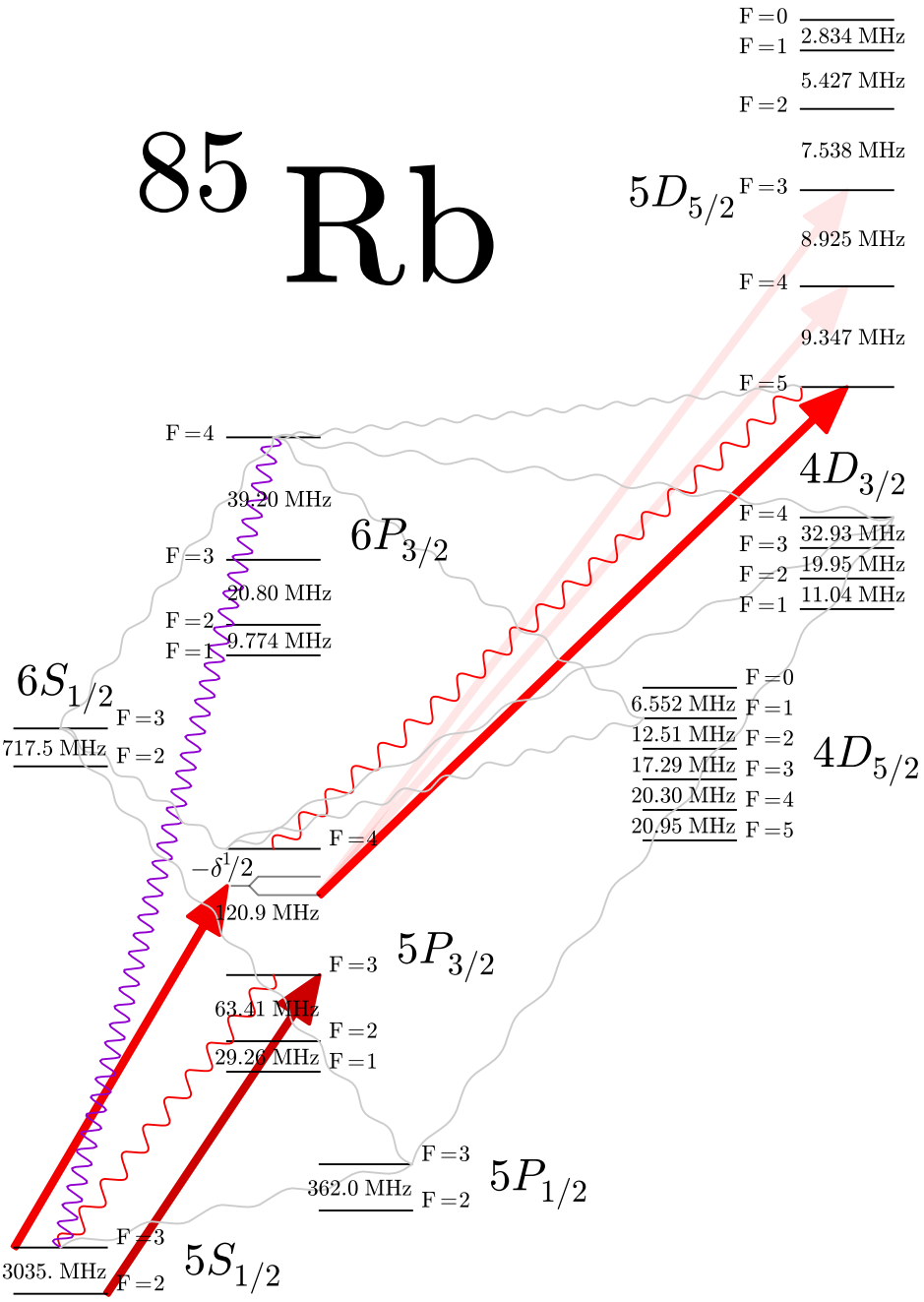

Figure 3-1: The hyperfine structure of ^{85}Rb. Each hyperfine multiplet is shown labelled by the corresponding F. The frequency differences between hyperfine levels are indicated between them (in absolute frequency). Whenever possible, this differences are shown with distances in proportion. The excitations driven by the laser fields of the experiment described in are shown as arrows; the cooling laser coupling the states $5S_{1/2}F = 3 \rightarrow 5P_{3/2}F = 4$ (with detuning $-\delta^1$), the repump laser coupling states $5S_{1/2}F = 2 \rightarrow 5P_{3/2}F = 3$, and the probe laser coupling states $5P_{3/2}F = 4 \rightarrow 5P_{3/2}F = 5, 4, 3$. When ATS is present, the $5P_{3/2}F = 4$ multiplet is split into $|\pm\rangle$ states. This doublet states are coupled by the probe laser to the $5D_{5/2}$ multiplet. Spontaneous decays are shown as wavy lines, the repump spontaneous decay $5P_{3/2}F = 3 \rightarrow 5S_{1/2}F = 3$ is shown in red, as is the return decay $5D_{5/2} \rightarrow 5P_{3/2}$. The 420 nm spontaneous decay detected by the photomultiplier tubes is shown in purple.

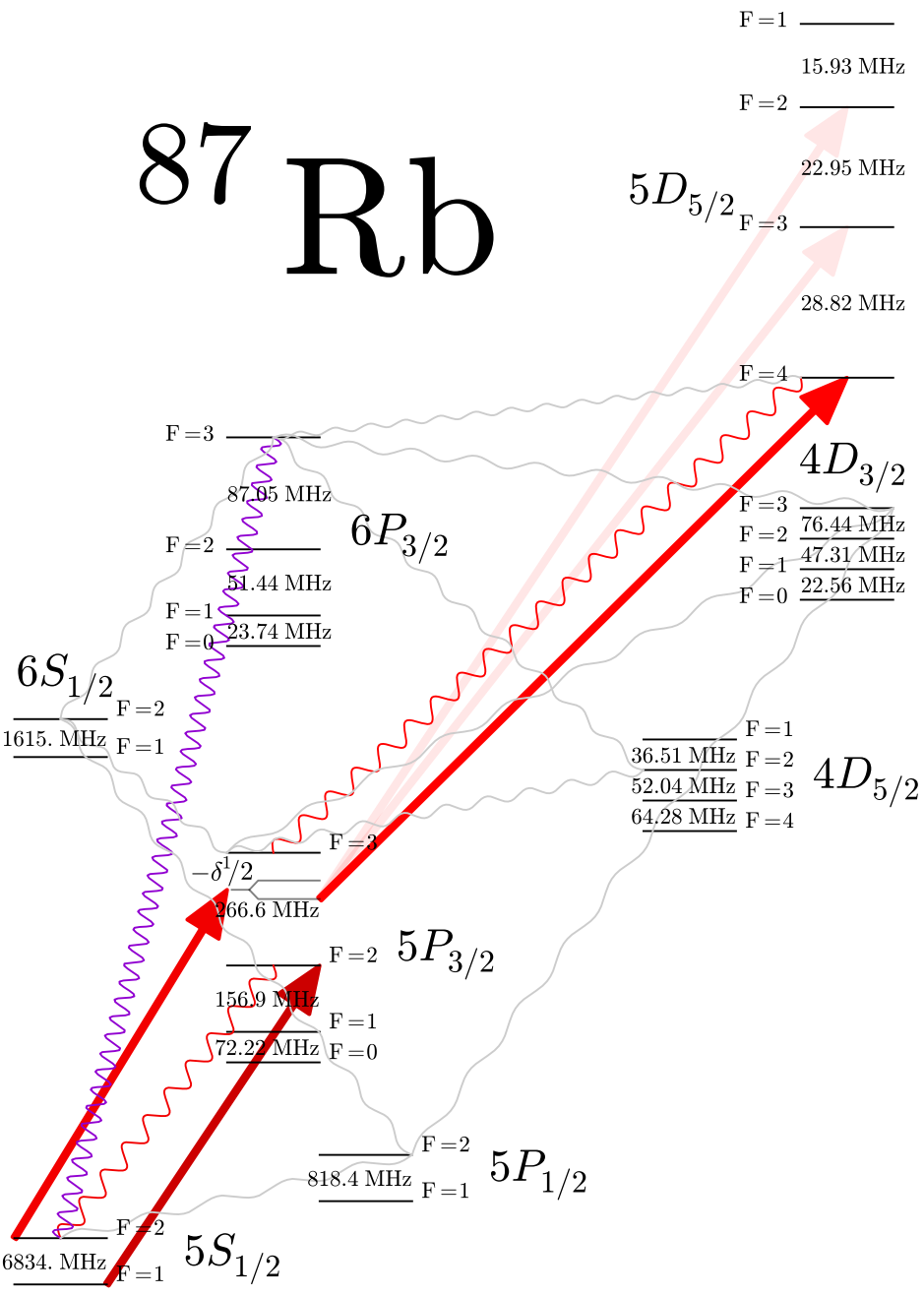

Figure 3-2: The hyperfine structure of ^{85}Rb. Each hyperfine multiplet is shown labelled by the corresponding F. The frequency differences between hyperfine levels are indicated between them (in absolute frequency). Whenever possible, this differences are shown with distances in proportion. The excitations driven by the laser fields of the experiment described in are shown as arrows; the cooling laser coupling the states $5S_{1/2}F = 2 \rightarrow 5P_{3/2}F = 3$ (with detuning $-\delta^1$), the repump laser coupling states $5S_{1/2}F = 1 \rightarrow 5P_{3/2}F = 2$, and the probe laser coupling states $5P_{3/2}F = 3 \rightarrow 5P_{3/2}F = 4, 3, 2$. When ATS is present, the $5P_{3/2}F = 3$ multiplet is split into $|\pm\rangle$ states. This doublet states are coupled by the probe laser to the $5D_{5/2}$ multiplet. Spontaneous decays are shown as wavy lines, the repump spontaneous decay $5P_{3/2}F = 2 \rightarrow 5S_{1/2}F = 2$ is shown in red, as is the return decay $5D_{5/2} \rightarrow 5P_{3/2}$. The 420 nm spontaneous decay detected by the photomultiplier tubes is shown in purple.

calculated. The full ω_{ij} matrix is shown in figure 3-3 (3-4) for ^{85}Rb (^{87}Rb). In these matrices red lines have been traced to separate fine structure states, and blue lines to separate hyperfine states. Blocks of similar colour correspond to transitions of similar resonant frequencies. In particular, the two-photon transition

$$5S_{1/2} \rightarrow 5P_{3/2} \rightarrow 5D_{5/2}$$

is the focus of this thesis, and the steps are resonant at 780.2414 nm and 775.9786 nm.

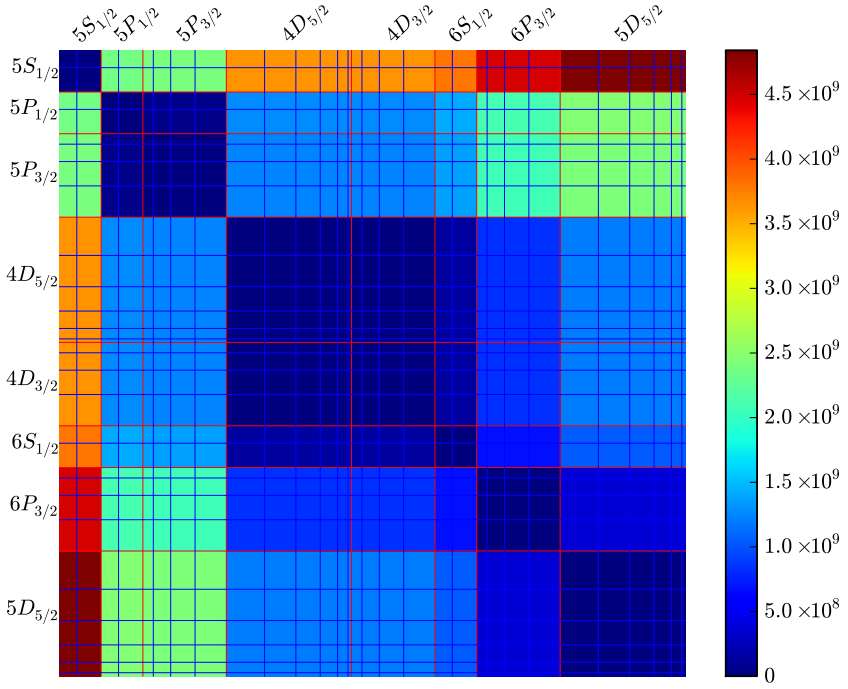

Figure 3-3: The transition frequencies ω_{ij} for ^{85}Rb in rad$/s$.

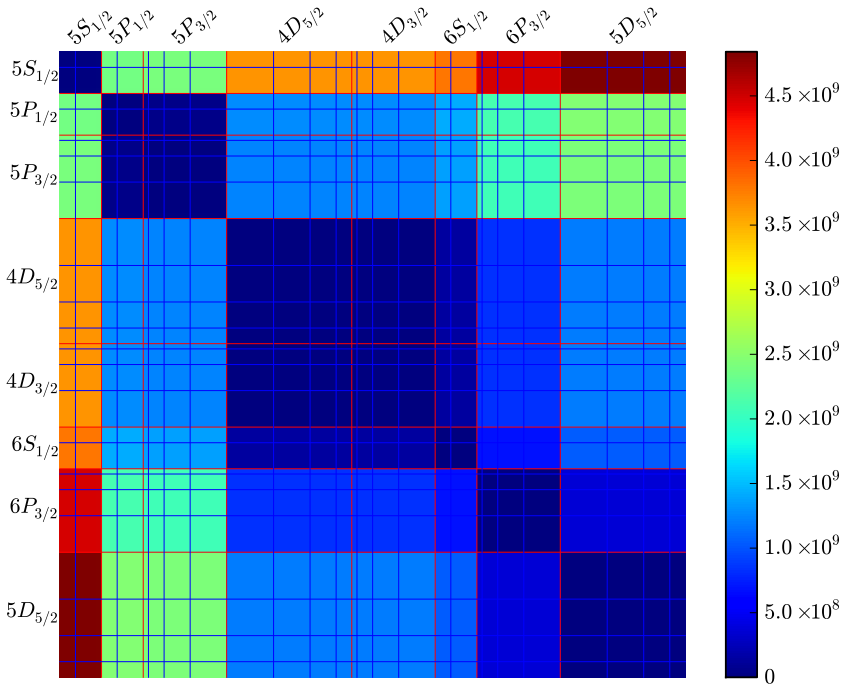

Figure 3-4: The transition frequencies ω_{ij} for ^{87}Rb in rad$/s$.

3.2 Derived quantities

However, not all transitions shown in figures 3-3 and 3-4 are allowed by the electric dipole Hamiltonian derived in chapter 2. The transition $|i\rangle \rightarrow |j\rangle$ is allowed only if the corresponding matrix element of the interaction Hamiltonian $e\vec{E}\cdot\widehat{\vec{r}}$ is non-zero. We will calculate these matrix elements in the helicity basis to exploit the symmetries of Wigner symbols.

In appendix D the matrix elements of the dipole operator are reduced to the following expression

$$\begin{aligned}\langle N_i L_i J_i F_i M_i|T^1_p(\widehat{\vec{r}})|N_j L_j J_j F_j M_j\rangle &= (-1)^{F_i-M_i+J_i+I+F_j+1}\sqrt{(2F_j+1)(2F_i+1)} \\ &\times \begin{pmatrix} F_i & 1 & F_j \\ -M_i & p & M_j \end{pmatrix} \begin{Bmatrix} J_i & F_i & I \\ F_j & J_j & 1 \end{Bmatrix} (N_i L_i J_i||T^1(\widehat{\vec{r}})||N_j L_j J_j)\end{aligned} \tag{3.1}$$

where $\begin{pmatrix} F_i & 1 & F_j \\ -M_i & p & M_j \end{pmatrix}$, $\begin{Bmatrix} J_i & F_i & I \\ F_j & J_j & 1 \end{Bmatrix}$, and $(N_i L_i J_i||T^1(\widehat{\vec{r}})||N_j L_j J_j)$ are a Wigner 3-j symbol, a Wigner 6-j symbol, and the reduced matrix element among fine states. These are also defined in appendix D.

In the calculation of these matrix elements it is very important to consider that the reduced matrix elements are not symmetric under exchange of their arguments, but rather follow the symmetry relation [17]

$$(N_i L_i J_i||T^1(\widehat{\vec{r}})||N_j L_j J_j) = (-1)^{J_i-J_j}(N_j L_j J_j||T^1(\widehat{\vec{r}})||N_i L_i J_i)^*, \tag{3.2}$$

although they will be taken to be real in this thesis.

The reduced matrix elements can be calculated from the decay rates Γ_{ij} among fine multiplets

$$(N_i L_i J_i||T^1(\overrightarrow{\hat{r}})||N_j L_j J_j) = \left(\frac{3\pi\hbar c^3\varepsilon_0}{\omega_{ij}^3 e^2}(2J_i+1)\Gamma_{ij}\right)^{1/2}. \tag{3.3}$$

For a detailed derivation of this formula see appendix E.

Replacing 3.1 and 3.3 in E.1 the decay frequencies can be calculated as

$$\begin{aligned}\gamma_{ij} &= \tfrac{\omega_{ij}^3 e^2}{3\pi\hbar c^3\varepsilon_0}\textstyle\sum_p \left|\langle N_i L_i J_i F_i M_i|T^1_p(\widehat{\vec{r}})|N_j L_j J_j F_j M_j\rangle\right|^2 \\ &= \tfrac{\omega_{ij}^3 e^2}{3\pi\hbar c^3\varepsilon_0}(2F_j+1)(2F_i+1)\begin{Bmatrix} J_i & F_i & I \\ F_j & J_j & 1 \end{Bmatrix}^2 |(N_i L_i J_i||T^1(\widehat{\vec{r}})||N_j L_j J_j)|^2 \textstyle\sum_p \begin{pmatrix} F_i & 1 & F_j \\ -M_i & p & M_j \end{pmatrix}^2 \\ &= \Gamma_{ij}(2J_i+1)(2F_j+1)(2F_i+1)\begin{Bmatrix} J_i & F_i & I \\ F_j & J_j & 1 \end{Bmatrix}^2 \textstyle\sum_p \begin{pmatrix} F_i & 1 & F_j \\ -M_i & p & M_j \end{pmatrix}^2.\end{aligned} \tag{3.4}$$

The Γ_{ij} for rubidium and their reference to experiments or calculations are listed in table 3.1

The measurements cited are for total decay rates Γ_i, however the branching ratios (the ratios to

$\Gamma_{ij}/2\pi$	$5S_{1/2}$	$5P_{1/2}$	$5P_{3/2}$	$4D_{5/2}$	$4D_{3/2}$	$6S_{1/2}$	$6P_{3/2}$	$5D_{5/2}$	$\Gamma_i/2\pi$	Ref
$5S_{1/2}$	×	−5.746	−6.065	×	×	×	−0.299	×	×	
$5P_{1/2}$	5.746	×	×	×	−1.5	−1.746	×	×	5.746	[66]
$5P_{3/2}$	6.065	×	×	−1.7	−0.3	−1.746	×	−0.493802	6.065	[66]
$4D_{5/2}$	×	×	1.7	×	×	×	−0.0286	×	1.7	[58]
$4D_{3/2}$	×	1.5	0.3	×	×	×	−0.2574	×	1.5	[58]
$6S_{1/2}$	×	1.746	1.746	×	×	×	−0.715	×	3.492	[26]
$6P_{3/2}$	0.299	×	×	0.0286	0.2574	0.715	×	−0.173498	1.3	[70]
$5D_{5/2}$	×	×	0.493802	×	×	×	0.173498	×	0.6673	[64]

Table 3.1: Total decay frequencies $\Gamma_{ij}/2\pi$ and $\Gamma_i/2\pi$ for all involved multiplets in MHz.

which Γ_i is divided into Γ_{ij}) are calculated in [58]. Notice that since 3.3 does not contain reference to F quantum numbers (and therefore to nuclear angular momentum coupling), these numbers are the same for both isotopes, as are the reduced matrix elements $(N_iL_iJ_i||T^1(\widehat{r})||N_jL_jJ_j)$.

The places marked with a × are forbidden under electric-dipole rules (see appendix F) but not necessarily zero. In this thesis however, they will be neglected.

We can thus obtain the reduced matrix elements from Γ_{ij} through 3.3 and 3.2, and are shown in table 3.2.

$(N_iL_iJ_i\|\|T^1(\widehat{r})\|\|N_jL_jJ_j)$	$5S_{1/2}$	$5P_{1/2}$	$5P_{3/2}$	$4D_{5/2}$	$4D_{3/2}$	$6S_{1/2}$	$6P_{3/2}$	$5D_{5/2}$
$5S_{1/2}$	×	4.231	−8.453	×	×	×	−0.7421	×
$5P_{1/2}$	4.231	×	×	×	−10.935	5.012	×	×
$5P_{3/2}$	8.453	×	×	−13.027	3.648	−3.718	×	−2.537
$4D_{5/2}$	×	×	13.027	×	×	×	−1.645	×
$4D_{3/2}$	×	10.935	3.648	×	×	×	6.045	×
$6S_{1/2}$	×	5.012	3.718	×	×	×	−19.019	×
$6P_{3/2}$	0.7421	×	×	1.645	6.045	19.019	×	−26.343
$5D_{5/2}$	×	×	2.537	×	×	×	26.343	×

Table 3.2: Reduced matrix elements $(N_iL_iJ_i||T^1(\widehat{r})||N_jL_jJ_j)$ in Bohr radii ($a_0 = 5.2917721067(12) \times 10^{-11}m$).

And γ_{ij} are calculated from Γ_{ij} through 3.4. The complete matrix γ_{ij} is shown in figure 3-5 (3-6) for ^{85}Rb (^{87}Rb). These matrices show which transitions are allowed by the electric dipole approximation as inherited to γ_{ij} by 6j symbols in 3.4.

The matrix elements r_{pij} can be calculated from reduced matrix elements through 3.1. The matrix elements are shown in figures 3-7, 3-8, 3-9 (3-10, 3-11, 3-12) for ^{85}Rb (^{87}Rb). These matrices carry further information about the relation of transitions to the light polarization. According to 2.4 the component $-p$ of the electric field (represented by $Y^{l(\pm)}_{-p}$) couples only with r_{pij}. Examining A.2 we can see that $\vec{E}^l$ can be decomposed in three terms corresponding to light linearly polarized along the $\hat{z}$ axis ($p = 0$) and circularly polarized light of either hand in the x-y plane ($p = \pm 1$). Therefore r_{pij} shows the coupling of these polarizations to the $|i\rangle \to |j\rangle$ transitions.

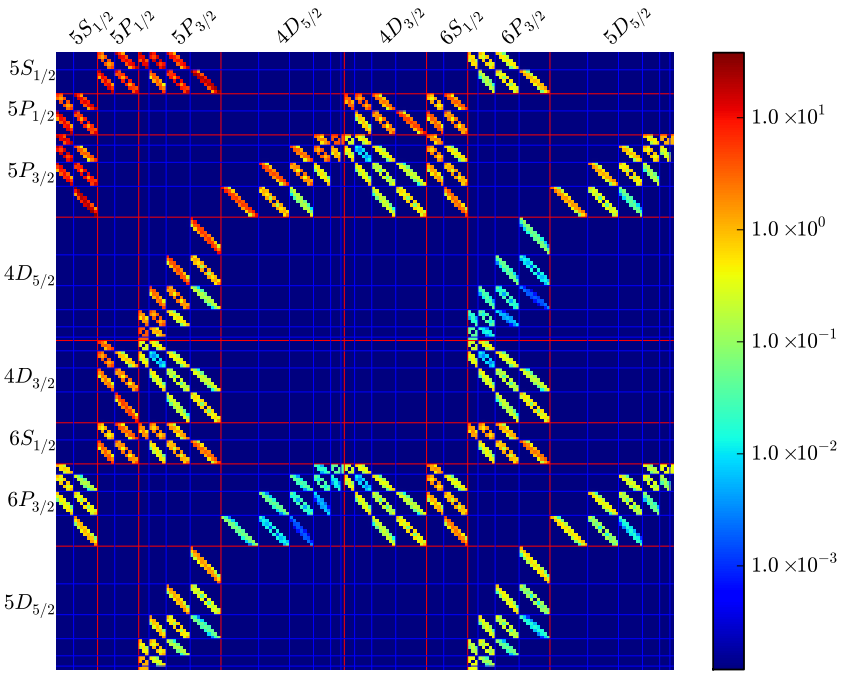

Figure 3-5: The decay frequencies γ_{ij} for ^{85}Rb in rad$/s$.

Linearly polarized light ($p = 0$) can only drive transitions with $M_{F_i} - M_{F_j} = 0$. While circularly polarized light ($p = \pm 1$) can only drive transitions with $M_{F_i} - M_{F_j} = \mp 1$ (for $i > j$). This M_F distinction is inherited to r_{pij} by the 3j symbols in 3.1.

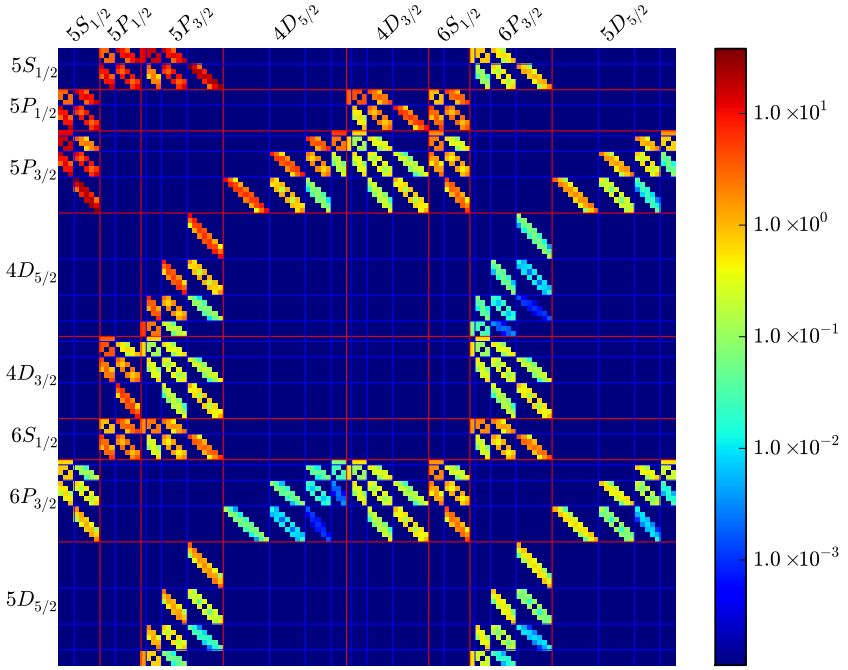

Figure 3-6: The decay frequencies γ_{ij} for ^{87}Rb in rad$/s$.

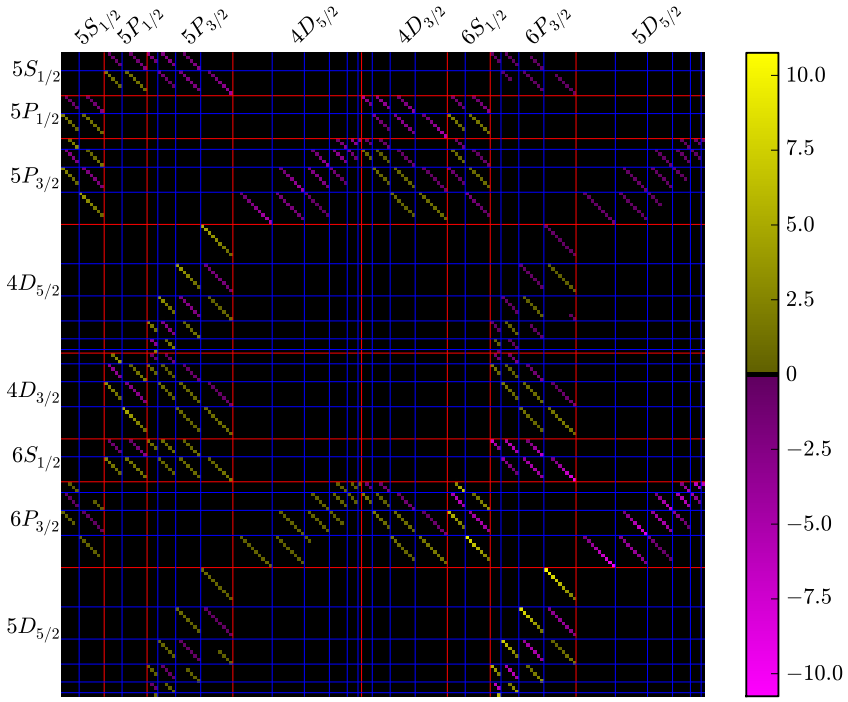

Figure 3-7: The matrix elements of the dipole operator r_{-1ij} for ^{85}Rb in Bohr radii.

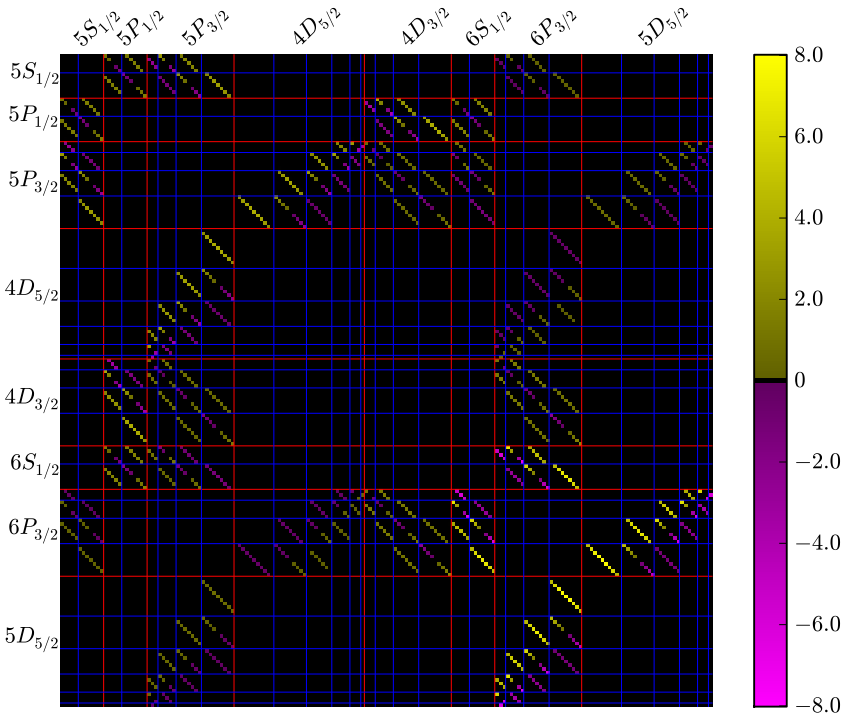

Figure 3-8: The matrix elements of the dipole operator r_{0ij} for ^{85}Rb in Bohr radii.

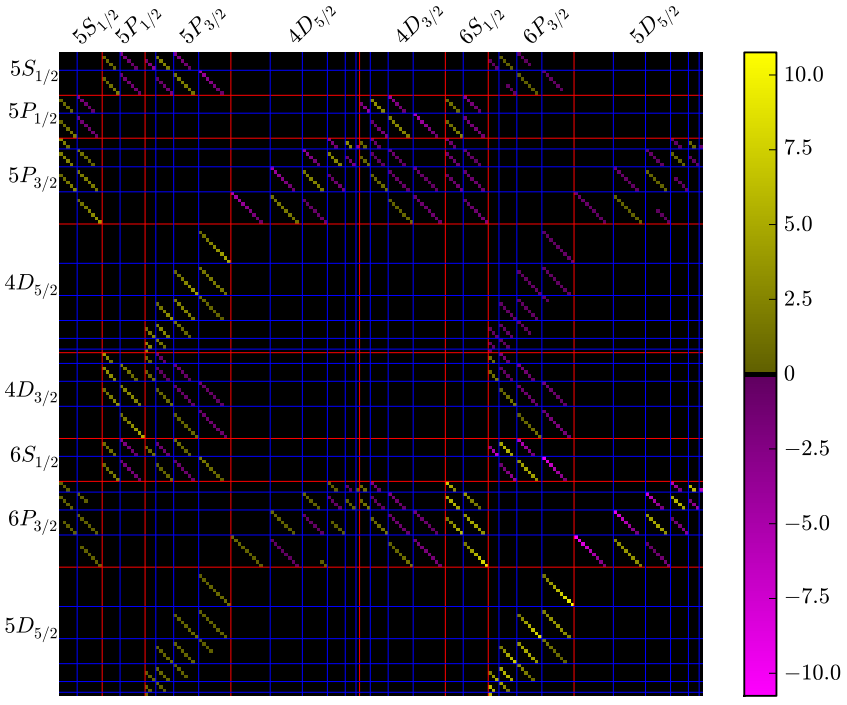

Figure 3-9: The matrix elements of the dipole operator r_{1ij} for ^{85}Rb in Bohr radii.

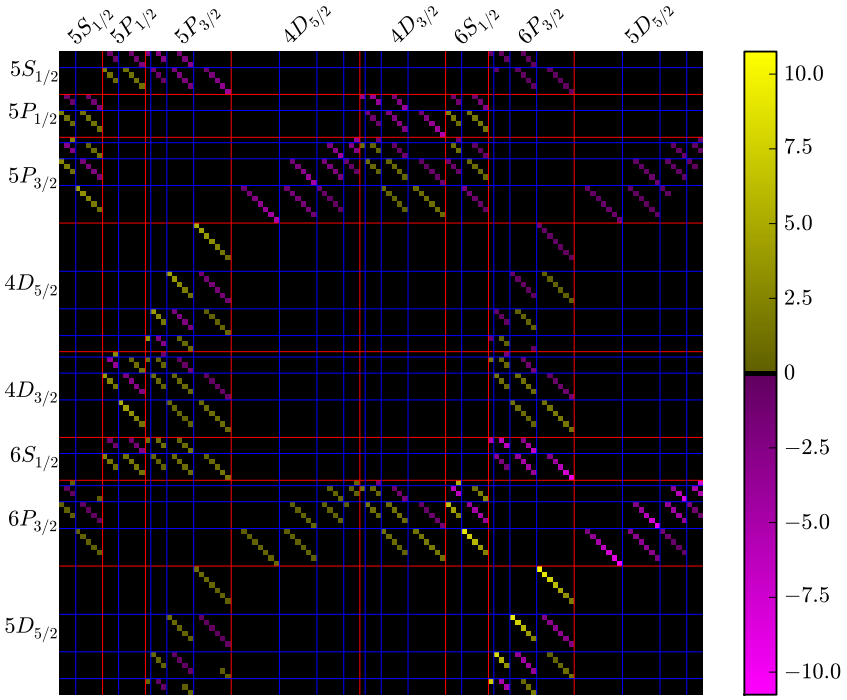

Figure 3-10: The matrix elements of the dipole operator r_{-1ij} for ^{87}Rb in Bohr radii.

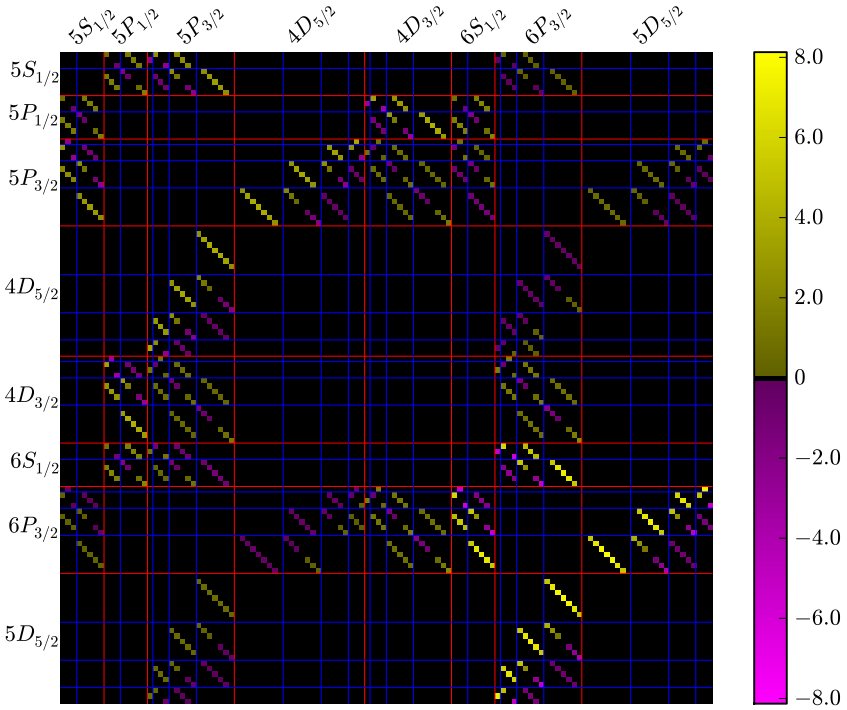

Figure 3-11: The matrix elements of the dipole operator r_{0ij} for ^{87}Rb in Bohr radii.

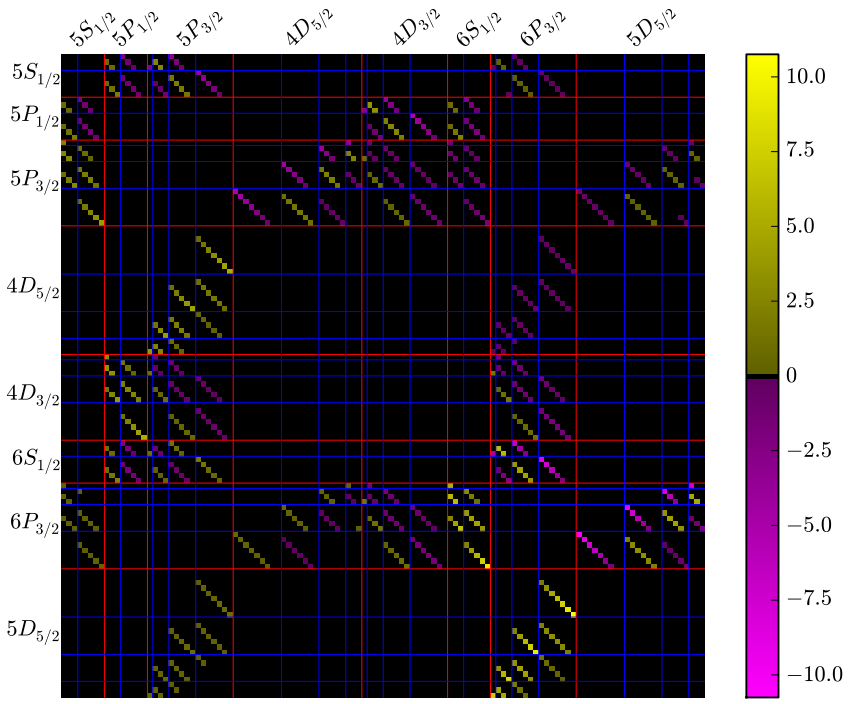

Figure 3-12: The matrix elements of the dipole operator r_{1ij} for ^{87}Rb in Bohr radii.

3.3 Fluorescence spectra

We need a way to calculate the power carried by the spontaneous fluorescence. In particular, we are interested in the spontaneous decay from the transition $6P_{3/2} \rightarrow 5S_{1/2}$. Each state $|i\rangle$ in $6P_{3/2}$ decays to states $|j\rangle$ in $5S_{1/2}$ at a rate γ_{ij} with each decay carrying energy $\hbar\omega_{ij}$. The total power is thus

$$P_\phi = N \sum_{ij} \hbar\omega_{ij}\gamma_{ij}\rho_{ii}$$

where i is an index that runs over the states $6P_{3/2}$ and j over the states $5S_{1/2}$ and N is the number of atoms that form the statistical ensemble $\hat{\rho}$ (or approximately the number of atoms trapped). This can be seen as an observable $\hat{P}_\phi$ in quantum mechanics

$$P_\phi = \mathrm{Tr}[\hat{P}_\phi\hat{\rho}] = \mathrm{Tr}\left[\left(\sum_{ij} N\hbar\omega_{ij}\gamma_{ij}|i\rangle\langle i|\right)\hat{\rho}\right]$$

On another side, if each ω_{ij} is considered approximately equal, we can define the number of photons per atom per second as

$$\phi = \sum_{ij} \gamma_{ij}\rho_{ii}. \tag{3.5}$$

3.4 Broadening

Up to this point we have considered the atom to be driven by strictly monochromatic fields of frequencies ω^l, and described the calculation of the density matrix $\hat{\rho}(t, \omega^l)$ associated with this frequencies. However in practice the laser emission spectra have a certain frequency distribution $f(\omega) = g(\omega - \omega^l)$ around this central value. Therefore the density matrix is a statistical ensemble of density matrices associated with each frequency weighed by this (normalized) frequency distribution

$$\hat{\rho}(t) = \int_{-\infty}^{\infty} \hat{\rho}(t,\omega)f(\omega)d\omega = \int_{-\infty}^{\infty} \hat{\rho}(t,\omega)g(\omega - \omega^l)d\omega.$$

If the zero-centred distribution g are even ($g(\omega) = g(-\omega)$) as is the case of laser sources with Gaussian distributions, then this is simply the convolution $\hat{\rho}(t,\omega) \oplus g(\omega)$ of the density matrix with the zero-centred frequency distribution, so we do not need to calculate many density matrix solutions to get a weighed density matrix. Instead, numerically calculating the convolution, for instance with a Gaussian distribution, is computationally very cheap through a fast Fourier transform.

Also, other broadening components such as the Doppler effect due to the velocity distribution of the atoms can be considered in this manner. Since the cloud of cold rubidium atoms that is examined in this thesis is a dilute gas, the broadening due to collisions between atoms will not be considered explicitly here. Notice that the broadening effects discussed here do not account for all

the width of the atomic transition lines, but rather to broadening additional to the natural widths γ_{ij} and to power broadening.

The convolution is associative $(f(\omega)\oplus g_1(\omega))\oplus g_2(\omega) = f(\omega)\oplus(g_1(\omega)\oplus g_2(\omega))$, and the convolution of two Gaussian distributions with standard deviations σ_1, σ_2 is another Gaussian distribution with standard deviation $\sigma = \sqrt{\sigma_1^2 + \sigma_2^2}$.

Thus we can consider all broadening effects using a single convolution with an effective Gaussian frequency distribution with standard deviation

$$\sigma_{\text{eff}} = \sqrt{\sum_l (\sigma_T^l)^2 + (\sigma^l)^2} = \sqrt{(\sigma_T)^2 + \sigma_{\text{lasers}}^2}$$

due to each of the laser linewidths σ^l and to the standard deviation σ_T due to the Doppler effect. This Doppler broadening is due to a Maxwell-Boltzman velocity distribution for atoms with temperature T

$$f(v) = \left(\frac{M}{2\pi k_B T}\right)^{1/2} \exp\left(-\frac{Mv^2}{2k_B T}\right),$$

where v is the atom velocity along the direction of a beam. The Doppler frequency shift (in the non-relativistic limit) is $\omega_D^l = \omega^l v/c = k^l v$. The effective frequency has a distribution

$$f(\omega_D^l) = \left(\frac{M(\omega^l)^2}{2\pi k_B T c^2}\right)^{1/2} \exp\left(-\frac{mc^2}{2k_B T(\omega^l)^2}(\omega_D^l)^2\right),$$

which has a standard deviation

$$\sigma_T^l = \frac{\omega^l}{c}\sqrt{\frac{k_B T}{M}}.$$

For a Gaussian distribution with standard deviation σ, the full width at half maximum (FWHM) is $2\sqrt{2\log(2)}\sigma$, therefore the FWHM from each laser is

$$\text{FWHM}_T^l = \frac{2\omega^l}{c}\sqrt{\frac{2\log(2)k_B T}{M}}.$$

and the effective total widening FWHM is

$$\text{FWHM}_{\text{eff}} = \sqrt{\sum_l (\text{FWHM}_T^l)^2 + (\text{FWHM}^l)^2} = \sqrt{\sum_l \frac{8\log(2)(\omega^l)^2}{c^2 M} k_B T + (\text{FWHM}^l)^2}$$

and therefore

$$T = \frac{c^2 M}{8\log(2)k_B \sum_l (\omega^l)^2}\left[\text{FWHM}_{\text{eff}}^2 - \sum_l (\text{FWHM}^l)^2\right] \tag{3.6}$$

which allows the temperature of the atoms to be estimated from the effective broadening if the widths FWHM^l of each laser are known.

Chapter 4

The Magneto-Optical Trap

In this chapter the principles behind the operation of a Magneto-Optical Trap are described. For the sake of simplicity we will consider a two level system (described in section 2.4) to illustrate the physical phenomena involved.

For circularly polarized light σ_+ propagating in the direction $\hat{z}$ of the quantization axis the polarization vectors $\vec{\varepsilon}^{\,l(\pm)} = \hat{e}_{\mp}$, whose only non-zero helicity-basis components are $Y^{l\pm}_{\mp 1} = 1/2$ (see appendix A). The effective Hamiltonian 2.5 couples states $|i\rangle$ and $|j\rangle$ through $\vec{\varepsilon}^{\,l(+)} \cdot \vec{r}_{ij}$ only if $i > j$ and through $\vec{\varepsilon}^{\,l(-)} \cdot \vec{r}_{ij}$ only if $i < j$. Therefore, the only couplings are $r_{1ij}/2$ for $i > j$ and $r_{-1ij}/2$ for $i < j$.

Examining figures 3-9, 3-7, 3-12, and 3-10 it can be seen that these couplings always correspond to transitions $|F, M\rangle \rightarrow |F+1, M+1\rangle$. In other words, circularly polarized light only induces transitions in one direction of the magnetic projections of angular momentum. It is said that it produces *optical pumping*.

In particular, if the circular light is resonant to the $5S_{1/2}F = 3(2) \rightarrow 5P_{3/2}F = 4(2)$ transition of ^{85}Rb (^{87}Rb), the result is that all the population is pumped to the extreme M states $5S_{1/2}F = M = 3(2)$ and $5P_{3/2}F = M = 4(3)$ states; which results in the effective two-state system that we will consider in this chapter. The transition between these states is known as the *cycling transition* because electric dipole transition rules (see appendix F) determine that for radiation resonant to them atoms are periodically excited and lowered to these states (at the Rabi frequency of the effective two-state system).

4.1 Optical Molasses

Each photon that is absorbed by the atom receives momentum $\hbar k = \hbar\omega/c$, since this occurs at a rate $\gamma\rho_{22}$ [21], and force is the rate of momentum transfer, the force light with detuning δ exerts

on the atom is

$$F(\delta) = -\frac{\hbar\omega^1}{c}\frac{\gamma\Omega^2}{2\Omega^2+\gamma^2+4\delta^2},$$

(see section 2.4). However, if the atom has a velocity v opposed to the direction of the beam the Doppler effect will shift the frequency by $\omega^1 v/c$ so the force becomes

$$F(v,\delta) = -\frac{\hbar(\omega^1+\omega^1 v/c)}{c}\frac{\gamma\Omega^2}{2\Omega^2+\gamma^2+4(\omega^1+\omega^1 v/c-\omega_{21})^2}.$$

This is maximal for $v = v_c = -(\omega^1-\omega_{21})c/\omega^1 = -\delta c/\omega^1$, which means that the beam pushes atoms *velocity-selectively*. The atoms are always pushed in the direction of the beam regardless of the velocity they have. However, atoms that move at this optimal velocity have a stronger interaction with the light. In particular, if $\delta < 0$ (that is if the laser beam is *red-detuned* from the atomic transition) atoms moving against the beam are slowed down at a maximal rate, while those moving in the direction of the beam gain speed, but at a much lesser rate.

The optical molasses technique exploits this velocity selectivity by using three pairs of counter-propagating beams in orthogonal directions as shown by the blue arrows in figure 4-1. If the beams are produced by the same source they have the same detuning $\delta < 0$. In the region in which all beams intersect, for all x, y, z components of the velocity of the atom there is always a beam that propagates in the direction opposite to the movement and thus slows it down. The interaction with this opposing beam is enhanced by the detuning, while the interaction with the beam propagating in the same direction as the atom is reduced by the detuning. In this way, the average speed and kinetic energy of a collection of atoms that are strongly resonant with the red detuned light is reduced, therefore lowering the temperature of this velocity selected collection of atoms.

Let us consider the force exerted on an atom with velocity v_z by one such pair of counter-propagating beams along the z axis. For small v_z

$$\begin{aligned} F_z &= F(v_z,\delta) - F(-v_z,\delta) \\ &= F(0,\delta) + (\tfrac{\partial F}{\partial v_z}|_{v=0})v_z - [F(0,\delta) - (\tfrac{\partial F}{\partial v_z}|_{v=0})v_z] \\ &= 2(\tfrac{\partial F}{\partial v_z}|_{v=0})v_z \\ &= \tfrac{2\hbar\Omega^2\gamma(8\delta\omega_{21}-2\Omega^2+4\delta^2-\gamma)(\omega_{21}+\delta)}{(2\Omega^2+\gamma^2+4\delta^2)^2c^2}v_z \end{aligned}$$

This last expression has eight terms involving δ, Ω, γ, and ω_{21} in their numerators. All of these frequencies are of the order of MHz for rubidium and experimental arrangements of our current interest, with the exception of ω_{21} that is of the order of THz, thus the largest term by far is the one proportional to ω_{21}^2, so

$$F_z \simeq \frac{16\hbar\Omega^2\gamma\delta\omega_{21}^2}{(2\Omega^2+\gamma^2+4\delta^2)^2c^2}v_z \simeq \frac{16\hbar\Omega^2\gamma\delta\omega_{21}^2}{(\gamma^2+4\delta^2)^2c^2}v_z = -\alpha v_z = M\dot{v}_z, \tag{4.1}$$

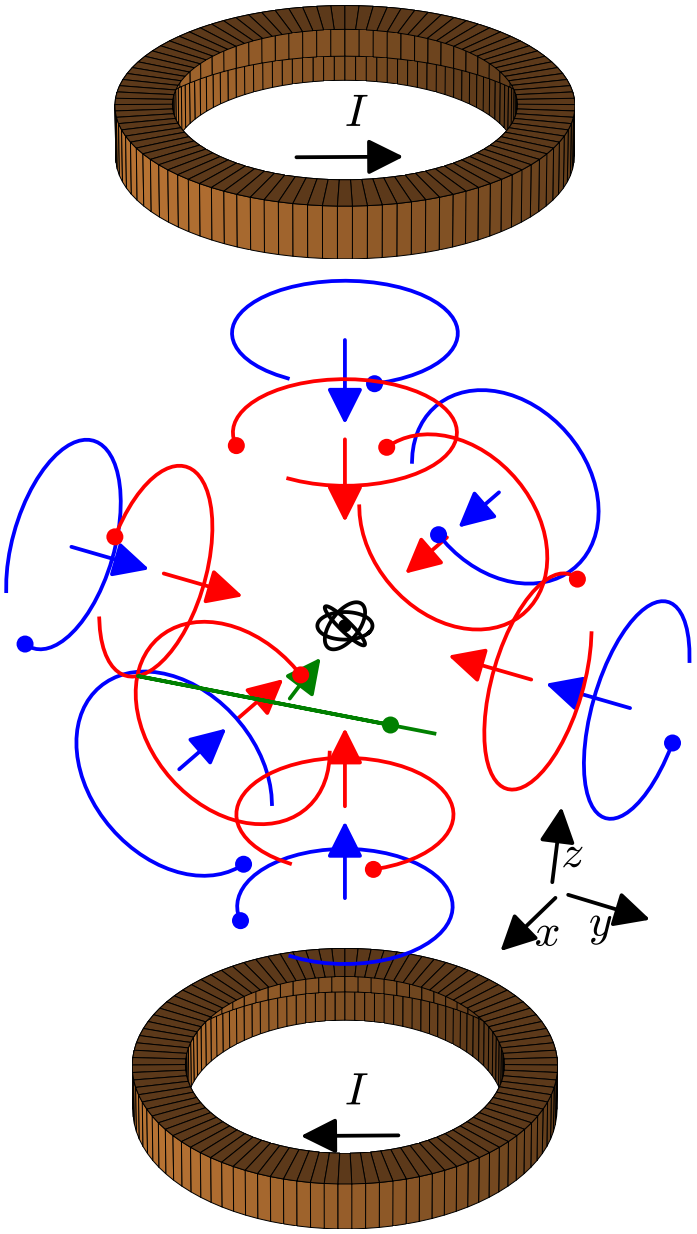

Figure 4-1: The cooling (repump) beams are shown here as blue (red) arrows along with the direction of their polarizations required for the MOT to work. These polarizations are specific to the direction of the currents indicated in the coils. The horizontally polarized probe beam is shown in green.

where the term with Ω^2 in the denominator has been neglected by assuming the intensity of the beam to be low. This is helpful in simplifying the theory, but it should be noted that this simple analysis is not valid for intensities above saturation, because the forces do not act separately. Instead, a rigorous analysis requires the calculation of the electric-dipole force from the standing wave that the two beams produce together [21].

Equation 4.1 is the equation for a particle in a viscous medium with damping α (assuming $\delta < 0$),

and for this reason the region in which the six beams intersect is known as an *optical molasses*.

The forces that optical molasses exert on an atom under typical conditions for rubidium are shown in figure 4-2. The Force that each beam exerts are shown separately, as well as their sum. The $v_c = \delta c/\omega^1$ is the *capture velocity*, that is the velocity threshold that the optical molasses are able to cool down (the force at this velocity is shown as two crosses).

Notice that we take care to speak about velocity and not speed despite the fact that atoms with $|v| < v_c$ are slowed down. In an room-temperature vapour, like those commonly used in magneto-optical traps, optical molasses cool down atoms with a Maxwell-Boltzmann velocity distribution.

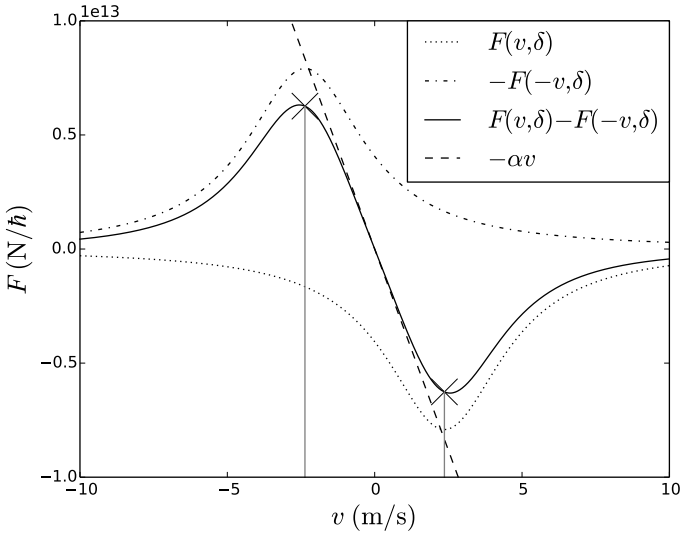

Figure 4-2: The forces exerted on an atom as functions of the velocity of the atom v. The force exerted by a beam propagating in the $-\hat{z}$ direction is shown as a dotted line, the force of a beam propagating in the $\hat{z}$ direction is shown as a dot-and-dash line, and the sum of these forces as a solid line. The linear approximation of optical molasses (see equation 4.1) is shown as a dashed line. The capture velocity is indicated in both directions with crosses. This curves correspond to $\gamma = 2\pi 6.065$ MHz, $\omega_{21} = 2\pi 384$ THz, and $\delta = -\gamma/2$, that correspond to rubidium.

The linear approximation of this force is also shown in 4-2, and it should be noted that for very slow atoms, there is also only a small force. Equation 4.1 suggests that atoms inside this linear region would reach zero velocity, but a new effect arises to prevent this for slow atoms.

4.2 Doppler Cooling Limit

Thus far we have considered only the force that radiation exerts over the atoms when photons are absorbed, however spontaneous emission must also preserve total linear momentum. While spontaneous emission is not generally isotropic, it is equally likely in opposite directions [32]. This means that over time, the kicks given to the atom by spontaneous emission cancel out.

However, absorption and emission occur at random times. Assuming a Poissonian statistic, the

average number of scattering events within time t is $\gamma\rho_{22}t$. Each of these scattering events kick the atom in a random direction giving it an additional *recoil velocity* $v_r = \hbar k/M = \hbar\omega^1/cM$. This is 5.983 mm/s for rubidium. If a photon is emitted with an angle θ respect to the z axis, it will add to the spread of the mean square velocity along the z axis by $\Delta(\bar{v_z^2})_{spont} = (\hat{z}\cdot v_r\hat{r})^2 = cos^2(\theta)v_r^2$. The average over solid angle is $\langle\Delta(\bar{v_z^2})_{spont}\rangle = \langle cos^2\theta\rangle v_r^2 = \eta v_r^2$. And since this events happen at a rate $\gamma\rho_{22}$ it follows that spontaneous emission contributes to the change of the average square velocity at a rate $\eta v_r^2\gamma\rho_{22}$. In a similar manner, the variations in time of the absorption events contribute with $v_r^2\gamma\rho_{22}$ (since all absorptions of a beam along z occur along z). On the other hand, from equation 4.1 it follows that

$$v_z F_z = v_z\frac{dP_z}{dt} = Mv_z\frac{dv_z}{dt} = \frac{d}{dt}(\frac{1}{2}Mv_z^2) = \frac{dK}{dt} = -\alpha v_z^2$$

where K is the kinetic energy and P_z is the momentum of the atom in the $\hat{z}$ direction. Taking the average over time and adding contributions from absorption and spontaneous emission for two beams counter propagating along the z axis.

$$\frac{d}{dt}(\frac{1}{2}M\bar{v_z^2}) = \frac{1}{2}M(2\eta\gamma\rho_{22}v_r^2 + 2\gamma\rho_{22}v_r^2) - \alpha\bar{v_z^2}$$

However, the counter propagating beams along the x and y axes contribute further spontaneous emissions along the z direction (but none from absorption). Therefore the η becomes 3η. In a symmetrical light field, random variations from the relative phases between the beams make the emission isotropic [21], $\eta = \frac{1}{3}$ so the equation becomes

$$\frac{d}{dt}(\frac{1}{2}M\bar{v_z^2}) = 2M\gamma\rho_{22}v_r^2 - \alpha\bar{v_z^2}. \tag{4.2}$$

This can be easily solved, and converges to $\bar{v_z^2} = \frac{2M\gamma\rho_{22}}{\alpha}v_r^2$. In other words, atoms reach a *terminal velocity* v_∞ (along the z axis)

$$v_\infty = \sqrt{\frac{2M\gamma\rho_{22}}{\alpha}}v_r \simeq \frac{\omega^1}{\omega_{21}}\sqrt{\frac{\hbar(4\delta^2+\gamma_{21}^2)}{-8M\delta}}$$

where the $\simeq$ indicates that low intensities have been assumed. According to the equipartition theorem, this average kinetic energy is related to the temperature by

$$\frac{1}{2}k_BT = \frac{1}{2}M\bar{v_z^2} = \frac{M^2\gamma\rho_{22}}{\alpha}v_r^2 \qquad \Rightarrow \qquad T = -\frac{\hbar(\omega^1)^2(4\delta^2+\gamma^2)}{16k_B\delta\omega_{21}},$$

where k_B is the Boltzmann constant, and low intensities have once again been assumed. This is a

function of δ, and it has a minimum at

$$\delta_{\text{crit}} = -\frac{\gamma}{2}, \qquad T_{\text{min}} = \frac{\hbar\gamma(\omega^1)^2}{2k_B\omega_{21}^2} \simeq \frac{\hbar\gamma}{2k_B}.$$

For rubidium, we effectively have $\gamma = 2\pi$ 6.065 MHz and the *critical detuning* is $\delta_{\text{crit}} = 2\pi 3.0325$ MHz, and the *Doppler cooling limit* limit is $T_{\text{min}} = 145.537\mu$K. For $\delta = \delta_{\text{crit}}$ the capture velocity is $v_c = 2.366$ m/s (as shown in figure 4-2) and the terminal velocity is $v_\infty = 0.118$ m/s.

4.3 Quadrupole magnetic field

The optical molasses technique is used to slow down atoms that come into the region where the six beams intersect. Atoms cooled in this way quickly reach the terminal velocity deducted in the previous section, but they eventually leave the optical molasses region. In order to trap the atoms so they do not leave the intersection of the beams, a force is needed that depends on the position of the atoms in addition to the velocity-dependant damping force. One way to achieve this is by spatially tuning the atomic resonance.

This is achieved by introducing a quadrupole magnetic field centred in the region of intersection, usually produced by a pair of coils in *anti-Helmholtz* configuration as shown in figure 4-1. The figure is slightly misleading in that the anti-Helmholtz configuration has the distance between the parallel coils equal to their radii. This ideal configuration produces the greatest gradient of the magnetic field, but it is not critical. Often greater distances are necessary because of the size of the vacuum chamber or other spacial constraints (although not as large as the figure suggests). The necessary gradient can be achieved simply by increasing the current in the coils. Typical MOTs function with approximately 15-5 G/cm [61].

Figure 4-3a shows the shape of the magnetic field lines from the quadrupole coils. The field is zero at the origin as shown by the grey lines and has increases linearly around that point. If the region in which the six beams intersect is made to coincide with this zero of magnetic field, the atoms that are slightly away from the origin will experience a Zeeman splitting δ_{M_F} of their magnetic states $|M_F\rangle$. If an atom has some displacement z along the z axis, the Zeeman splitting will be

$$\Delta E_{|FM_F\rangle} = \mu_B g_F M_F B_z.$$

where $\mu_B = \frac{e\hbar}{2m_e}$ is the Bohr magneton (see section 6.5 for a detailed calculation of the hyperfine g-factor g_F). Since the light is red-detuned this means that atoms must be slightly displaced from the origin so that the frequency-displaced energy levels allow them to absorb the cooling beam. The beam with direction $\pm\hat{z}$ is prepared with circular polarization $\sigma_\pm$ so it couples the lower states $|F, M = \pm F\rangle$ to the upper states $|F+1, M = \pm F \pm 1\rangle$ as shown in figure 4-3b.

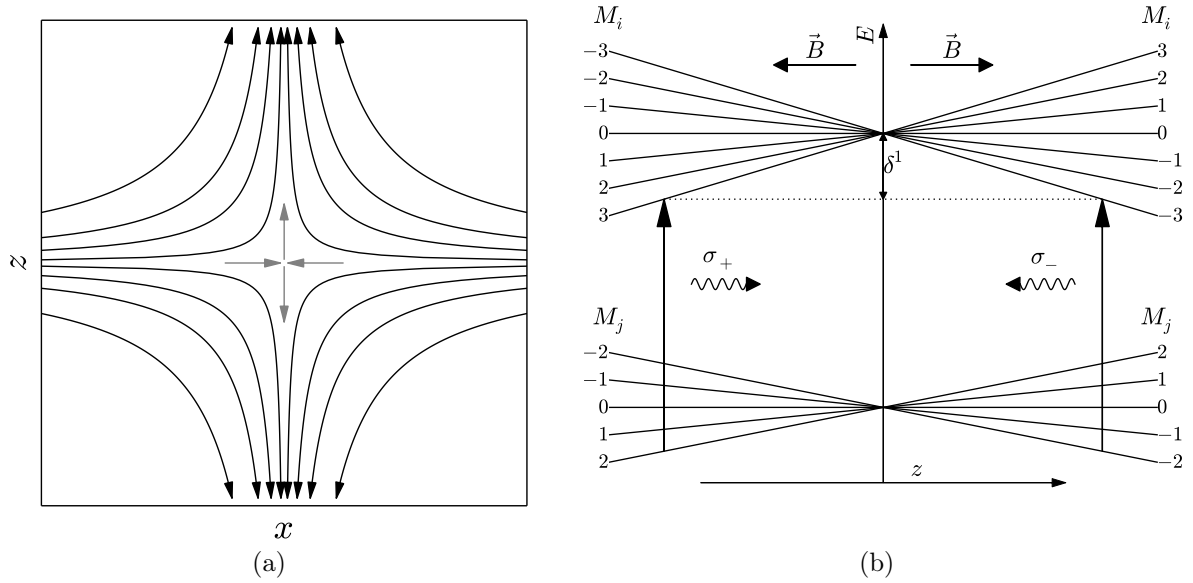

Figure 4-3: (a) The magnetic field lines produced by the anti-Helmholtz coils. (b) The position-dependant Zeeman splitting of cycling transition states for ^{87}Rb. Two counter-propagating beams of opposite circular polarizations induce a position-dependant force imbalance that pushes atoms towards the center of the trap. Notice that the energies are not to scale, since the Zeeman splittings are much smaller than the optical frequencies.

Along the $\hat{x}$ or $\hat{y}$ axes the appropriate quantization axes are $\pm\hat{x}$ and $\pm\hat{y}$ as given by the direction of the magnetic field (the field is axially symmetric) as shown in figure 4-3a. The polarization of the beams along these axes are also set so that the Zeeman effect selects the beam opposed to the displacement of the atom and the atoms are optically pumped to analogous extreme states. The appropiate polarizations are shown in figure 4-1 as well as the direction of currents that will produce the appropiate trapping magnetic field.

4.4 Repump beam

Up to this point it would seem that if the cooling beams have their frequency locked with negative detuning, atoms would be trapped in a cooling cycle between these extreme states. However, for ^{85}Rb (^{87}Rb) quantum mechanics allow a small fraction of excitations to go from $|5S_{1/2}, F = 3(2)\rangle$ to $|5P_{3/2}, F = 3(2)\rangle$. This non-resonant absorption is known as *Raman scattering*. The probability of Raman scattering decreases quickly with the detuning. The $|5S_{1/2}, F = 3(2)\rangle \rightarrow |5P_{3/2}, F = 4(3)\rangle$ and $|5S_{1/2}, F = 3(2)\rangle \rightarrow |5P_{3/2}, F = 3(2)\rangle$ transitions are separated by 120.9 MHz (266.6 MHz).

Atoms that reach the $|5P_{3/2}, F = 3(2)\rangle$ state can decay back to the $|5S_{1/2}, F = 3(2)\rangle$ but they can also decay to $|5S_{1/2}, F = 2(1)\rangle$. This *dark state* is 3035 MHz (6834 MHz) away from the upper hyperfine level of the $5S_{1/2}$ multiplet, and therefore atoms that fall there have a near zero probability of going back into the cooling cycle. In order to continue the cooling of these atoms, a *repump beam*

is introduced locked to the transition from $|5S_{1/2}, F = 2(1)\rangle$ to $|5P_{3/2}, F = 3(2)\rangle$. In this way, atoms that fall to the dark state are taken to $|5P_{3/2}, F = 3(2)\rangle$ and are given a new chance to decay to $|5S_{1/2}, F = 3(2)\rangle$, and get back to the cycling transition to be further cooled or go back to the dark state and be repumped again.

Chapter 5

Experimental setup

A scheme of the experimental setup is shown in figure 5-1. Either ^{85}Rb or ^{87}Rb is trapped and cooled in the MOT using cooling and repump lasers as shown. The cooling, repump, and reference lasers in the experiment are *extended cavity diode lasers* (ECDLs). The cooling laser is a commercial New-Focus Vortex-7000/6013 ECDL, and both the repump and reference laser were built in the Cold Atoms Laboratory of the Instituto de Ciencias Nucleares (LAF-ICN). The probe beam is produced by a commercial M-Squared SolsTis-1600-SRX-F *titanium-sapphire laser* (TiSap).

5.1 Frequency Locking

The two-photon spectroscopy is realized by keeping a constant frequency of the first-step transition, and varying the frequency of the second-step transition across the hyperfine structure of the $5D_{5/2}$ multiplet. Thus, we need to be able to lock the frequency of the lasers that will induce the first step transition.

The cooling, repump, and reference lasers frequency-locked through a *polarization spectroscopy* as described in [50]. For each laser, this spectroscopy consists of a weak probe beam counter-propagating with a strong pump beam in a room temperature rubidium vapour. The pump beam is circularly polarized and excites atoms to $\Delta M_F = 1$ transitions only (it produces optical pumping). This gives rise to a medium in which orthogonal linear polarization components of the weak and linearly polarized probe beam are absorbed differently (a birefringent medium). After propagating through this medium, the state of polarization of the probe beam is divided in orthogonal linear polarizations by a polarizing beam splitter and analysed by two different photodiodes. Thus, it is possible to simultaneously measure the absorption of both polarizations. The difference between these two signals has the shape of the derivative of a Lorentzian profile in the position of each atomic resonance that are known as *dispersion curves*.

Despite the Doppler broadening, this curves are visible to within hyperfine resolution because the

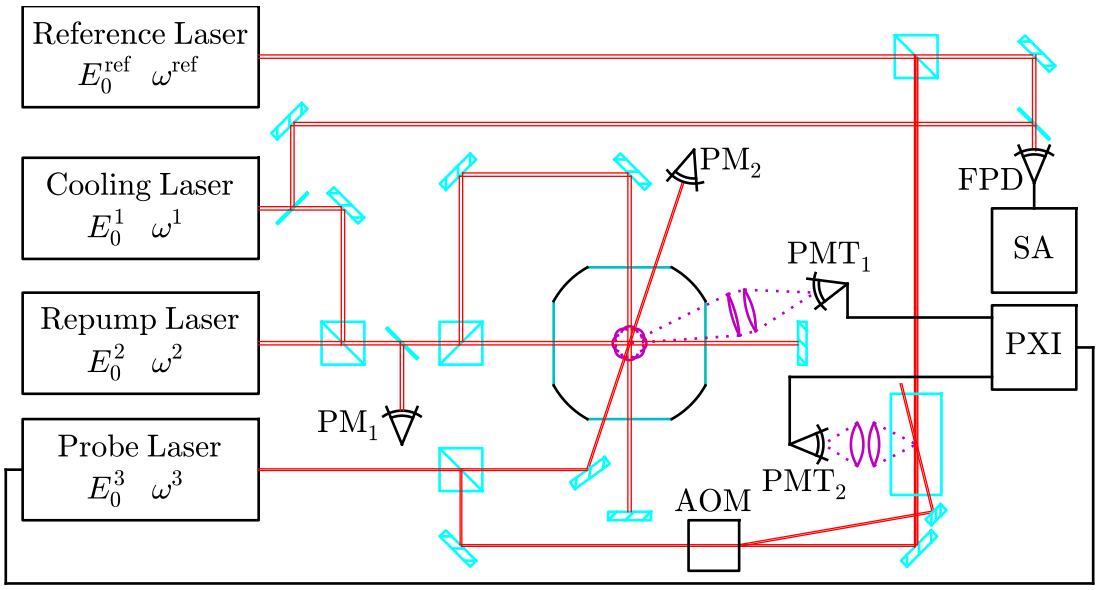

Figure 5-1: The experimental setup. The cooling laser (with amplitude E_0^1 and frequency ω^1), the repump laser (with amplitude E_0^2 and frequency ω^2), and the reference laser (with amplitude E_0^{ref} and frequency ω^{ref}) are shown here with their frequency locking spectroscopy implicit. The cooling and repump beams are mixed in a polarizing beam splitter and then split into three orthogonal counter-propagating pairs of beams with polarizations as indicated in figure 4-1. The probe beam is sent through the atomic cloud to induce the second-step excitation controlling the probe frequency ω^3 using the PXI module. The resulting spontaneous fluorescence is recorded using a photomultiplier tube (PMT$_1$). The reference and probe beams are introduced to a room-temperature cell with rubidium vapour. An acousto-optic modulator (AOM) is used to produce a second, frequency-shifted beam which is also introduced to the cell. This beams produce the calibration spectroscopy (recorded with another photomultiplier tube PMT$_2$). The cooling and reference beams are mixed and pointed at a fast photodiode (FPD) and the relative detuning $\omega^1 - \omega^{\text{ref}} = \delta^1 - \delta^{\text{ref}}$ is measured using a spectrum analyser (SA). The power of the cooling and repump beams is measured by deflecting a small portion of the power to a power-meter (PM$_1$), and the power of the probe beam is measured with another power-meter (PM$_2$).

pump laser saturates the vapour, and thus only allows the probe field to be absorbed by atoms that are precisely in resonance at zero velocity. A side effect of this velocity selectivity, is that the Doppler effect at frequencies that are at the mid-point of two atomic transitions are also velocity-selected, giving rise to a dispersion curve at each of these mid-points. These are known as *crossovers*.

The dispersion curves of the ECDLs are shown in figure 5-2. For a sufficiently strong transition or crossover, these signals exhibit a region of linear dependance on frequency, or in this case, with the electronic signal that controls the lasing frequency. This signal can be either a voltage applied to a piezoelectric that modulates the size of the extended cavity, or the current going through the laser diode.

These linear signals are used to drive a *proportional-integral-derivative controller* (PID) to establish a control loop feedback mechanism that uses the dispersion signal to correct displacements of the dispersion curve relative to a set point along the curve. In figure 5-2 the approximate position of setpoints are shown as crosses for each laser. According to the analysis in [45] the setpoints in

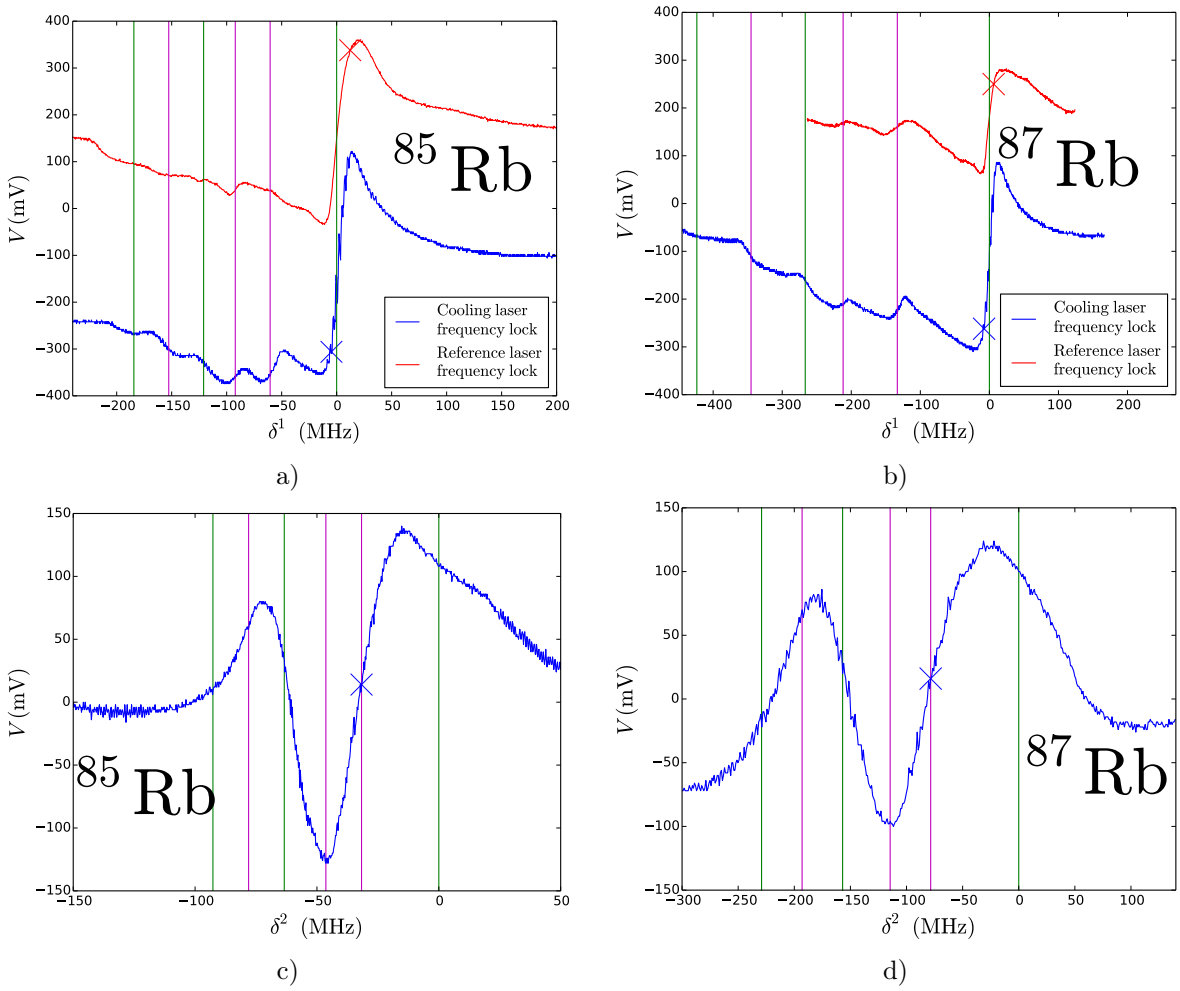

Figure 5-2: The dispersion curves used in frequency locking a) of the cooling and reference lasers for ^{85}Rb a) of the cooling and reference lasers for ^{87}Rb c) of the repump laser for ^{85}Rb d) of the repump laser for ^{87}Rb. In all spectra, the position of atomic transitions are shown as green vertical lines, and crossovers are shown as purple vertical lines. The approximate position of the frequency setpoint for the PID locks is shown in each spectrum with a cross.

a) and b) correspond to transitions $5S_{1/2}F = 3(2) \rightarrow 5P_{3/2}F' = 4(3)$ in ^{85}Rb (^{87}Rb); and setpoints in c) and d) correspond to the crossovers between transitions $5S_{1/2}F = 2(1) \rightarrow 5P_{3/2}F' = 2(1)$ and $5S_{1/2}F = 2(1) \rightarrow 5P_{3/2}F' = 3(2)$.

5.2 Capturing Fluorescence

The cooling and repump ECDLs are used to cool atoms inside a magneto-optical trap (as shown in figure 5-1). A second excitation to the $5D_{5/2}$ multiplet is induced with the TiSap. The atoms that reach the $5D_{5/2}$ multiplet spontaneously decay to the $6P_{3/2}$ multiplet emitting 5233.11 nm photons, and from there to the $6S_{1/2}, 4D_{3/2}, 4D_{5/2}, 5S_{1/2}$ multiplets. The decay to the ground multiplet produces 420.29 nm photons (which are in the visible spectrum) collected using a pair of

lenses and directed to a photomultiplier tube (PMT_1). This is an Electron Tubes-9783B, 30 mm photomultiplier tube which is powered by a Pacific Instruments model 110 high-voltage source.

However, since the atoms are inside a steel vacuum chamber, most of this spontaneous fluorescence is lost in the walls of the chamber. Only the photons that go through the windows of the chamber can be collected from the outside. The vacuum chamber poses a problem, since it is not possible for instance to place a screen inside the chamber to verify that the collecting lens is focused on the cloud. The presence of necessary optical components in the table is also cumbersome, since the collecting lens must be placed as closely to the cloud as possible to collect the largest possible amount of fluorescence.

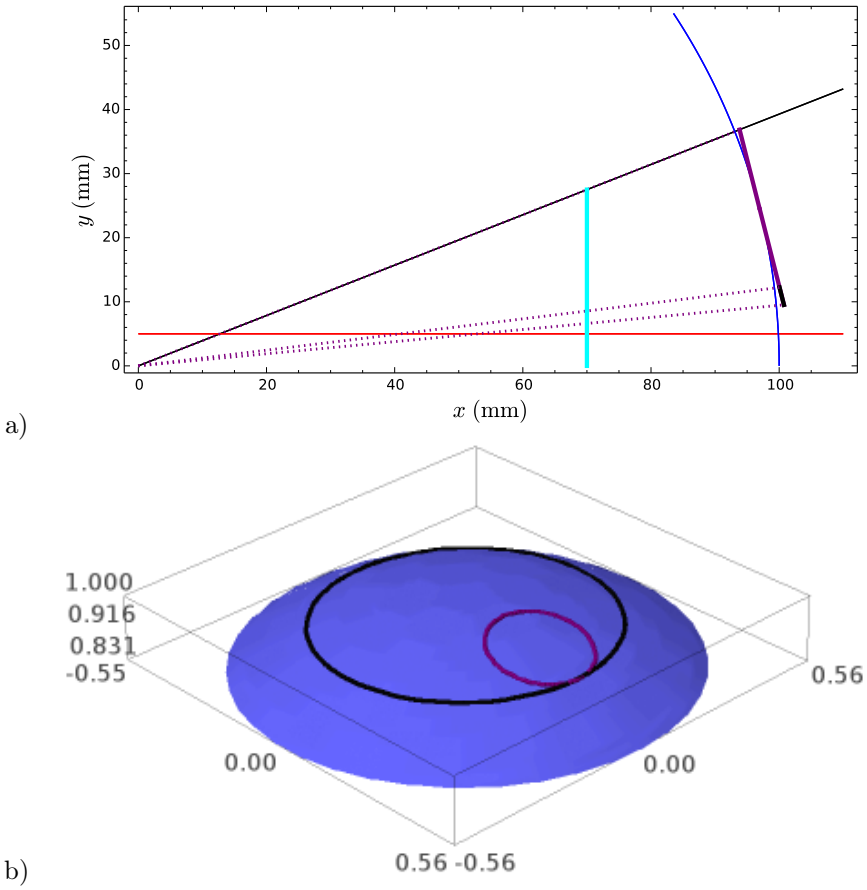

Figure 5-3: a) A view of the geometrical constraints in the $x - y$ plane. The atomic cloud (at the origin) produces spontaneous fluorescence through the vacuum chamber window (shown in pale blue). The lens (shown as a purple line) must be placed within this fluorescence cone (shown in black) orthogonal to a sphere (shown in blue) with radius equal to the focal length of the lens. This mus be done without blocking the cooling beam (shown in red). The solid angle captured by the lens is indicated with dotted purple lines. b) A 3D view of the solid angle that the lens captures. A cap of the sphere of radius equal to the focal length is shown together with the solid angle that the window lets out of te vacuum chamber (shown in black). The solid angle captured by the lens is shown in purple.

The circular windows of the chamber place the restriction that the lens must be within the cone

with vertex in the centre of the trap that is generated by the circumference of the window as sketched in figure 5-3. The radius of the window is shown as a clear blue line, and the cone as a black diagonal line. The condition for the cloud to be in focus is that the lens is placed tangent to a sphere with radius equal to the focal length (10 cm) shown as a blue circle. Another restriction is that the lens must not intersect the counter-propagating cooling beams shown in red that go through the window (otherwise there will be no trapped atoms). Furthermore, the edge of the metallic tube that holds in place the lens (shown in black) must not obstruct the cooling beams either.

A program was made to calculate the range of positions relative to the centre of the trap that satisfy these geometric conditions. Two biconcave lenses were fixed inside a metallic tube, the collecting lens with focal length 10 cm and the second with focal length 5 cm. The tube was fixed to a 3-micrometer traslation stage, that allows the position of the collecting lens to be controlled with a precision of 0.001 inches. Knowing the position of the traslation stage relative to the vacuum chamber, the solutions of the geometric problem were introduced trough the micrometers to place the lens. A set of plumbs were used to align the tube respect to the centre of the chamber, thus fulfilling all necessary conditions. The resulting solid angle is 0.398 % of a sphere.

The light collected by the first length is collimated inside the tube, and the second lens focuses it on the cathode of the photomultiplier tube. The current produced in the cathode is then directed to a current to a Keitheley-428 current-to-voltage amplifier with gain 10^5 V/A and a filter rise-time of 300 μs. The amplification was chosen to obtain the maximum signal without overloading the amplifier, and the filter rise-time to suppress the noise without distorting the signal.

5.3 Data Acquisition

The overall process of recording spectra is shown schematically in figure 5-4. Using a LabView, the following program was implemented:

1. The user specifies five parameters: the number data points N that the spectra will have, the time step between each data point dt, the amplitude A of a triangular voltage signal (from now on the *sweep signal*), an offset Off for the sweep signal, a number of spectra to average over N_{av} to produce a single final spectrum.

2. The values of $N, dt, A,$ Off are used to calculate two lists of numbers $t,$ sweep of length N that comprise the execution times of each data point and their corresponding value of sweep signal.

3. Zero-valued cache lists of numbers $\overline{\text{PMT}}_1$ and $\overline{\text{PMT}}_2$ of length $N$are created.

4. A for loop of N_{av} iterations is started.

5. The t and sweep signals are fed to a data-synchronization routine denoted R&W in figure 5-4 that for each time step sends the corresponding sweep voltage to the piezoelectric that

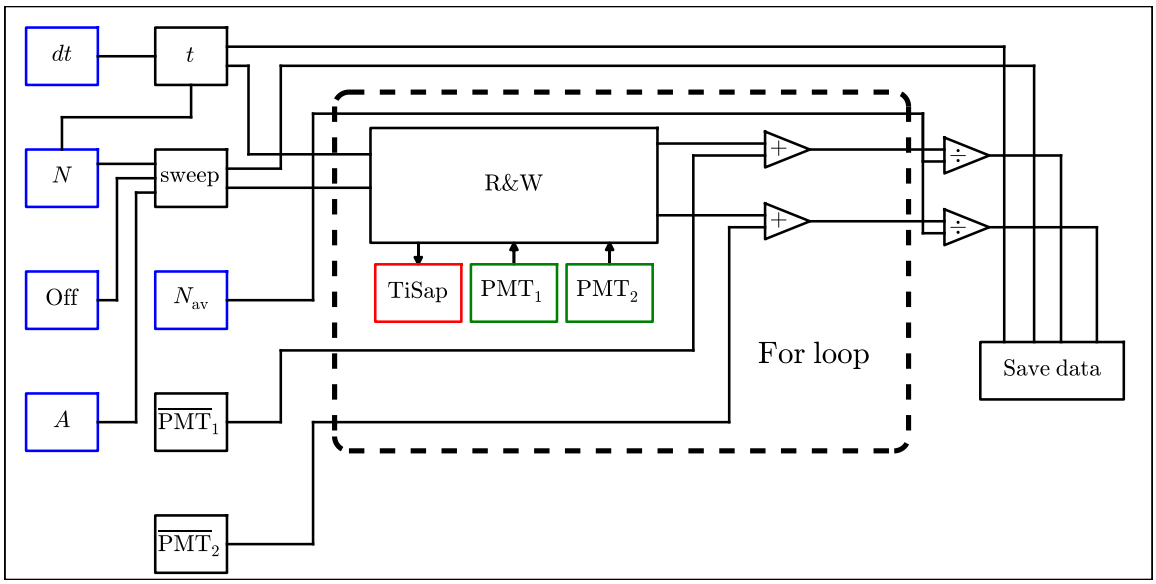

Figure 5-4: A schematic of the data acquisition system. Parameter provided by the user are shown in blue: the time-step between frequency variation steps dt, the number of steps N, the offset given to the sweep signal Off, the amplitude of the sweep signal A, and the number of spectra to average over N_{av}. These parameters are used to prepare the sweep signal and the time steps t as lists of floating-point numbers. Two cache lists $\overline{\text{PMT}}_1$, $\overline{\text{PMT}}_1$are created to store the averages. A for loop with N_{av} iterations is started, and in each iteration a read & write routine sends the sweep signal to the reference cavity of the TiSap laser, and simultaneously records the voltage from both photomultiplier tubes. The numeric values of these recorded voltages are added to the caches. When the for loop ends the numeric values in the cache are divided by N_{av} to produce the average in each entry. The results are saved to a text file containing four columns with the values of t, sweep, $\overline{\text{PMT}}_1$, $\overline{\text{PMT}}_2$ (in that order).

controls the length of the reference cavity of the TiSap (thus varying the emission frequency), and simultaneously reads the value of voltage returned by the current-to-voltage amplifier of both PMTs.

6. Once all N steps are executed, add the readings of the PMTs to $\overline{\text{PMT}}_1$ and $\overline{\text{PMT}}_2$.

7. If less than N_{av} iterations have been performed go to step 5, or else continue.

8. Divide $\overline{\text{PMT}}_1$ and $\overline{\text{PMT}}_2$ by N_{av}

9. Save t, sweep, $\overline{\text{PMT}}_1$ and $\overline{\text{PMT}}_2$ to disk.

This program is ran inside a while loop, so changing the values of $N, dt, A, \text{Off}, N_{\text{av}}$ allows the user to repeat chosen spectroscopies in real time. Measurements in this thesis were performed with $N_{\text{av}} = 100$, $N = 1000$, $dt = 1\mu$s and the other values were chosen according to what the hyperfine structure required from the sweep signal to be well visualized.

5.4 Calibration spectroscopy

The $\overline{\mathrm{PMT}}_1$ data form spectra of the voltage produced by the current-to-voltage amplifier as a function of the voltage of the sweep signal. In order to transform the sweep signal into a frequency scale an auxiliary *reference laser* is frequency locked with another PID feedback controller to the $5S_{1/2}\ F = 2(3) \rightarrow 5P_{3/2}\ F = 3(4)$ transition for ^{87}Rb (^{85}Rb). This beam is then directed to a room temperature cell with rubidium vapour. A portion of the probe beam used in the MOT is also directed to the cell (in the opposite direction). The combined beams produce the same excitation and decay scheme taking place in the MOT. The resulting 420 nm spontaneous fluorescence is recorded in a Hamamatsu H7827 photomultiplier tube (PMT_2) whose signal is recorded by the PXI in synchrony with the sweep signal.

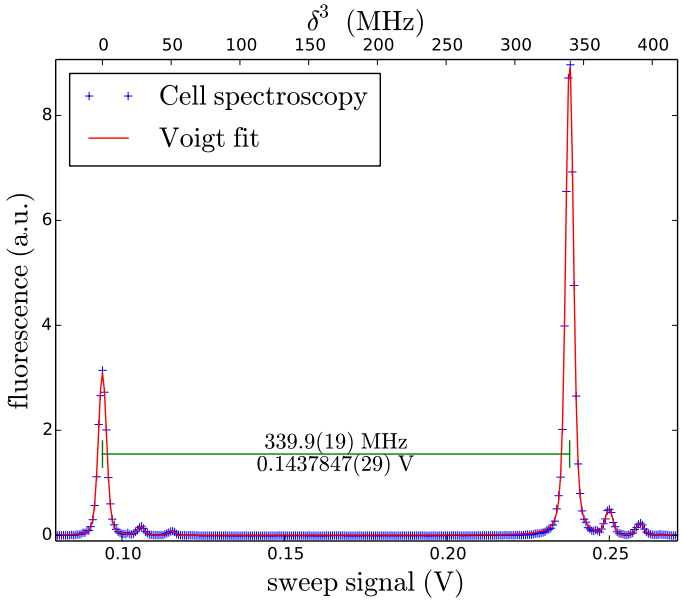

Figure 5-5: The data recorded by the photomultiplier tube in the cell spectroscopy are shown in blue. Six Voigt profiles are fitted to the peaks, as shown. The frequency difference between the highest peaks is given by the radio-frequency from the driver that controls the AOM, and the voltage difference is extracted from the Voigt fits.

The spectrum obtained in the cell is taken at low $E_0^{\mathrm{ref}}, E_0^3$, so that E_0^1 can be varied to observe the effect in the MOT spectra. The cell spectra show well defined peaks to which Voigt profiles can be fitted to find their centres. The probe beam is sent through an acousto-optic modulator (AOM), that is used to produce a frequency-displaced beam which is sent co-propagating with the original beam. The frequency difference between the modulated beam and the original is given by a radio-frequency driver. In this way, if the sweep signal is of sufficient amplitude the three peaks of the $5D_{5/2}$ multiplet are visible at two different voltage values. The relationship between voltage and frequency is known to be very linear in this voltage interval because the voltage differences between the other two pairs

of peaks are $0.143784V \pm 2.9 \times 10^{-6}V$, $0.14405V \pm 5.3 \times 10^{-5}V$, $0.1441V \pm 1.1 \times 10^{-4}V$. The ratio of the frequency and voltage differences between the two highest peaks 2363 ± 13 MHz/V is used to transform the voltage scale into an absolute frequency scale as shown in figure 5-5. The frequency difference between the $5P_{3/2}F = 3 \rightarrow 5D_{5/2}F = 4, 2$ peaks is 51.77 MHz in ^{87}Rb, the error of measuring this frequency difference using this calibration is 297 kHz.

5.5 Relative detuning

The cooling laser can be locked to different frequencies in a range of about 8 MHz (while still having enough detuning to cool and trap atoms) using different setpoints along the dispersion curve with the PID controller [61]. However, this does not give information about the *exact* detuning from the transition of interest. In order to get this information, the reference beam is mixed with that of the cooling laser, which is locked at the same transition (with a certain redshift). The mixed beam is pointed to a fast photodiode (FPD) whose voltage signal is fed to a spectrum analyser (SA) that returns the frequency spectrum of this *beat* signal shown in figure 5-6. Since the reference laser and the cooling laser are locked at different frequencies, this spectrum shows a peak at the frequency difference $\omega^1 - \omega^{\text{ref}} = \delta^1 - \delta^{\text{ref}}$. Assuming that the reference laser has a constant frequency this measurement allows the δ^1 detuning to be varied in a controlled manner.

The approximate setpoints of the frequency locks are shown in 5-2. The setpoints of the cooling and reference lasers were taken as apart as possible in order to obtain a frequency difference as large as possible. At small differences, the peak becomes mixed with the zero-frequency peak in the Fourier transform.

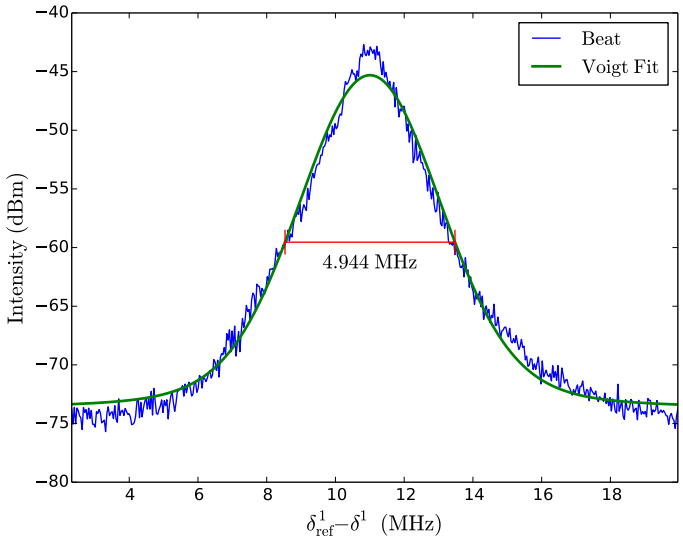

Figure 5-6: Beat of the reference and cooling lasers.

Since a beat of the two lasers was recorded only for each data series (but not for each recorded spectrum), and the value of $\delta^{ref} - \delta^1$ was taken by examining the frequency spectrum of the beat singal directly at the spectrum analyser screen, the error of the relative detuning measurement is taken as the half width at half maximum (HWHM) of the beat signal shown in figure 5-6 (2.47 MHz).

This beat allows the spectral width of the lasers to be estimated by taking them to be approximately of the same width. This is reasonable given that they are all ECDLs of similar architecture and diodes. Hence $\text{FWHM}_1 = \text{FWHM}_2 = (4.94 \pm 0.14 \text{ MHz})/\sqrt{2} = 3.4 \pm 0.1$ MHz.

5.6 Electric field measurement

The power of the cooling and repump beams is measured using a power-meter (PM) that receives a faint beam reflected on a beam splitter. The power of the probe beam is measured by another power-meter placed at the other side of the atomic cloud. The power of of these beams is varied using a half-wave plate to rotate their initially linear polarizations and using a polarizing beamsplitter to select horizontal polarization.

The combined cooling and repump beams go through quarter-wave plates with a diameter of 1/2' to produce the polarization that the MOT requires. These plates obstruct most of the laser light of the previously expanded Gaussian beam. The diameter of the power-meter is smaller than these beams (9 $\pm$0.02 mm). The error of the power measurement is taken as the variation of the reading of power which is about 5 in the third digit of the reading. This corresponds to 0.5 % of the power measurements. The widths of these beams are previously increased through a pair of lenses, this means that only the central part of the originally Gaussian beam is present in the MOT. Since the spatial variation of the intensity is not taken into account, and it is relatively homogeneous, it is appropiate to dismiss this variations and calculate the amplitude of the electric field treating the beam as having a top-hat intensity distribution. Hence the electric field amplitude is calculated through B.1. The corresponding error is propagated from the measurements of the power and the diameter of the detector. The light that is not contained in the detector has no effect in the value of the electric field as long as the variations of intensity are ignored.

The probe beam is introduced without any obstruction to the atomic cloud, so that electric field amplitude must be calculated through B.2. In order to measure the width of this beam a photograph (shown in figure 5-7a) was taken. The beam is directed to a perpendicular sheet of millimetric paper. A photograph of the millimetric paper 5-7b allows a pixel-to-millimeter correspondance to be calculated. A 2D Gaussian distribution of the form

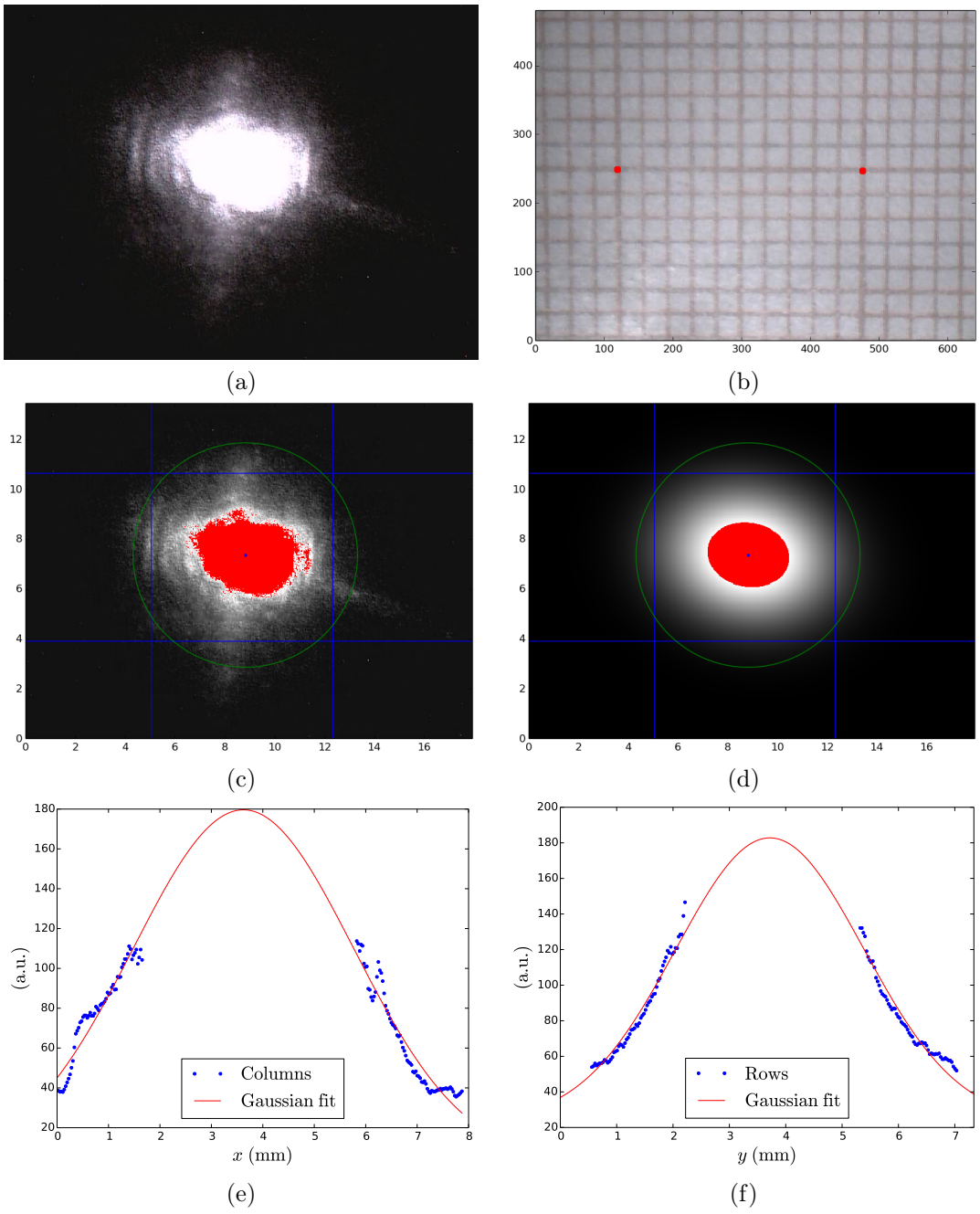

Figure 5-7: The steps in the determination of the size of the probe beam. a) The photograph of the beam. b) The photograph of the millimetric paper indicting two pixels separated by 10 mm. c) The photograph with the saturated pixels indicated in red, and the pixels to be fitted delimitated by blue lines. The detector is shown as a green circle for comparison.d) The resulting fit. e) The summed columns. f) The summed rows.

$$A\exp(-\frac{((x\cos(\theta)+y\sin(\theta))-(\sigma_x\cos(\theta)+\sigma_y\sin(\theta)))^2}{2\sigma_x^2}-\frac{((x\sin(\theta)-y\cos(\theta))-(\sigma_x\sin(\theta)-\sigma_y\cos(\theta)))^2}{2\sigma_y^2})$$

is fitted to the values of each pixel in the photograph, with pixels with a value above certain threshold not being considered as shown in red in 5-7c. This allows the tilt θ of the beam in the photograph to be accounted for. The corresponding Gaussian distribution is shown in 5-7d. The fit returns $\sigma_x = 2.14 \pm 0.10$ mm and $\sigma_y = 1.67 \pm 0.10$ mm as the standard deviations in rotated axis.

The picture is then rotated by the angle θ about the blue point indicted in figure 5-7c, and the pixel values of columns and rows are added to produce the profiles shown in figures 5-7e and 5-7f respectively. A Gaussian fit with the same σ_x and σ_y is shown.

Chapter 6

Numerical Simulation

The purpose of developing the theory in chapters 2 and 3 is to solve optical Bloch equations that simulate the spectroscopy described in chapter 4. A Python 2.7 program was written that receives as input the quantities calculated in chapter 3 (namely a set of states $|i\rangle$, resonant frequencies ω_{ij}, matrix elements of the dipole operator r_{pij}, and decay frequencies γ_{ij}). From these quantities it uses equations 2.10 and 2.9 to produce Fortran 90 code to calculate explicitly each non-zero element $A_{\mu\nu}$ of the evolution operator and the independent vector b^{ν}.

The Fortran expressions for each $A_{\mu\nu}$ and b^{ν} are explicitly in terms of arbitrary E_0^l and δ^l. The code is next compiled using the gfortran compiler from the GNU Compiler Collection [19]. The resulting binary file is then called using a Python interface through which values of E_0^l and δ^l are specified. With these user-given parameters, the Fortran program then solves the equations for the steady state using LAPACK (Linear Algebra Package) [2]. To calculate spectra the user selects a δ^l to be swept (δ^3 in our case), a variation range and a number of points to be solved.

The solutions of these systems of equations are complete ρ^{ν} for each point of interest. When all of these have been calculated for a spectrum, the Fortran program saves the results to a NetCDF (Network Common Data Form) binary file [55], [10]. This file is then read by a Python interface and the density matrices can then be used to calculate the spontaneous fluorescence using equation 3.5. The NetCDF protocol for binary encryption was chosen to make the fastest and most memory-efficient communication between the Python and Fortran sides of this process. Using text files is approximately 23 times slower, and can take even more time than it takes LAPACK to solve the equations.

These spectra are then convolved with a Gaussian distribution to account for all broadening effects (except power broadening, which is contained in the solutions to Bloch equations), including the laser emission widths and the Doppler effect as explained in section 3.4. The convolution is calculated in Python using the NumPy library [69]. This library implements the convolution

through a fast Fourier transform, and the time this takes is negligible compared to the solution of the equations.

Since all this process, from producing the code of the equations to their solution, interfacing and calculating the fluorescence spectra are done in a highly efficient way, I have creatively named this software package "FAST Atomic Spectroscopy from Theory" (FAST).

6.1 Approximations to the complete problem

This name can be misleading, however. The complete problem includes all states from all the multiplets shown in figures 3-1 and 3-2. For ^{85}Rb (^{87}Rb) this means solving optical Bloch equations that have $N_e = 180$ (120) states, leading to $N_\rho = 32399$ (14399) equations. FAST can solve this problems, and is characterized using processor cores Intel® Xeon® E5-2690 v3 at 2.60GHz clock frequency and RAM memories of 2GB. The characterization is shown in table 6.1. However, calculating theoretical spectra involves finding a solution to the equations for approximately 500 experimental data points from an experimental spectrum. Each of these points takes approximately 5030 s (445 s).

The aim of this thesis is not just to reproduce the measured spectra using experimental parameters, but to fit theoretical spectra to the experimental data in order to provide insight of the details of the physical processes occurring during the spectroscopy across a range of parameters. This fitting would take months to years using the complete problems so some compromise must be made between physical accuracy and time of computation.

One obvious shortcut is using solutions to a reduced number of states to calculate the fluorescence spectra. For instance, one could exclude multiplets $4D_{3/2}$ and $4D_{5/2}$ from the calculation. These states recieve less than 6 % of the 0.6673 MHz of spontaneous decay from $5D_{5/2}$. Ignoring their role would still produce in principle reasonably realistic results. From this reduced problem we could still use 3.5 to calculate the spontaneous fluorescence. While the values calculated in this way might correlate well with those of the complete problem, the populations in $6P_{3/2}$ will be higher because of the absence of other relevant states. This will lead to higher-than-real values of fluorescence.

		^{85}Rb				^{87}Rb			
States	Comp	N_e	t_w	t_c	t_r	N_e	t_w	t_c	t_r
$5S_{1/2}$ $5P_{3/2}$ $5D_{5/2}$	74 %	72	22.0	32.8	21.5	48	7.88	10.0	2.01
$5S_{1/2}$ $5P_{3/2}$ $6P_{3/2}$ $5D_{5/2}$	80 %	96	40.4	56.3	122	64	13.5	16.4	10.6
$5S_{1/2}$ $5P_{1/2}$ $5P_{3/2}$ $4D_{5/2}$ $4D_{3/2}$ $6S_{1/2}$ $6P_{3/2}$ $5D_{5/2}$	100 %	180	163	4615	5030	120	50.6	64.9	445

Table 6.1: For both simplified and complete problems, and for each isotope the number of states in N_e, the number of equations N_ρ, the time required to write the Fortran code t_w, to compile it t_c, and to run it for one point of a spectrum t_r are shown in seconds. The *completeness* of each problems is defined as the fraction of the 0.6673 MHz of spontaneous decay from $5D_{5/2}$ that is taken into account.

The most extreme version of this simplification scheme is to solve only for the $5S_{1/2}, 5P_{3/2}, 5D_{5/2}$ multiplets. In this case formula 3.5 cannot be applied, since there is no $6P_{3/2}$ multiplet to sum over. However, since it can only come from spontaneous decay, the population in $6P_{3/2}$ can intuitively be thought of as being proportional to that in $5D_{5/2}$. The sum of the populations in $5D_{5/2}$ is taken as a measure of fluorescence and compared to the fluorescence calculated from the complete problem as shown in figure 6-1.

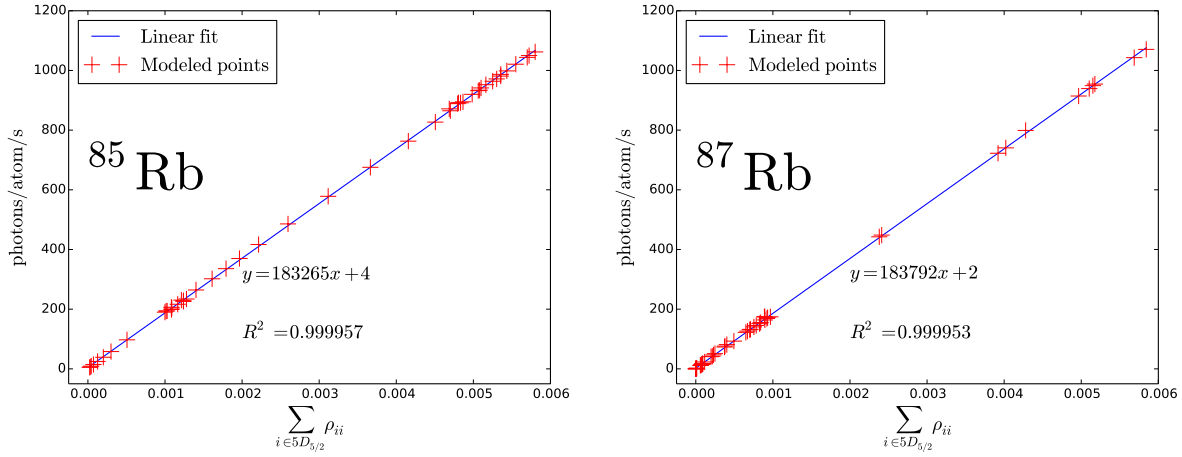

Figure 6-1: The fluorescence calculated through formula 3.5 using all of the states in figures 3-1 and 3-2 is shown in the vertical axis. The horizontal axis shows the sum of the populations in the $5D_{5/2}$ multiplet calculated using only the states in the $5S_{1/2}, 5P_{3/2}, 5D_{5/2}$ multiplets.

A very strong correlation coefficient $R^2 = 0.999957$ ($R^2 = 0.999953$) is found between fluorescence and this sum of populations for ^{85}Rb (^{87}Rb). This linear relation can then be used to calculate the fluorescence while solving only for the reduced problem. 8-core processors with the characteristics mentioned above are used to calculate solutions in parallel computation, allowing the calculation of fluorescence spectra in about 16 min (2 min).

6.2 Fitting to the experiment

In order to reproduce the measured spectra the experimental parameters E_0^l and δ^l have been obtained in chapter 4. However, we are still missing the value of δ^1_{ref} that is used to calculate variations of δ^1. The emission linewidth of the lasers is also unaccounted experimentally, as is the temperature of the atomic cloud. In order to get an estimation of these parameters the model will be used to fit theoretical spectra to the experimental data.

A fitting process could in principle be performed for any experimental parameters that may be of interest, that are unknown or that are relatively uncertain. In this thesis the reference detuning δ^1_{ref} and the effective broadening standard deviation σ_{eff} will be fitted to the experimental spectra. We measure spectra varying the power of the cooling beams (directly related to E_0^1) and the cooling

detuning δ^1. We will also fit this parameters in order to compare how their measured values (and errors) might differ from those obtained by fitting the model to the data.

For a given experimental spectrum with N data points we calculate a theoretical spectrum from some values of the fitting parameters $(\sigma_{\text{eff}}, E_0^1, \delta_{\text{ref}}^1, \delta^1)$. The highest point of this experimental spectrum is used to rescale the experimental data, and calculate the reduced chi squared

$$\chi^2_{\text{red}} = \frac{1}{N-4-1}\sum_j^N (\phi(\delta_j^3; \sigma_{\text{eff}}, E_0^1, \delta_{\text{ref}}^1, \delta^1) - y_j)^2$$

where ϕ is the fluorescence calculated from the model (equation 3.5) and y_j is the rescaled experimental data point corresponding to δ_j^3. This objective function is minimized over parameter space using the Nelder-Mead polygon method as implemented in the SciPy library for Python [34]. When this converges to a minimum in parameter space we obtain a theoretical estimation of the experimental parameters that are being fitted.

6.3 Goodness of fit error estimation

Some measure of the error of this estimation is needed. The most strict procedure would be to take into account the experimental errors of all measurements that are done to feed the numerical values that the model uses. This includes the measurement of atomic energy levels, half-lives, laser powers, detunings, polarizations and imperfections in the geometry of the MOT setup. This errors must then be propagated through all the calculation process including the solution of the Bloch equations. This approach is completely impractical, so a heuristic alternative will be used instead.

If all measurements $\vec{X}$ are treated as Gaussian random variables, it can be demonstrated [53] that $\chi^2_{\text{red}}(\vec{X})$ is also a random variable whose probability distribution gives rise to a covariance matrix among the parameters $\vec{X}$ given by

$$\mathbf{COV} = (\mathbf{H})^{-1}\chi^2_{\text{red}} = \begin{bmatrix} \frac{\partial^2\chi^2_{\text{red}}}{\partial X_1^2} & \frac{\partial^2\chi^2_{\text{red}}}{\partial X_1\,\partial X_2} & \cdots & \frac{\partial^2\chi^2_{\text{red}}}{\partial X_1\,\partial X_n} \\ \frac{\partial^2\chi^2_{\text{red}}}{\partial X_2\,\partial X_1} & \frac{\partial^2\chi^2_{\text{red}}}{\partial X_2^2} & \cdots & \frac{\partial^2\chi^2_{\text{red}}}{\partial X_2\,\partial X_n} \\ \vdots & \vdots & \ddots & \vdots \\ \frac{\partial^2\chi^2_{\text{red}}}{\partial X_n\,\partial X_1} & \frac{\partial^2\chi^2_{\text{red}}}{\partial X_n\,\partial X_2} & \cdots & \frac{\partial^2\chi^2_{\text{red}}}{\partial X_n^2} \end{bmatrix}^{-1} \chi^2_{\text{red}},$$

where $\mathbf{H}$ is the Hessian matrix in parameter space at the convergence point. In our case we calculate it only for the four fitting parameters for which χ^2_{red} is readily available, and not for all the measurements mentioned before. The derivatives in this matrix are calculated numerically using second order centred finite difference approximations [9]. The diagonal elements of this matrix are

variances for each parameter, and their square roots are taken as their theoretical errors.

6.4 Spatial dependance of the density matrix

It is also important to note that this numerical simulation is done considering only the atoms that are precisely at the centre of the MOT. In reality, the atomic cloud has a diameter of approximately 1 mm, and atoms in different positions contribute differently to the fluorescence captured by the PMT.

Firstly, the magnetic field $\vec{B}(\vec{R})$ of the MOT establishes a preferential quantization axis for the density matrix along the direction of the magnetic field $\hat{b}(\vec{R}) = \vec{B}(\vec{R})/|\vec{B}(\vec{R})|$. In each point, equations in chapter 2 must be solved rotating the light fields so they are oriented correctly with respect to the preferential axis. This $\hat{\rho}(\vec{R})$ solutions must then be added to produce an effective density matrix

$$\hat{\rho}_{\text{eff}} = \frac{\int_{V_{\text{cloud}}} [\hat{U}(\vec{R})\hat{\rho}(\vec{R})\hat{U}^{\dagger}(\vec{R})]\varrho(\vec{R})dV}{\int_{V_{\text{cloud}}} \varrho(\vec{R})dV},$$

where $\varrho(\vec{R})$ is the density of the atomic cloud. Notice that $\hat{\rho}(\vec{R})$ are not simply added together, but rather they must be transformed by a rotation matrix $\hat{U}(\vec{R})$ that takes it from the basis of $\hat{\vec{F}} \cdot \hat{b}(\vec{R})$ eigenvectors to the basis of $\hat{\vec{F}} \cdot \hat{z}$ eigenvectors (see [7], [17]).

Secondly, the fields have been taken as plane waves throughout this thesis, however, if we consider their Gaussian structure $\vec{E}^{l}(\vec{R})$ the calculation becomes

$$\hat{\rho}_{\text{eff}} = \frac{\int_{V_{\text{cloud}}} [\hat{U}(\vec{R})\hat{\rho}(\vec{R}, \vec{E}^{l}(\vec{R}))\hat{U}^{\dagger}(\vec{R})]\varrho(\vec{R})dV}{\int_{V_{\text{cloud}}} \varrho(\vec{R})dV}.$$

Also, the presence of a magnetic field produces a Zeeman shift in every point of the cloud (except in the center), thus

$$\hat{\rho}_{\text{eff}} = \frac{\int_{V_{\text{cloud}}} [\hat{U}(\vec{R})\hat{\rho}(\vec{R}, \vec{E}^{l}(\vec{R}), \vec{B}(\vec{R}))\hat{U}^{\dagger}(\vec{R})]\varrho(\vec{R})dV}{\int_{V_{\text{cloud}}} \varrho(\vec{R})dV}.$$

Furthermore, the position of the lens that collects the fluorescence makes atoms that are more or less in focus contribute more or less to the registered signal, and there may also be defects in the alignment of the beams and the magnetic field.

These integrals cannot be calculated except at great computational cost (and there is no mathematical trick available as in section 3.4). Hence all of these spatial details have been neglected in this thesis, and $\hat{\rho}$ has been calculated only at the center of the MOT using $\hat{z}$ as the quantization axis and without any Zeeman shift.

6.5 Zeeman Shift

It is still important to know what might be an upper bound of the effects of the Zeeman shift in the calculation. If this shift is relatively small compared to the hyperfine structure, then the interaction Hamiltonian between the static field $\vec{B}(\vec{R}) = B_z\hat{z}$ is [36]

$$\hat{H}_B = \frac{\mu_B}{\hbar} g_F B_z \hat{F}_z,$$

where $\hat{F}_z$ is the total angular momentum operator in the $\hat{z}$ direction, μ_B is the Bohr magneton, and g_F is the hyperfine Landé g-factor, given by

$$g_F = g_J \frac{F(F+1) - I(I+1) + J(J+1)}{2F(F+1)} + g_I \frac{F(F+1) + I(I+1) - J(J+1)}{2F(F+1)},$$

where g_J is the Landé factor

$$g_J = g_L \frac{J(J+1) - S(S+1) + L(L+1)}{2J(J+1)} + g_S \frac{J(J+1) + S(S+1) - L(L+1)}{2J(J+1)}.$$

The quantity g_L is the electron orbital g-factor, given by $g_L = 1 - m_e/m_n = 0.99999354$ [6]. The electron spin g-factor g_S has been measured to great precision as $g_S = 2.00231930436182(52)$ (2014 CODATA recommended value). The nuclear spin g-factor $g_I = -0.00029364000(60)$ for ^{85}Rb and $g_I = -0.0009951414(10)$ for ^{87}Rb [3]. The energy levels split according to

$$\Delta E_{|FM_F\rangle} = \mu_B g_F M_F B_z.$$

The splitting in this weak-field regime is known as the *Zeeman splitting*, and the corresponding differences between energy levels are known as *Zeeman shifts*.

According to the characterization [61] the atomic cloud is approximately 1 mm in diameter, and the magnetic field gradient $\partial_z B_z = 7.5$ G/cm $= 0.075$ T/m. This means that at the border of the atomic cloud (where the magnetic field is most intense), the field is approximately 3.75×10^{-5} T $=$ 0.375 G.

		$\Delta E_{\lvert F_i M_{F_i}\rangle} - \Delta E_{\lvert F_j M_{F_j}\rangle}$ (MHz)	
$\lvert i\rangle$	$\lvert j\rangle$	^{85}Rb	^{87}Rb
$5P_{3/2}$ $F = 4(3)$ $M_F = F$	$5S_{1/2}$ $F = 3(2)$ $M_F = F$	0.52	0.52
$5D_{5/2}$ $F = 5(4)$ $M_F = F$	$5P_{3/2}$ $F = 4(3)$ $M_F = F$	0.52	0.52
$5D_{5/2}$ $F = 4(3)$ $M_F = F$	$5P_{3/2}$ $F = 4(3)$ $M_F = F$	0.20	0.28
$5D_{5/2}$ $F = 3(2)$ $M_F = F$	$5P_{3/2}$ $F = 4(3)$ $M_F = F$	-0.10	0.10

Table 6.2: The Zeeman shifts for the main transitions of interest for both isotopes.

The main transitions of our interest, for ^{85}Rb (^{87}Rb), are the cyclic transition $5S_{1/2}F = 3(2) \rightarrow$

$5P_{3/2}F = 4(3)$, and the three allowed transitions to the $5D$ multiplet $5P_{3/2}F = 4(3) \rightarrow 5D_{5/2}F = 5, 4, 5(4, 3, 2)$. Table 6.2 shows the Zeeman shift of each of these lines for both isotopes. For the cyclic transition, the shift is about 10 times smaller than the linewidth of 6.065 MHz, and three orders of magnitude smaller than the 120 MHz (266 MHz) of the distance between hyperfine levels. For the second-step transitions, the shifts are one order of magnitude smaller than the 9.3 MHz and 8.9 MHz between hyperfine levels of ^{85}Rb, and two orders of magnitude smaller than the 28.8 MHz and 22.9 MHz between hyperfine levels of ^{87}Rb.

These are the greatest shifts within the cloud, corresponding to the borders, and hence to the least-dense regions. This means that the error in the position of peaks due to neglecting the spatial dependance of the magnetic field is about 0.5 MHz. However, since the contribution of atoms to the effective density matrix is weighed by the density at each point of the cloud, this is an upper bound.

Chapter 7

Results

I now present the results for both isotopes. Fluorescence spectra from the experiment described in chapter 5 obtained varying the electric field amplitude E_0^1 are examined. The power of the cooling beam is varied so as to take constant-size steps of E_0^1. Secondly, the detuning of the first excitation is varied taking constant steps of the relative detuning $\delta^1 - \delta^1_{\text{ref}}$.

For each of these variations and for both isotopes the following analysis is presented. The voltage-to-frequency calibration is obtained from the AOM as described in chapter 5. A few representative spectra are shown to illustrate their general behaviour. Voigt distributions are fitted to the data and the variation on the position, relative heights, and widths of the peaks is examined. The tendencies are compared with the simplified three level theory developed in subsection 2.5.1.

Next, the multilevel model is compared with the data using the quantities calculated in chapter 3 for the rubidium atom. The tendencies of the fitted parameters are presented in this chapter as functions of experimental parameters.

Lastly, the results of the simplified and multilevel models are compared.

7.1 Power Variation of the First-step Beam

7.1.1 Simple Model

Figures 7-1 (7-2) show representative spectra for a range of values of E_0^1 for ^{85}Rb (^{87}Rb). The spectra obtained in the cell using the reference laser are also shown together with the Voigt fits used to obtain the frequency calibration. The residues of these fits are shown below each spectra and although for a few points of the cell fit they are as high as 15 % of the height of the spectra, typically they are below 2 % for both the cell and MOT fits.

The transitions $5P_{3/2}F = 4(3) \rightarrow 5D_{5/2}F = 5, 4, 3(4, 3, 2)$ as given by the literature cited in chapter 3 are indicated with black lines for the cell spectroscopies. The calibration is obtained

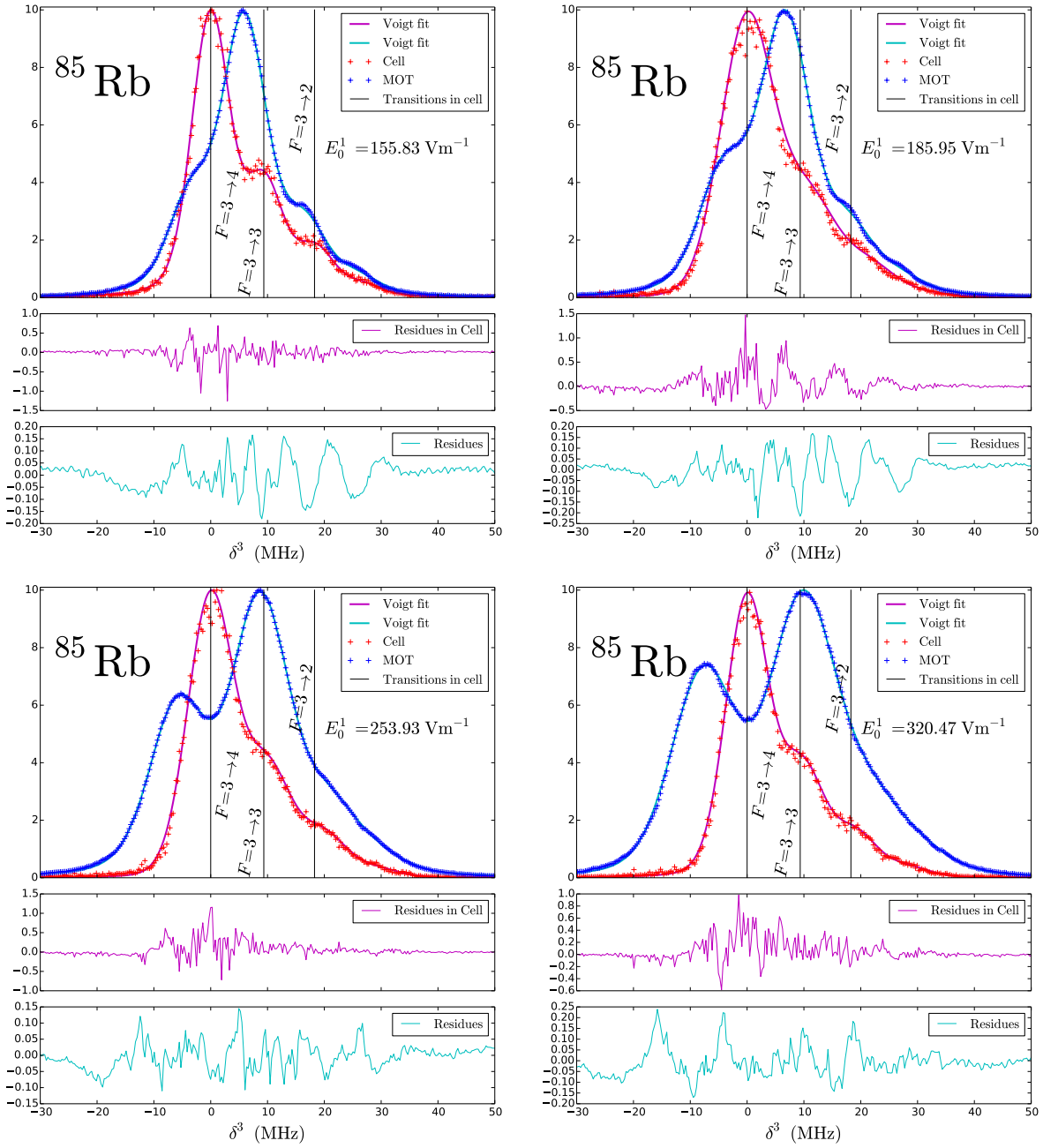

Figure 7-1: Spectra for different values of E_0^1 in ^{85}Rb. Hyperfine transitions of $5P_{3/2} \rightarrow 5D_{5/2}$ are indicated for the cell spectroscopy. The residues of Voigt fits for both spectroscopies are shown.

through the voltage-to-frequency correspondance described in section 5.4. The first peak is set to zero frequency, but the correspondance of the second and third peaks to the frequencies stated in the literature serves as confirmation of them.

The spectra in MOT show Autler-Townes splitting even at the lowest intensities. In particular, the first peak is split into the transitions $|\pm\rangle \rightarrow 5D_{5/2}F = 5(4)$ which are clearly visible for both isotopes. At high power the Autler-Townes pairs corresponding to each of the hyperfine transitions

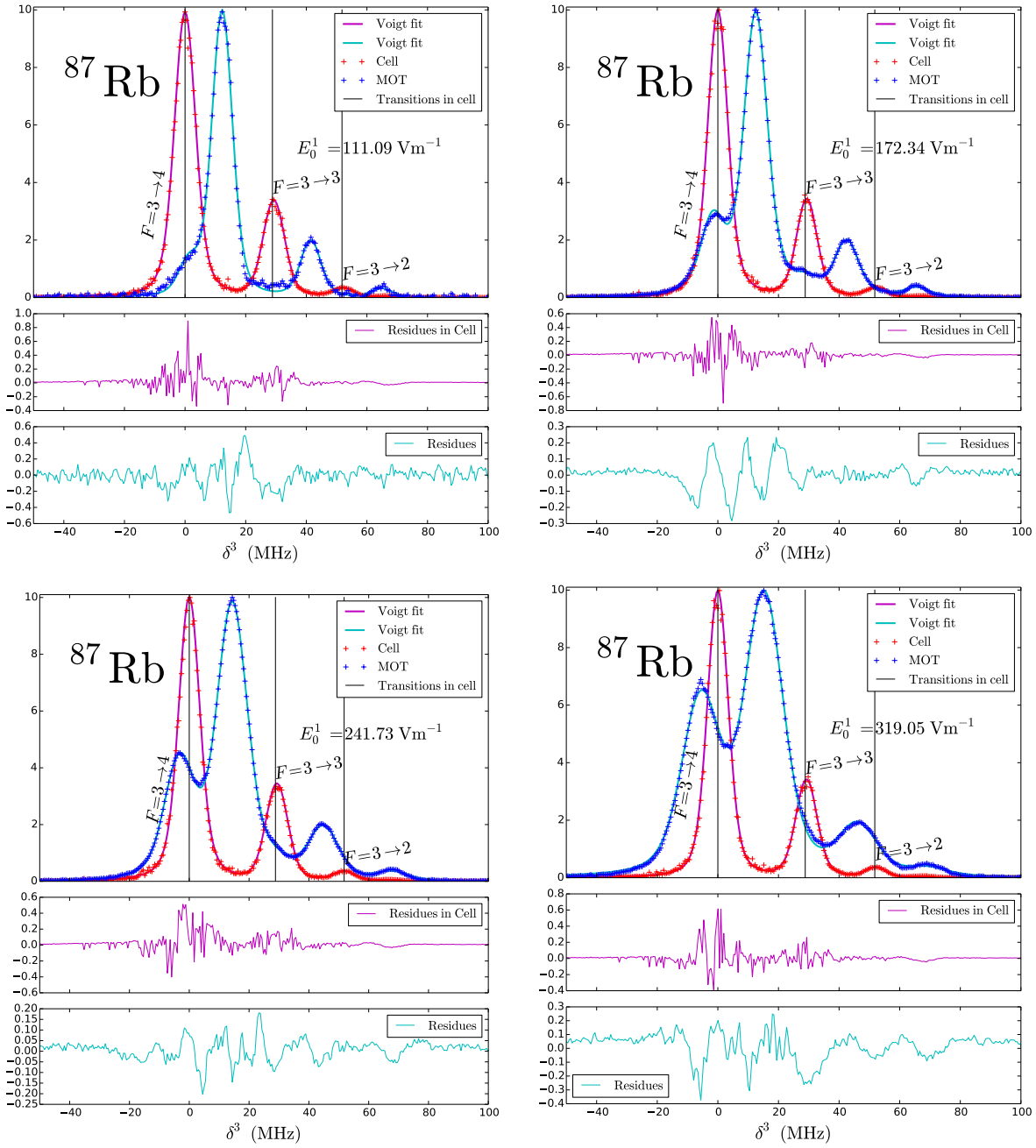

Figure 7-2: Spectra for different values of E_0^1 in ^{87}Rb. Hyperfine transitions of $5P_{3/2} \rightarrow 5D_{5/2}$ are indicated for the cell spectroscopy. The residues of Voigt fits for both spectroscopies are shown.

become so separate that different pairs overlap, and the peaks are difficult to distinguish.

Varying the intensity of the cooling beam produces changes in the fluorescence of each of the trapped atoms as driven by E_0^1 through the theory developed in chapter 2. However, this beam also plays a role in determining the number of trapped atoms. Therefore, without a reliable measurement of the number of trapped atoms, the signal from the PMT (shown in the vertical axis of these spectra) has no physically clear meaning. For this reason, their maxima have been rescaled to 10 so as to

compare the relative heights of the peaks which are shown in figure 7-3.

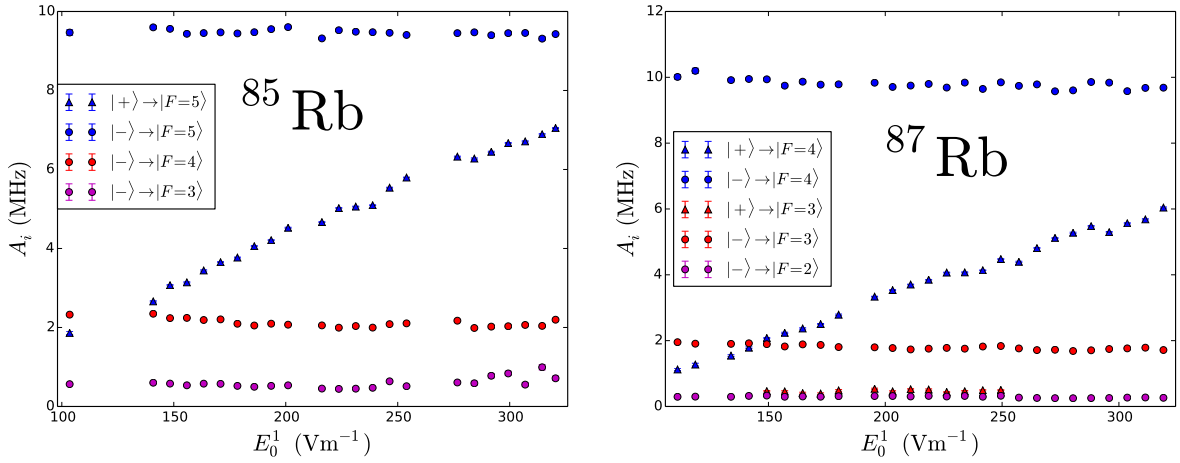

Figure 7-3: The relative heights of the Voigt peaks fitted to the spectra for all values of E_0^1.

As the intensity is increased the Autler-Townes pair is further split, and their relative heights become more symmetric. This matches the theory developed in subsection 2.5.1. These tendency graphs have experimental data in the horizontal axis and fitted parameters in the vertical axis. Vertical error bars are derived through the numerical approximation described in section 6.3.

The variation in the position of the peaks is shown in figure 7-4. As the intensity is increased the Autler-Townes splitting increases as expected. The mid point between the Autler-Townes pairs is indicated and with blue red and purple horizontal lines for each Autler-Townes pair (that is where the naked transition must be). An average for the position of this naked transition is taken for the main peak and used to deduce the position of the others using the known hyperfine separation. The fact that the midpoints for the second Autler-Townes pair ^{87}Rb do not coincide with this can be attributed to the overlaping of peaks, which makes difficult the precise localization of peaks.

For the main peaks the frequency difference between the peaks is shown as a function of E_0^1 in figure 7-5. According to theory this difference should be $\Delta\nu = \sqrt{(\Omega^1)^2 + (\delta^1)^2} = \sqrt{(e\wp_{21}/h)^2(E_0^1)^2 + (\delta^1)^2}$ for some effective Rabi frequency Ω^1. This expression is fitted to the data for values of $\wp_{21}$ and δ^1.

The fitted curves match closely the data, and the values obtained for δ^1 are in the range of 0-14 MHz expected from the characterization of the MOT in [61]. Remarkably, the values of $\wp_{21}$ are very close to half the 8.453 a_0 calculated in chapter 3 as the reduced matrix element of the $5S_{1/2} \rightarrow 5P_{3/2}$ transition. If one considers the atom to be purely in the cooling cycle from equation 3.1 it can be seen that for ^{85}Rb (^{87}Rb) the only relevant coupling will be that for $J_i = 3/2, F_i = M_i = 4(3), J_j = 1/2 F_j = M_j = 3(2), p = 1$.

For both isotopes

$$\langle N_i L_i J_i F_i M_i | T_p^1(\widehat{\vec{r}}) | N_j L_j J_j F_j M_j \rangle = \frac{1}{2}(N_i L_i J_i || T^1(\widehat{\vec{r}}) || N_j L_j J_j),$$

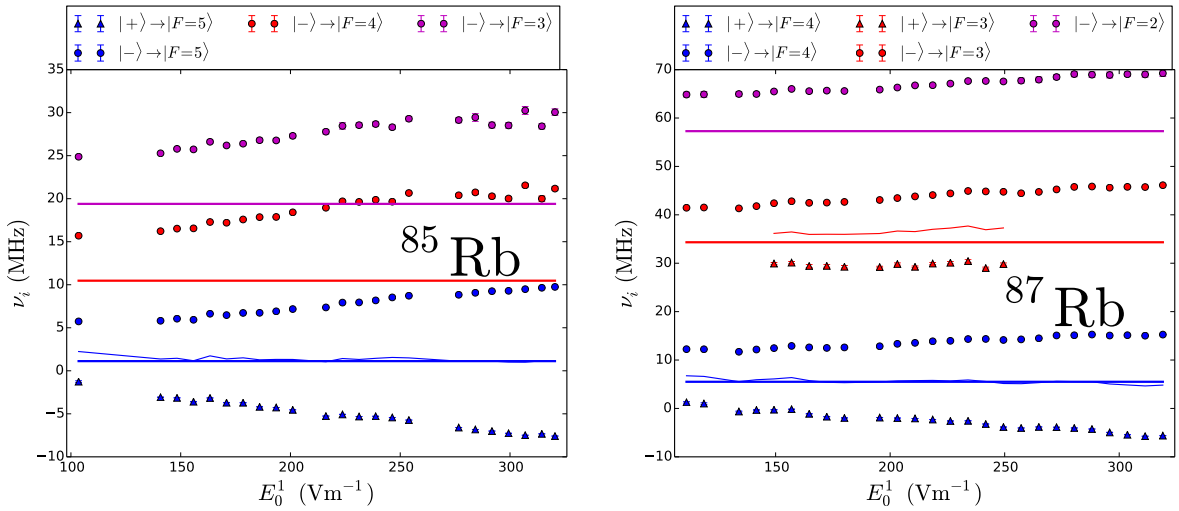

Figure 7-4: The centres of the Voigt peaks fitted to the spectra for all values of E_0^1.

which explains the fact that the effective matrix element is half the reduced matrix element in the simplified model.

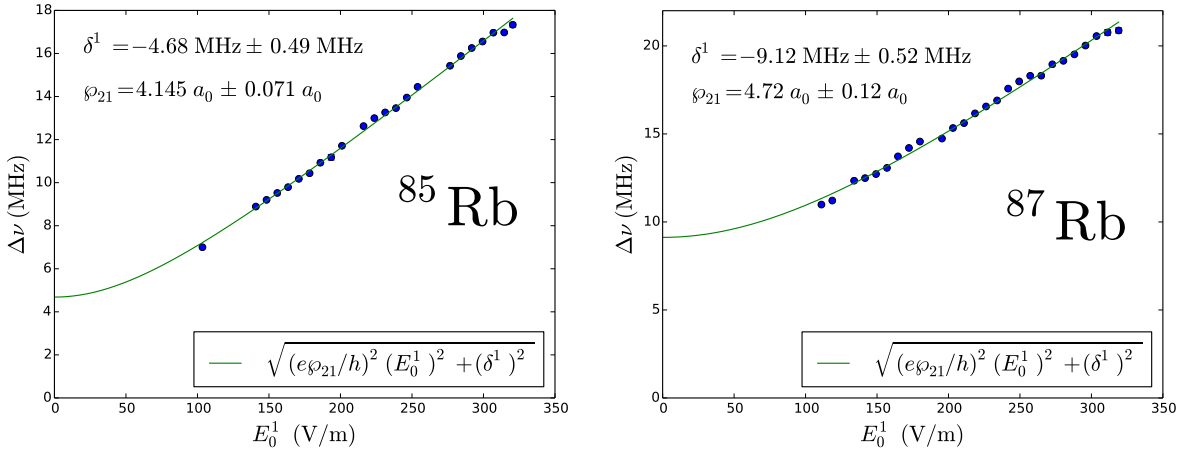

Figure 7-5: The frequency difference between the two main Voigt peaks for all values of E_0^1.

The FWHM of the Voigt profiles are shown in figure 7-6 and exhibit a clear linear tendency. At higher intensity there is higher broadening, which is attributable to the rising of temperature caused by the transference of momentum, and the Doppler effect broadening associated with it. This is consistent with the experimental findings in [71] and [72] where the temperature of the atomic cloud has been measured to increase with the intensity of the cooling beam.

Notice that all these fitted quantities are shown here with the error bars calculated from the inverse Hessian matrix as described in section 6.3, but in many cases they are very small. This happens when the Voigt fits are very good, but this may be only a lower bound of the error bars.

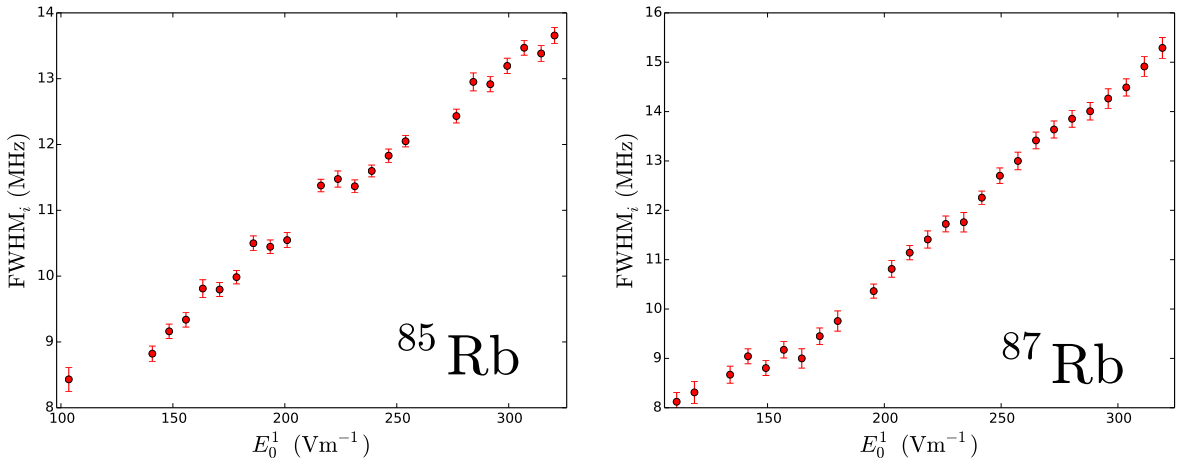

Figure 7-6: The FWHM of the Voigt peaks fitted to the spectra for all values of E_0^1.

7.1.2 Multilevel model

Figures 7-7 (7-8) show the same spectra already shown for the simplified analysis E_0^1 for ^{85}Rb (^{87}Rb) using now the multilevel model as described in chapters 3 and 6.

We can see good agreement between the multilevel model and the experimental data. The residues of the theoretical spectra relative to the experimental data are shown below each spectrum and they are at most 7.14 % of the total height of the spectra.

At high intensity the Autler-Townes peaks show many other peaks within them. This can be attributed to the multitude of polarization components driving the transitions and the differences between their couplings. Each channel splits according to different Rabi frequencies given by their respective couplings r_{pij}. Previous studies have resolved this M_F-specific Autler-Townes splitting [13,41,46]. For instance, for ^{85}Rb (^{87}Rb) in the highest Autler-Townes peak the M-specific excitations $|F = 4, M = 4(3)\rangle \rightarrow |F = 5, M = 5(4)\rangle$, $|F = 4, M = 3(2)\rangle \rightarrow |F = 5, M = 4(3)\rangle$, $|F = 4, M = 3(2)\rangle \rightarrow |F = 5, M = 3(2)\rangle$ can be distinguished from left to right.

Furthermore, in figure 7-9 the imaginary parts of the coherences for these transitions are shown for three different choices of M_i, M_j. The fluorescence has been rescaled to show the correlation with coherences. It can be seen that the different peaks in the fluorescence correspond to various excitation paths visible in the coherences. The broadening from the convolution hides this multi-channel splitting, resulting in theoretical spectra that very closely match the measured data. This shows that the detailed theoretical analysis developed in this work allows the different contributions of the excitation paths to be resolved.

At low intensity there is some discrepancy between the relative heights of the peaks. This is attributable to several effects. Firstly, not all model-parameters are fitted, importantly the MOT beams are taken to be perfectly circular, so any defect in their polarization is not taken into account.

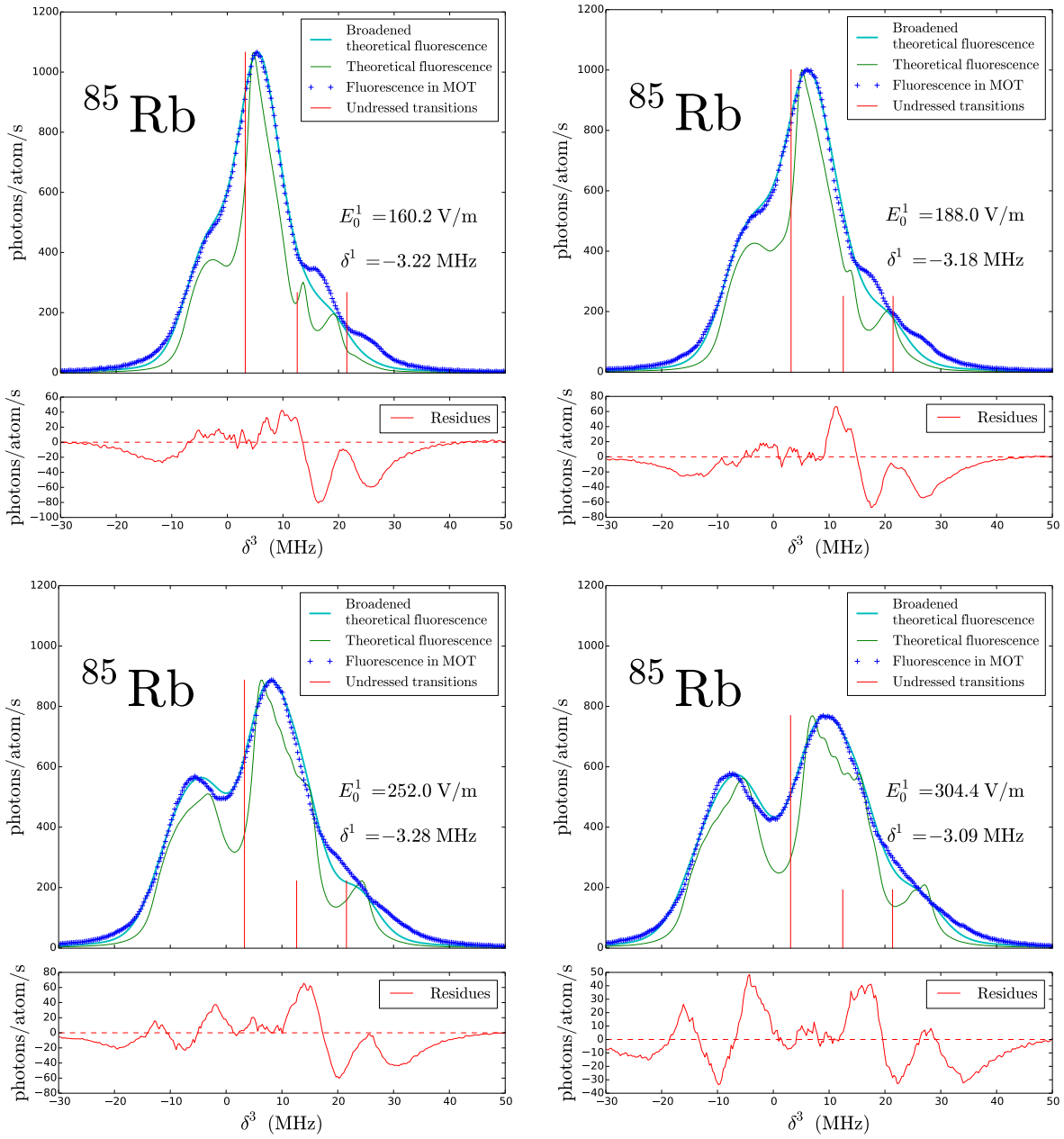

Figure 7-7: Spectra for different values of E_0^1 in ^{85}Rb.

Also, the quantization axis is taken to be precisely the $\hat{z}$ axis as shown in figure 4-1. However, the probe beam (although it is taken at a constant and low power) breaks the symmetry of the effective polarization of the atoms. Therefore, the proper quantization axis is slightly different than $\hat{z}$.

In addition to this, the magnetic field of the MOT contributes differently to the polarization at different points of the atomic cloud. A more complete calculation would have to consider the different contributions of different points of the cloud using rotations of the quantization axis as

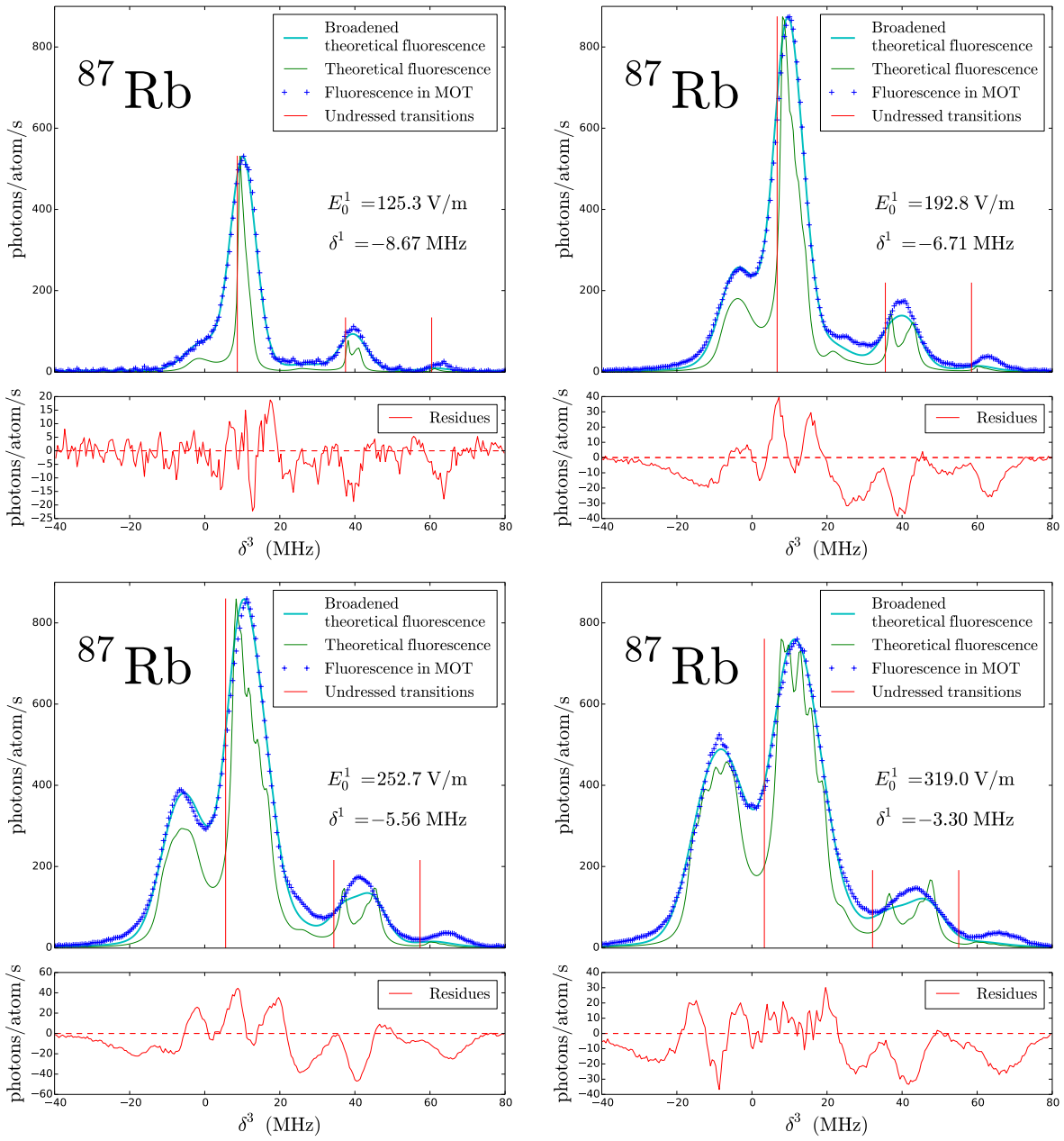

Figure 7-8: Spectra for different values of E_0^1 in ^{87}Rb.

dictated by the MOT magnetic field, with each contribution weighted by the local density of the cloud. Since this level of detail of the properties of the cloud is very difficult to measure, all the atoms are taken to be at the centre of the cloud using the $\hat{z}$ axis as the quantization axis.

It is also noticeable that the relative height discrepancies are greater for ^{85}Rb than for ^{87}Rb. One way to explain this is that the frequency differences between hyperfine states in ^{85}Rb are significantly smaller than those in ^{87}Rb. This means that errors in the voltage-to-frequency callibration of the former are more important. A smaller frequency-to-voltage ratio leads to peaks that are closer to

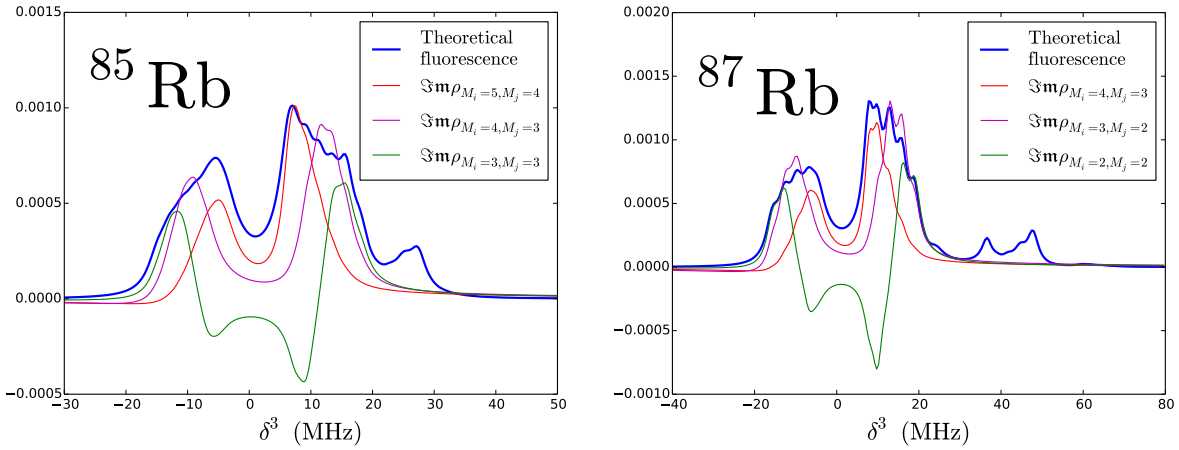

Figure 7-9: The imaginary parts of the coherences for ^{85}Rb (^{87}Rb) from transitions $5P_{3/2}F = 4(3) \rightarrow 5D_{5/2}F = 5(4)$ are shown for three different choices of M_i, M_j.

each other. This means that the optimization process leads to higher values of E_0^1. This in turn exaggerates the Autler-Townes splitting and when the convolution joins the split peaks they show with smaller heights.

Vertical error bars are derived through the numerical approximation described in section 6.3. Horizontal error bars are obtained by propagating the error from direct measurements as described in chapter 5.

The tendencies of the fitted values of the detuning of the reference laser δ_{ref}^1 are shown in figure 7-10. They show no clear tendency outside the error bars, which is consistent with a well-stabilized frequency for the reference laser. Noticeably, the error bars are larger at lower powers. When the power of the cooling beam decreases, there are less atoms able to contribute to the spectra and there is a lower signal. This leads to a smaller signal-to-noise ratio and therefore to greater error bars.

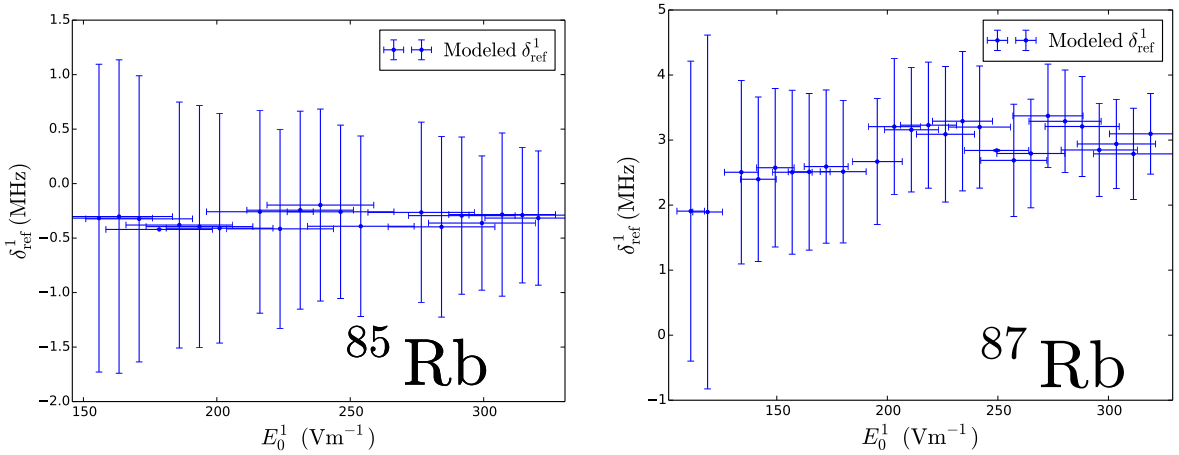

Figure 7-10: The fitted values of the detuning of the reference laser δ_{ref}^1 on the left for ^{85}Rb and on the right for ^{87}Rb.

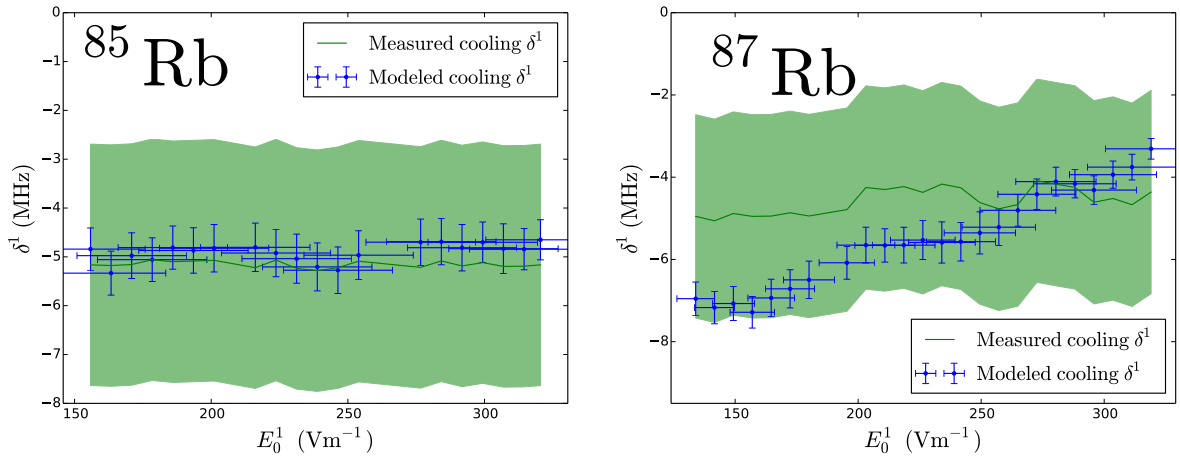

Figure 7-11: The fitted values of the detuning of the cooling laser δ^1 on the left for ^{85}Rb and on the right for ^{87}Rb.

The fits for δ^1 are shown in figure 7-11 together with the experimental values as deduced from the values δ^1_{ref} obtained from the fits. The fitted and measured values do match for ^{85}Rb within experimental and theoretical error bars. For ^{87}Rb they do not lie within the error bars calculated from the fit. However, they are within the 4.9 MHz error associated to the measurement of $\delta^1 - \delta^1_{\text{ref}}$ through the beat. This experimental error is shown as a green shade. Also, this is a small error compared to the 120 MHz (266 MHz) between the $F = 3(2)$ and $F = 2(1)$ hyperfine levels of the $5P_{3/2}$ multiplet for ^{85}Rb (^{87}Rb).

The data points correspond to spectra that were measured in order of increasing power, and so the variation of detuning for ^{87}Rb, is attributable to a drift in the frequency lock of the laser throughout the five to six hours that the data acquisition lasted. This indicates that the analysis using the multilevel model gives information about the conditions of measurement that are beyond the precision with which the experimental parameters could be determined.

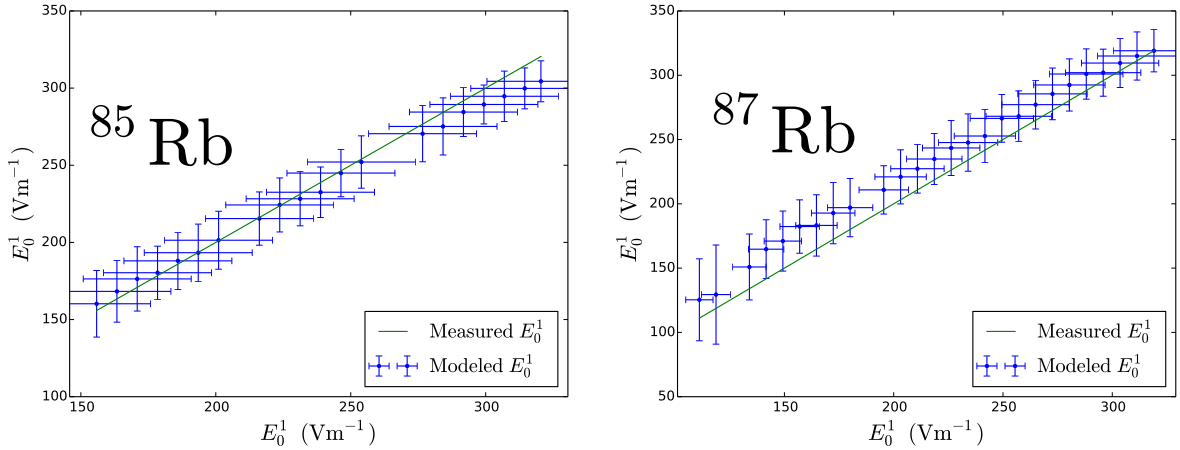

Figure 7-12: The fitted values of E_0^1 on the left for ^{85}Rb and on the right for ^{87}Rb.

The values fitted for the electric field amplitude E_0^1 are shown in figure 7-12. The measured and theoretical values of E_0^1 match to within both experimental and theoretical error bars, although there is a systematic underestimation of the measured values. This is attributable to not capturing all of the beam light in the power-meter. Noticeably, the error bars (obtained as explained in subsection 5.6 and section 6.3) are of similar magnitude, meaning that the fitting procedure could be used to estimate the electric field amplitude with a precision similar to that of the measurements.

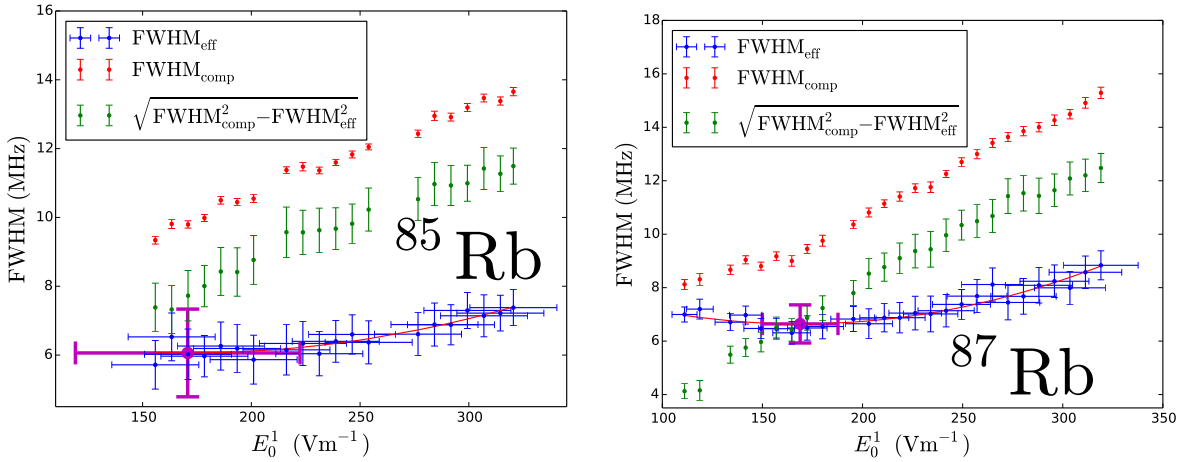

Figure 7-13: The experimental values δ^1 in the horizontal axis, and the fitted values of the FWHM that is convolved with the theoretical spectra. A second order polynomial is fitted to the data, and the corresponding minima are shown as green points (with their corresponding errors).

The broadening FWHM_{eff} obtained from the model are shown in figure 7-13 and (like those obtained by the Voigt fit) exhibit a clear tendency. Notice that these are the FWHMs associated to each gaussian distribution convolved with each of the spectrum obtained from the equations for monochromatic light and static atoms. In other words, these are purely the widths from broadening effects (but not power broadening), while those presented in the previous subsection are the complete widths of the peaks. For this reason they should not be expected to coincide, but only that the complete width is larger (as is indeed the case).

The complete widths obtained in the previous section are shown in figure 7-13 as red points for comparison. It is also possible to calculate the *difference* between these two widths to obtain the width component corresponding to natural widths and power broadening (shown in green).

At lower intensity the multilevel model shows an increase of broadening and there is a beam intensity with a minimum broadening. This may be explained by the presence of two opposing effects as described in section 4.2. On one side, higher intensity leads to higher momentum transfer to the atoms and therefore to higher temperatures. On the other side, very low intensities reduce the Rabi frequency of the cooling mechanism.

This shows that the analysis using the multilevel model allows us to identify the optimal intensity of the cooling beams to achieve the lowest temperature in the atomic cloud. In order to find this

optimal intensity a second order polynomial is fitted to the data (shown as red lines). The coefficients of these fits are then used to find the minimum, and the corresponding error bars are obtained propagating the error from the fits (shown as a green dot with thick error bars). Remarkably, the fits for ^{85}Rb (^{87}Rb) agree on the smallest broadening FWHM 6.06 MHz $\pm$ 1.27 MHz (6.64 MHz $\pm$ 0.71 MHz), and the corresponding the electric field amplitude 170.7 Vm^{-1} $\pm$ 51.6 Vm^{-1} (168 Vm^{-1} $\pm$ 18.9 Vm^{-1}).

The coincidence of the minimal widths is attributable to the fact that both clouds are cooled by the same beam, that is, by radiation with the same line width. Since both isotopes have the same reduced matrix element, and the atoms are effectively in the cyclic transition their coupling to the light is effectively the same, and therefore they are cooled to the same temperature.

This temperature can be calculated through equation 3.6. The widths of the cooling and pump lasers are obtained from the beat shown in 5.5 by assuming that the reference, cooling and repump lasers have the same width. This assumption is based on the fact that they are all ECDLs of similar arquitecture and diodes. Hence FWHM^1 = FWHM^2 = (4.94 MHz $\pm$ 0.147 MHz)/$\sqrt{2}$ = 3.4 MHz $\pm$ 0.104 MHz. The width of the probe beam is approximately 50 kHz (as indicated by the manufactor), and so is practically negligible.

In this manner, the minimum temperatures for ^{85}Rb (^{87}Rb) are calculated to be 346 μK $\pm$ 437 μK (555 μK $\pm$ 269 μK). Although the errors in these quantities are relatively large, they coincide with the characterization of the MOT [61] made in the LAF-ICN that shows temperatures in the range of $250 - 1600$ μK. These temperatures however, are significantly above those obtained in [72] and [71] which are in the range of $10 - 300$ μK.

7.2 Detuning Variation of the First-step Beam

7.2.1 Simple Model

Figures 7-14 (7-15) show representative spectra for a range of values of $\delta^1 - \delta^1_{\text{ref}}$ for ^{85}Rb (^{87}Rb). These were obtained with a measured electric field amplitude of 128 ± 52 V/m.The residues of this fits are shown below each spectra and although for a few points of the cell fit they are as high as 15 % of the height of the spectra, typically they are below 2 % for both the cell and MOT fits. These spectra also show Autler-Townes splitting in all the data series.

Each hyperfine transition is shown as indicated by the literature cited in section 3 The spectra in MOT show Autler-Townes splitting for all detunings. The first peak is split into the transitions $|\pm\rangle \rightarrow 5D_{5/2}F = 5(4)$ which are clearly visible for both isotopes. For large detunings the Autler-Townes pairs corresponding to each of the hyperfine transitions become so separate that different pairs overlap, and the peaks are difficult to distinguish.

As in section 7.1, varying the frequency of the cooling beam changes both the fluorescence per

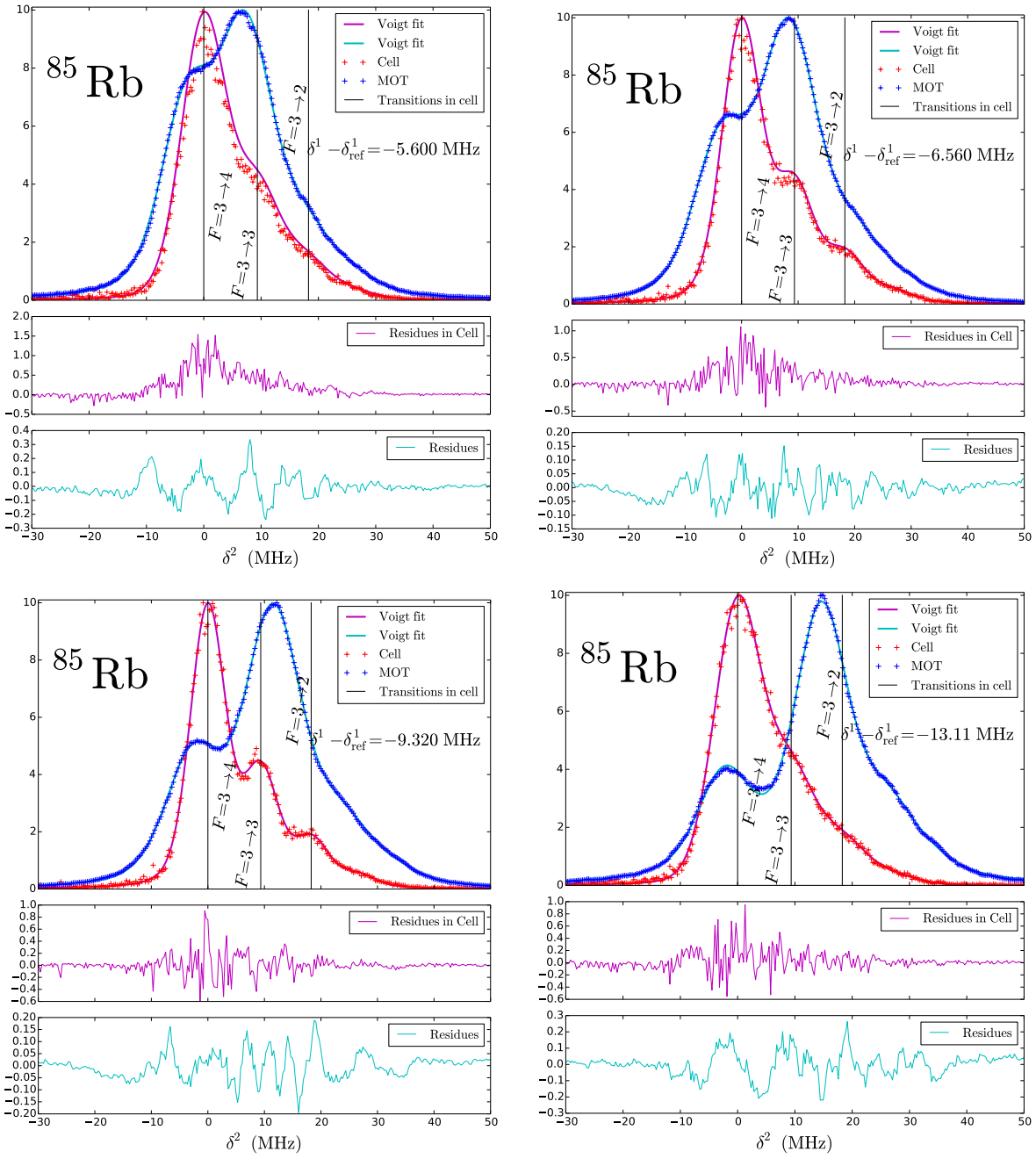

Figure 7-14: Spectra for different values of $\delta^1 - \delta^1_{\text{ref}}$ in ^{85}Rb. Hyperfine transitions of $5P_{3/2} \rightarrow 5D_{5/2}$ are indicated for the cell spectroscopy. The residues of Voigt fits for both spectroscopies are shown.

atom and the number of trapped atoms. The data have been rescaled to 10 in order to better compare the relative heights of the peaks shown in figure 7-16. Voigt profiles are fitted both to the reference spectra used to produce the frequency calibration and for the spectra obtained in the MOT. Once again, the tendency graphs have experimental data in the horizontal axis and fitted parameters in the vertical axis (and error bars are obtained accordingly).

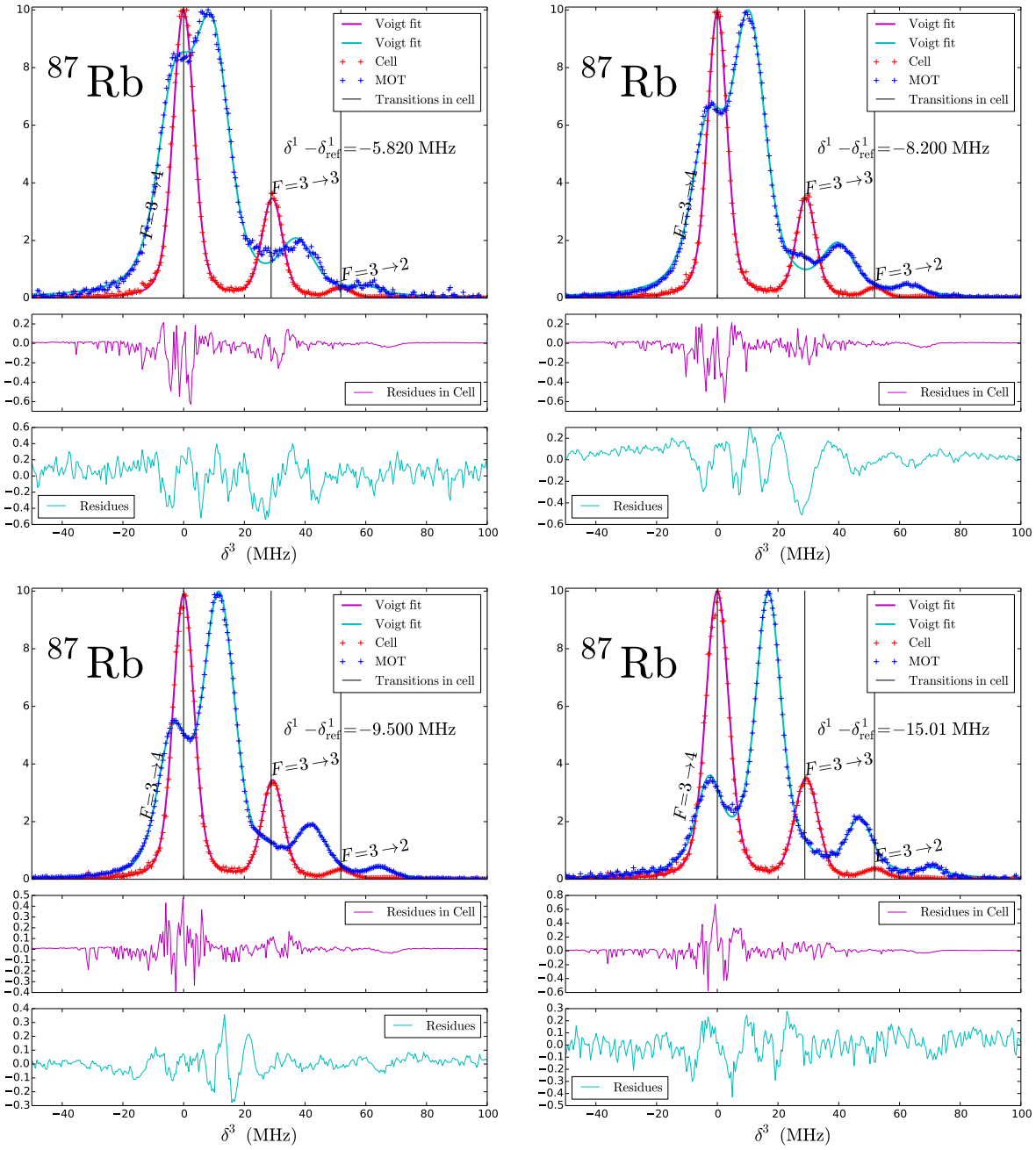

Figure 7-15: Spectra for different values of $\delta^1 - \delta^1_{\text{ref}}$ in ^{87}Rb. Hyperfine transitions of $5P_{3/2} \to 5D_{5/2}$ are indicated for the cell spectroscopy. The residues of Voigt fits for both spectroscopies are shown.

As the (negative) detuning is increased the Autler-Townes pairs become more separate in frequency, and their relative heights become less symmetric. This matches the theory developed in subsection 2.5.1.

The variation in the position of the peaks is shown in figure 7-17. As the detuning is increased, the Autler-Townes splitting increases as expected. In this data series, however, there is no way to obtain a fit of $\sqrt{(\Omega^1)^2 + (\delta^1)^2}$ since there is no measurement of the cooling detuning δ^1 or the

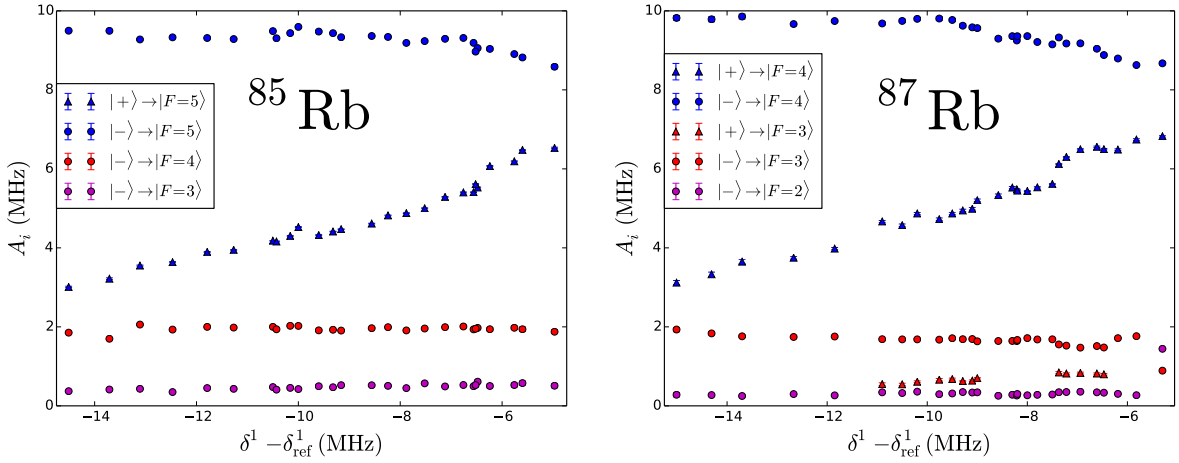

Figure 7-16: The relative heights of the Voigt peaks fitted to the spectra for all values of $\delta^1 - \delta^1_{\mathrm{ref}}$.

reference laser detuning δ^1_{ref}, but rather of $\delta^1 - \delta^1_{\mathrm{ref}}$. Despite this reservation, whatever the actual values of δ^1 are, the difference between levels must still be linear at high values of $\delta^1 - \delta^1_{\mathrm{ref}}$ if the value of δ^1_{ref} is relatively stable.

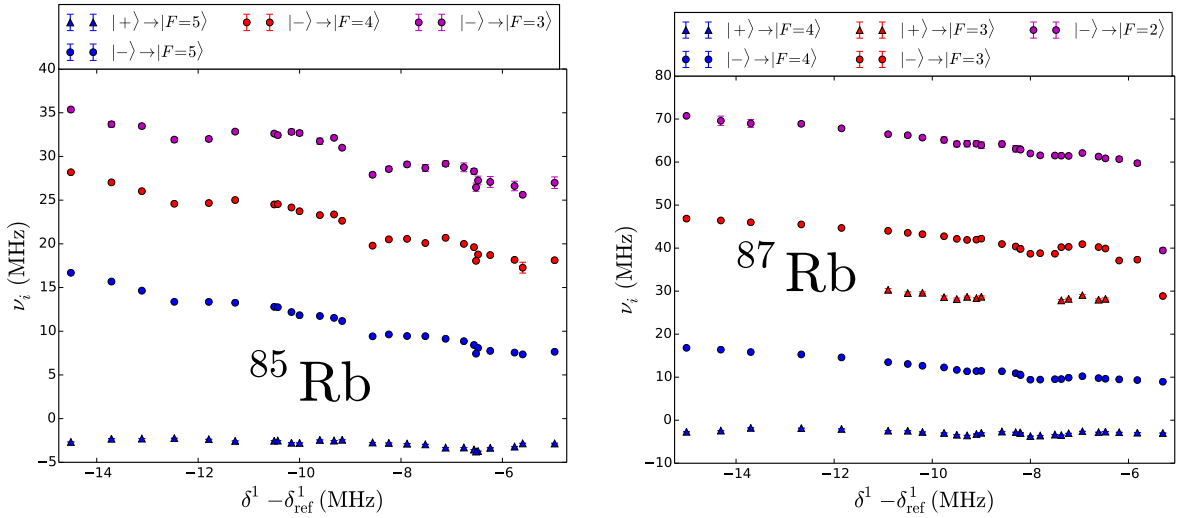

Figure 7-17: The centres of the Voigt peaks fitted to the spectra for all values of $\delta^1 - \delta^1_{\mathrm{ref}}$.

The FWHM of the Voigt profiles are shown in figure 7-19, and for ^{87}Rb they show a clear tendency to decrease as the (negative) detuning increases. This can be easily explained from lower temperatures for greater detunings. However, ^{85}Rb does not show a clear tendency. Because of the greater proximity of hyperfine transitions in this isotope, various excitation paths overlap, which reduces the sensibility of the cooling process to detuning variations.

As in the previous section, these fitted quantities are shown here with error bars that are considerably small in many cases and may be only a lower bound.

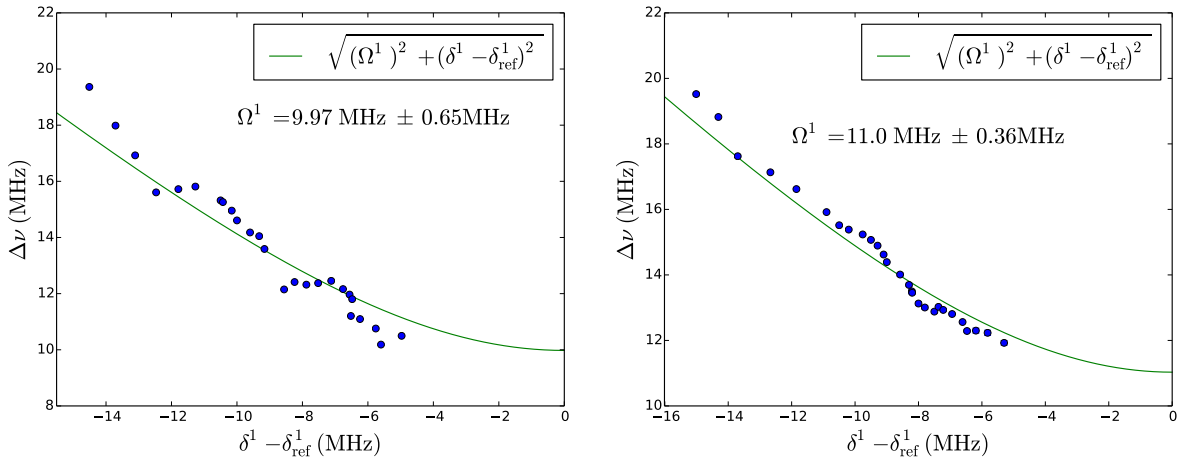

Figure 7-18: The frequency difference between the two main Voigt peaks for all values of $\delta^1 - \delta^1_{\text{ref}}$.

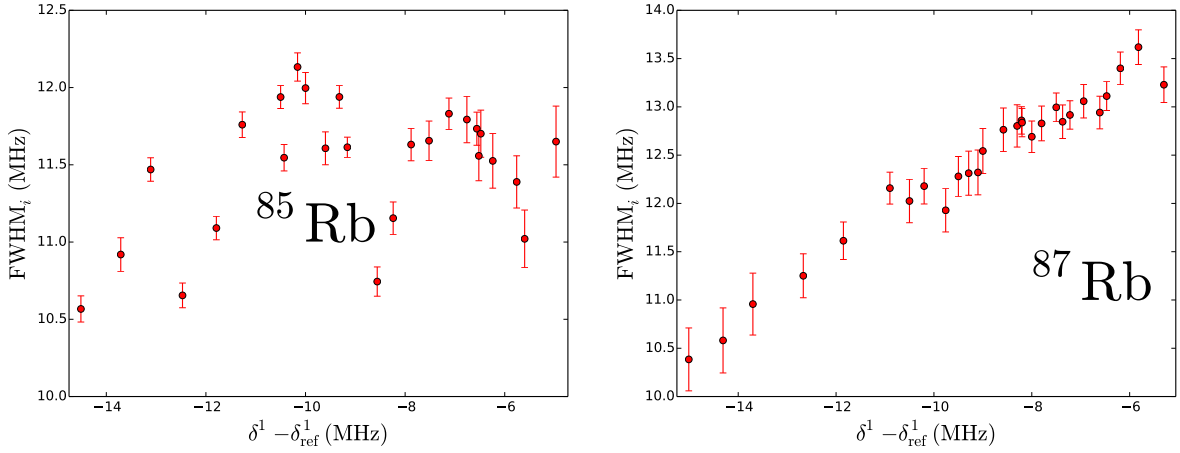

Figure 7-19: The FWHM of the Voigt peaks fitted to the spectra for all values of $\delta^1 - \delta^1_{\text{ref}}$.

7.2.2 Multilevel Model

Figures 7-20 (7-21) show representative spectra for a range of values of $\delta^1 - \delta^1_{\text{ref}}$ for ^{85}Rb (^{87}Rb). The residues of the theoretical spectra relative to the experimental data are shown below each spectrum and they are at most 9.75 % of the total height of the spectra.

As the (negative) detuning is increased the Autler-Townes pairs become more separate in frequency, and their relative heights become less symmetric. This matches the theory developed in chapter 2. The variation of the detuning is noticeable in the position of the undressed transitions shown in red.

It can be seen that for ^{87}Rb some spectra fit well in the area between the highest peaks and the next ones. This is because a Voigt profile cannot always be fitted for $|+\rangle \rightarrow |F = 4\rangle$ Autler-Townes peak, but when it is possible, the fit improves.

Discrepancies between experimental and theoretical spectra can be explained in similar ways as those for intensity variation. The polarization is taken as exactly circular and exactly linear as shown in figure 4-1. A different combination of polarizations will lead to a different distribution of populations of the $5P_{3/2}$. In particular, the optical pumping will be less efficient and states other than those in the cyclic transition will contribute more, leading to higher peaks in the $5P_{3/2}F = 4(3) \rightarrow 5D_{5/2}F' = 4, 3(3, 2)$ transitions for ^{85}Rb (^{87}Rb).

Another source of error is that an effective quantization axis is used based on the symmetry of the radiation and magnetic fields in the MOT. This symmetry is broken by the probe field. Local variations across the atomic cloud of the atom polarization, the atom density, the intensity of the light fields, and the Zeeman shifts as explained in section 6.4.

A bias of the optimization process to fit the main peak $5P_{3/2}F = 4(3) \rightarrow 5D_{5/2}F' = 5(4)$ for ^{85}Rb (^{87}Rb) also introduces error. The Autler-Townes pair of this peak has a greater number of data points, and therefore the optimization process prioritizes the fitting of this pair of peaks. Furthermore, since these peaks are higher, the residues from these data points are larger than those for the smaller peaks, further increasing the bias of the optimization. This also explains why the residues are slightly larger for the smaller peaks.

A more detailed simulation taking into account these details could be done, resulting in better fits, however the current approximation seems enough to obtain the desired insight. The time needed to complete this optimization is about 3 days (18 hours) for ^{85}Rb (^{87}Rb).

The tendencies of the fitted values of δ^1_{ref} are shown in figure 7-22. As in the previous section, the tendency graphs have experimental data in the horizontal axis and fitted parameters in the vertical axis (and error bars are obtained accordingly). The fits for ^{85}Rb appear constant within the error bars, however, for ^{87}Rb there is a jump corresponding to a point during the data acquisition in which the lock of the reference laser was lost and then recovered (at a different frequency shown in green). Both frequency locks are shown with different colours. Apart from this jump, there is no

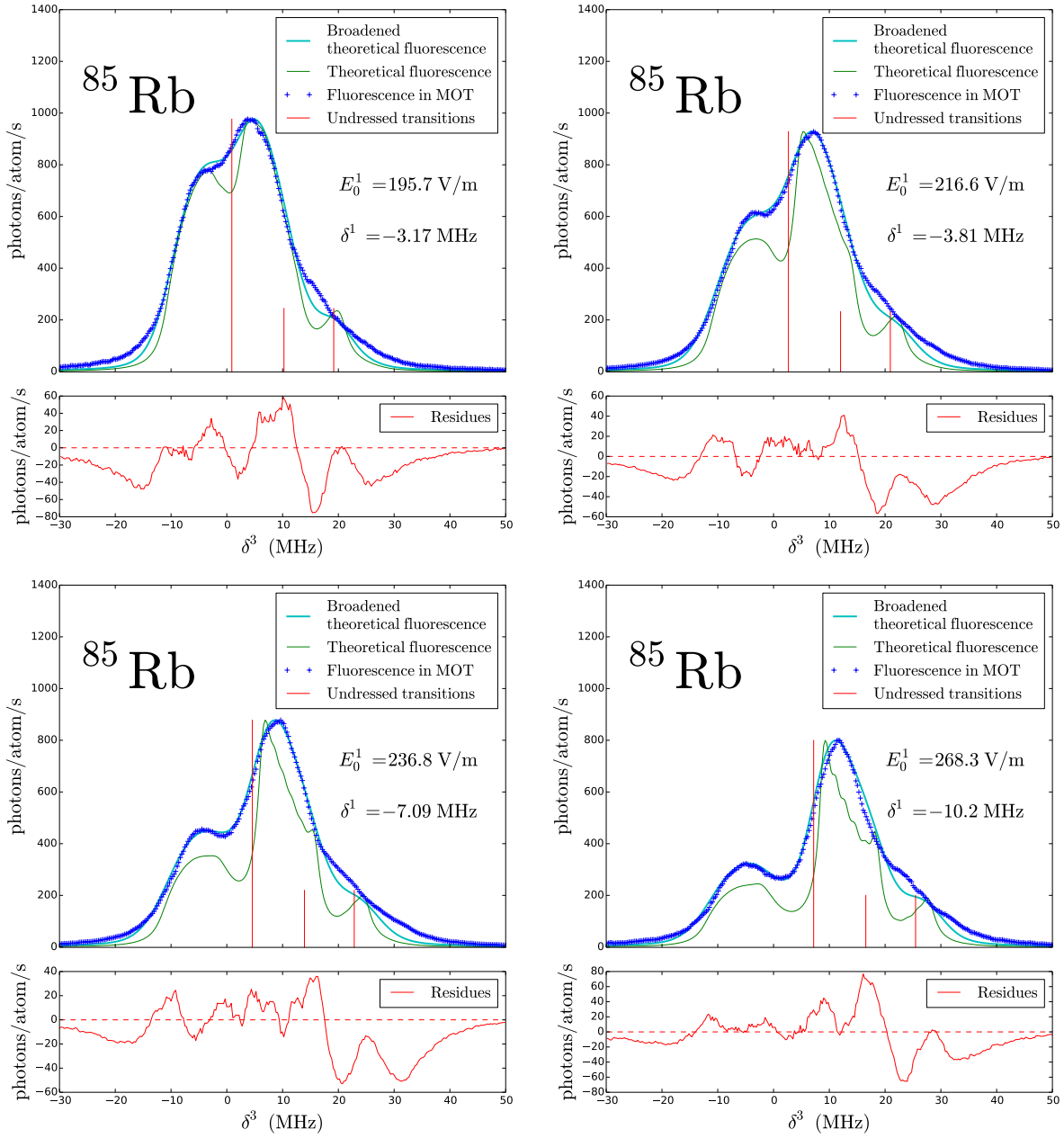

Figure 7-20: Spectra for different values of δ^1 in ^{85}Rb.

clear tendency within the error bars for ^{87}Rb either. Again, the error bars are larger at lower powers as expected. Notice however, that this does not imply that the measurement of relative detunings is less precise, only that the estimation from the model is affected by lower signal-to-noise ratios.

The fits for δ^1 are shown in figure 7-23. The horizontal axis shows the experimental measurement obtained from the measurement of the relative detuning and the theoretical estimation of δ^1_{ref}, and the vertical axis shows the theoretical estimation of δ^1 from the fits. A perfect match between these would correspond to points along a line at 45° from the horizontal axis (shown in green).

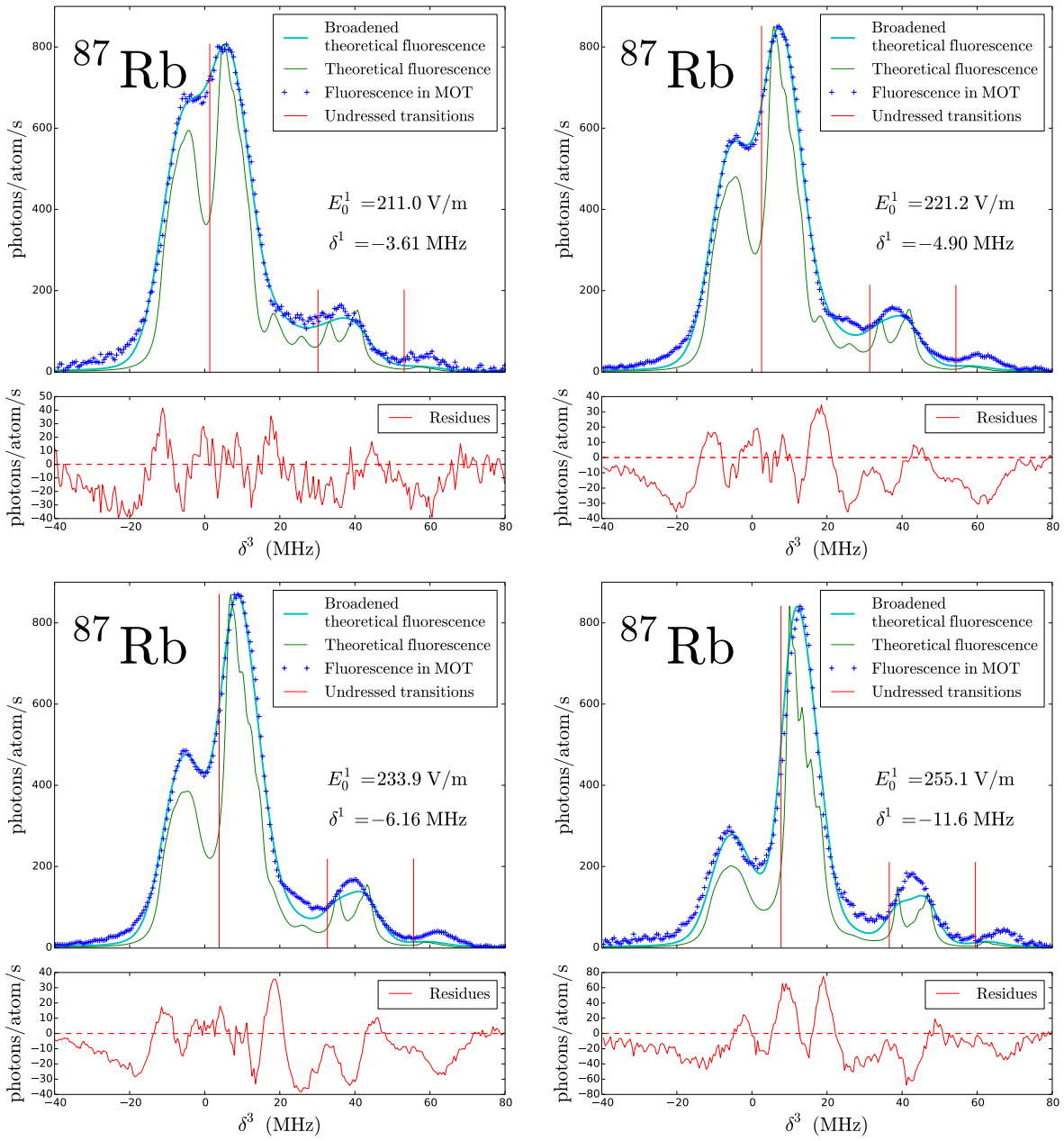

Figure 7-21: Spectra for different values of δ^1 in ^{87}Rb.

There is very good correspondance between experimental and theoretical spectra for both isotopes. Noticeably, the theoretical error bars are significantly smaller than the experimental ones, thus providing a more precise estimation of the actual value of δ^1.

The fitted values of E_0^1 are shown in figure 7-24. There is a clear trend showing a reduction in light intensity that should not be correlated with the detuning. However, this can be explained as a drift in the output power of the laser during the time that the data acquisition lasted (several hours). The experimental error of the determination of the electric field amplitude is shown as a

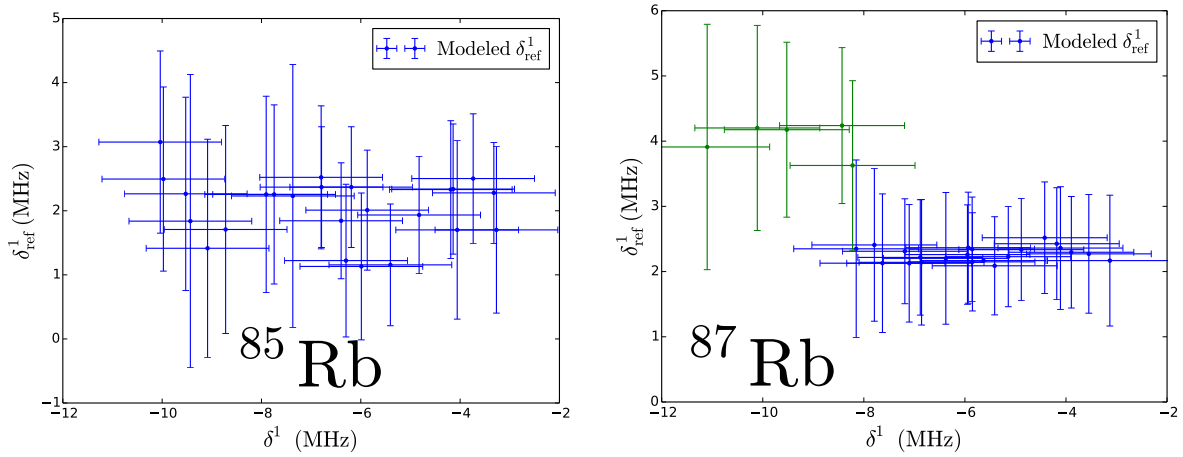

Figure 7-22: The fitted values of δ^1_{ref} on the left for ^{85}Rb and on the right for ^{87}Rb. Points that were taken before a jump in the frequency lock are shown in green for ^{87}Rb.

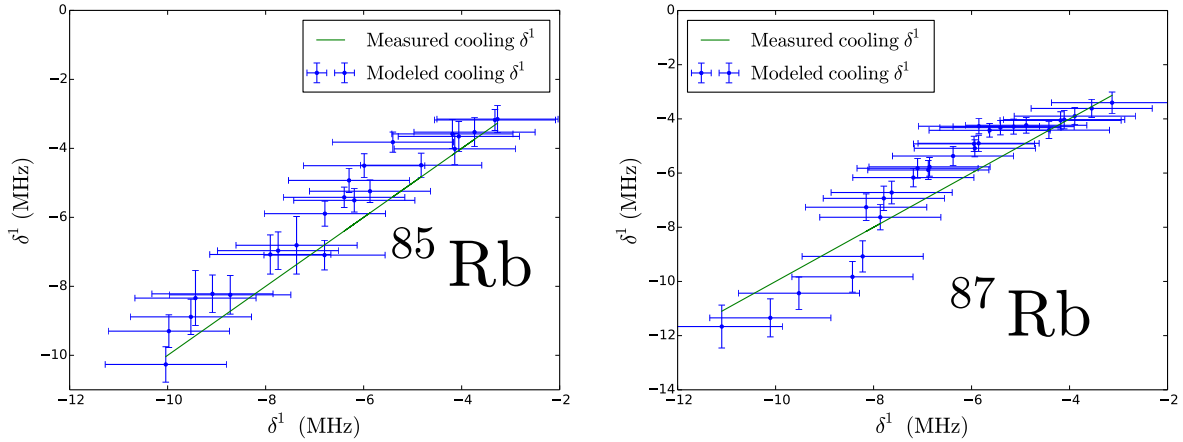

Figure 7-23: The horizontal axis shows the experimental values obtained from the direct measurement of $\delta^1 - \delta^1_{\text{ref}}$ and the fitted values of δ^1_{ref}. The vertical axis shows the fitted values of δ^1 on the left for ^{85}Rb and on the right for ^{87}Rb.

green shadow. The theoretical estimations are contained within this error, and exhibit the drift that could not be detected with the power-meter. Thus we can consider the fitting procedure as an alternative method to detect small changes in the output power of lasers.

The FWHM obtained from the model are shown in figure 7-25 and exhibit a clear tendency for ^{87}Rb. A greater (negative) detuning produces a smaller FWHM, which is attributable to lower temperatures. This analysis shows the same minimum FWHM (approximately 6 to 6.5 MHz) as the analysis from the variation of E^1_0.

Once again, it should be noted that these are the FWHMs associated to each gaussian distribution convolved with each of the spectrum obtained from the equations for monochromatic light and static atoms. In other words, these are purely the widths from broadening effects, while those presented in the previous subsection are the complete widths of the peaks. For this reason they should not be

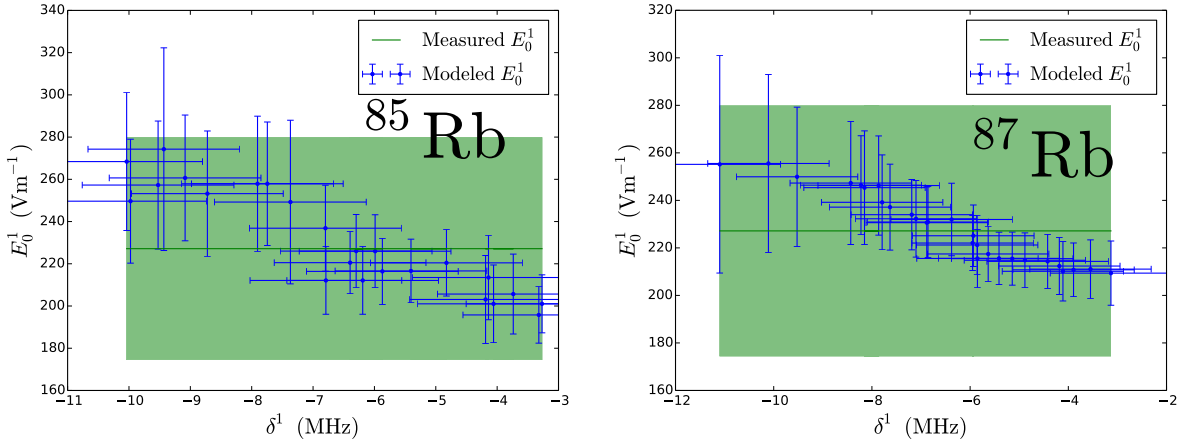

Figure 7-24: The fitted values of E_0^1 on the left for ^{85}Rb and on the right for ^{87}Rb.

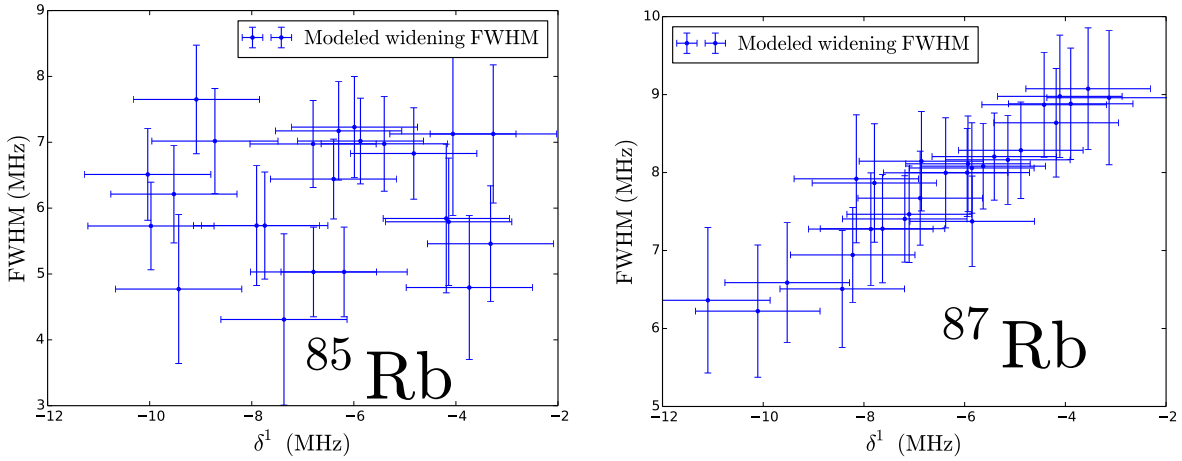

Figure 7-25: The experimental values δ^1 in the horizontal axis, and the fitted values of the FWHM that is convolved with the theoretical spectra.

expected to coincide, but only that the complete width is larger (as is indeed the case).

Although the fitted broadening FWHM for ^{85}Rb do not show a clear tendency, they do seem to indicate lower broadening for greater detunings. This lack of an overall tendency is also consistent with the analysis with Voigt profiles, and can be explained by the non-resonant mixing of hyperfine transitions.

The simplified model was used to produce an estimation of an effective Rabi frequency Ω^1 at zero detuning without taking into account the detuning of the reference laser δ^1_{ref}. The estimation of this number from the multilevel model will be taken into account to make a new estimation of Ω^1. For ^{85}Rb (^{87}Rb) the average value of δ^1_{ref} was 2.2682 MHz (2.2667 MHz). This values are used to calculate δ^1 and with this shifted x axis a new fit is made and shown in figure 7-26.

This new value of Ω^1 is now used together with the estimation of E_0^1 from the complete model: 222.3860 V/m (228.4725 V/m) to calculate the effective coupling constant $\wp_{21} = \frac{\hbar\Omega^1}{eE_0}$. This gives

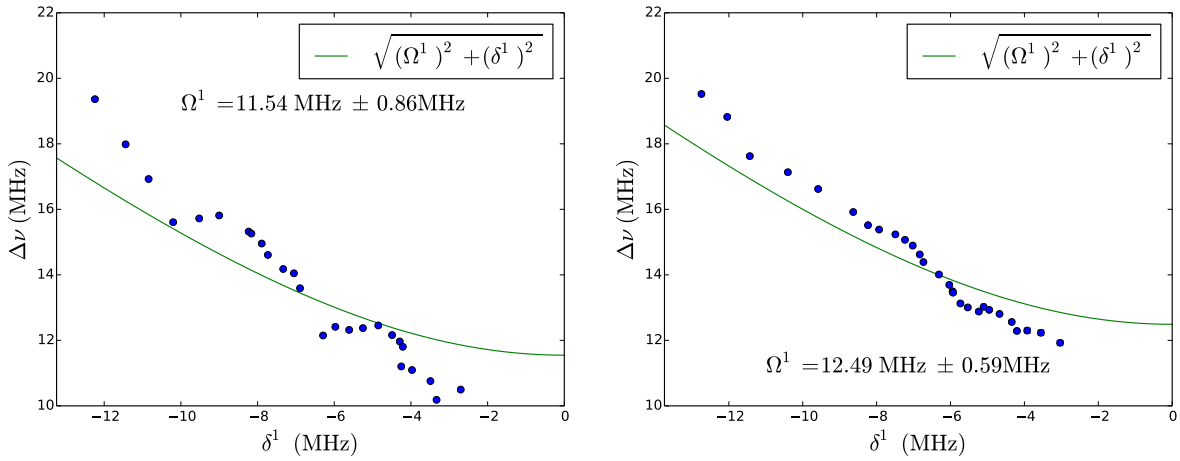

Figure 7-26: The simplified model fitted to the Autler-Townes splitting using the δ^1_{ref} from the complete model.

4.0578 a_0 ± 0.3036 a_0 (4.2725 a_0 ± 0.2032 a_0) which is very close to the result obtained from the simple model and to half the value of the reduced matrix element of the $5S_{1/2} \rightarrow 5P_{3/2}$ transition (8.453 a_0).

Chapter 8

Conclusions

The generalized Optical Bloch Equations developed in this thesis can be used to explain fluorescence spectra of rubidium atoms with different degrees of detail ranging from an effective simplified three level model to a complete model including the full hyperfine and magnetic structure.

These models can be used in a wide variety of experimental conditions, including non-resonant frequencies and intensity above saturation.

The spectra produced from the complete model accurately reproduce experimental data with relative errors that are most 9.75 % although for most data points this is better than 2 %.

Experimental uncertainties are comparable in magnitude to the confidence intervals derived from the theoretical analysis. But the later ones seem to provide more information regarding the wide variety of physical processes occurring in the experiment.

Theoretical spectra from the complete model provide insight about physical quantities otherwise not directly available from the spectra, such as precise detuning, intensity, and temperature variations.

This insight includes separating power broadening from broadening contributions from the Doppler effect and laser widths. Power broadening can further be decomposed in the huge variety of transitions between magnetic states that contribute to the lines measured in the experiment.

An estimation of the temperature of the atomic cloud can be obtained through this separation of broadening contributions.

Variations of the intensity of the beams can be estimated through this method beyond what the precision of the power-meters allow.

If only the states in the $5S_{1/2}, 5P_{3/2}, 5D_{5/2}$ multiplets are taken into account, this theoretical analysis can be done with common computing equipment in the range of minutes to several days. This simplified model produces results that correlate with those of the complete model with a correlation coefficient $R^2 = 0.999957$ (0.999953) for ^{85}Rb (^{87}Rb).

The detailed analysis including magnetic states allows the different contributions of each excitation path to be resolved.

The dependance of the heights and positions of Autler-Townes pairs vary according to what the simplified model qualitatively predicts.

The effective matrix element obtained from the simplified model is approximately half the corresponding reduced matrix element, and this can be explained purely in terms of Wigner symbols derived from angular momentum theory.

8.1 Perspectives

Using the software developed in this thesis to opens a window to exploring spectroscopies before building complicated experiments, or buying expensive equipment.

Optimizing the experimental parameters from theory to make a three photon spectroscopy aimed at Rydberg atoms.

Recording spectra from electric quadrupole transitions.

Developing the terms from the electric quadrupolar Hamiltonian and include the calculations.

Using the dipolar transitions in this thesis to calibrate the voltage to fluorescence correspondance of the PMT.

Using the model to fit the reduced matrix element of the quadrupolar transitions to the measured fluorescence.

Using the fitted reduced matrix element to calculate the quadrupolar decay frequency.

Giving structure to $\vec{E}(\vec{R})$ to explore effects of structured light beams on the spectra. In particular beams with additional orbital angular momentum such as Bessel beams.

Describing the photons themselves developing a generalized Jaynes-Cummings model, and applying this to Cavity Quantum Electrodynamics.

Appendices

Appendix A

Electric Field

For simplicity we will consider the electric field as a linear combination of N_l plane waves, $\vec{E}_0(\vec{R},t) = \sum_l \vec{E}^l(\vec{R},t)$ produced by N_l lasers with arbitrary polarizations, orientations and intensities. In this thesis indices spanning the N_l laser fields will be superindices unless explicitly noted for typesetting convenience. Each component of radiation will be taken to have the form

$$\vec{E}^l(\vec{R},t) = R_{\alpha^l\theta^l\phi^l}\frac{E_0^l(\vec{R})}{2}(\vec{\epsilon}^{\,l(+)}e^{-i\omega^l t} + \vec{\epsilon}^{\,l(-)}e^{i\omega^l t}) = R_{\alpha^l\theta^l\phi^l}E_0^l(\vec{R})\begin{pmatrix}\cos(\omega^l t)\cos(2\beta^l)\\ \sin(\omega^l t)\sin(2\beta^l)\\ 0\end{pmatrix} \quad (A.1)$$

where $\vec{\epsilon}^{\,l(+)} = \overline{\vec{\epsilon}^{\,l(-)}}$ are unitary vectors that contain information about the polarization having the form

$$\vec{\epsilon}^{\,l(+)} = \begin{pmatrix}\cos(2\beta^l)\\ i\sin(2\beta^l)\\ 0\end{pmatrix}, \qquad \vec{\epsilon}^{\,l(-)} = \begin{pmatrix}\cos(2\beta^l)\\ -i\sin(2\beta^l)\\ 0\end{pmatrix}.$$

in the Cartesian base, and $R_{\alpha^l\theta^l\phi^l}$ is a rotation represented by matrices

$$R_{\alpha^l\theta^l\phi^l} = \begin{pmatrix}\cos\phi^l & -\sin\phi^l & 0\\ \sin\phi^l & \cos\phi^l & 0\\ 0 & 0 & 1\end{pmatrix}\begin{pmatrix}\cos\theta^l & 0 & \sin\theta^l\\ 0 & 1 & 0\\ -\sin\theta^l & 0 & \cos\theta^l\end{pmatrix}\begin{pmatrix}\cos 2\alpha^l & -\sin 2\alpha^l & 0\\ \sin 2\alpha^l & \cos 2\alpha^l & 0\\ 0 & 0 & 1\end{pmatrix},$$

in the same Cartesian base. This particular form to specify the orientation of the electric field has been chosen so that ϕ^l, θ^l are angles in spherical coordiantes such that $\vec{k}^l = k^l(\cos\phi^l\sin\theta^l\hat{x} + \sin\phi^l\sin\theta^l\hat{y} + \cos\theta^l\hat{z})$ is the wave vector of the plane wave, and so that α^l describes the effect of half-wave plate and β^l the effect of a quarter-wave plate.

We can express the electric field more compactly as

$$\vec{E}^l(\vec{R},t) = \frac{E_0^l(\vec{R})}{2}(\vec{\varepsilon}^{l(+)}e^{-i\omega^l t} + \vec{\varepsilon}^{l(-)}e^{i\omega^l t})$$

where

$$\vec{\varepsilon}^{l(\pm)} \equiv R_{\alpha^l\theta^l\phi^l}\vec{\epsilon}^{l(\pm)}.$$

In the following treatment of evolution equations we will need to compute at many points the quantity $\hat{r}\cdot\vec{\varepsilon}^{l(\pm)}$. This dot product may be computed in the usual manner using the components of both vectors in the Cartesian basis, however, the matrix elements of the $\hat{r}$ operator are easier to calculate in the so-called *helicity basis*

$$\hat{e}_{-1} = \frac{\hat{x}+i\hat{y}}{\sqrt{2}}, \qquad \hat{e}_0 = \hat{z}, \qquad \hat{e}_{+1} = \frac{\hat{x}-i\hat{y}}{\sqrt{2}}.$$

The components of $\vec{\varepsilon}^{l(\pm)}$ in the Cartesian base will be denoted by $X_q^{l(\pm)}$ and in the helicity basis by $Y_q^{l(\pm)}$

$$\begin{aligned}\vec{E}^l(\vec{R},t) &= \tfrac{E_0^l(\vec{R})}{2}(\vec{\varepsilon}^{l(+)}e^{-i\omega^l t} + \vec{\varepsilon}^{l(-)}e^{i\omega^l t}) \\ &= \tfrac{E_0^l(\vec{R})}{2}\textstyle\sum_{k=1}^{3}[X_k^{l(+)}e^{-i\omega^l t} + X_k^{l(-)}e^{i\omega^l t}]\hat{x}_k \\ &= \tfrac{E_0^l(\vec{R})}{2}\textstyle\sum_{q=-1}^{1}[Y_q^{l(+)}e^{-i\omega^l t} + Y_q^{l(-)}e^{i\omega^l t}]\hat{e}_q\end{aligned} \tag{A.2}$$

Appendix B

Power and the Electric Field

In the laboratory the power of beams is measured instead of the amplitude of the electric fields, therefore we need some way to estimate this electric field using power measurements and the characteristics of the cross section of the beams. According to the Poynting theorem the change in the electromagnetic energy density in a given volume is

$$\frac{du}{dt} = \frac{d}{dt}\left[\frac{\varepsilon_0|\vec{E}|^2}{2} + \frac{|\vec{B}|^2}{2\mu_0}\right] = -(\nabla\cdot\vec{S} + \vec{J}\cdot\vec{E})$$

where $\vec{S} = \vec{E}\times\vec{B}/\mu_0$ is the Poynting vector. Assuming that the light propagates in vacuum $\vec{J} = 0$. Integrating over the volume inside a cylindrical surface oriented along the beam's optical path we get

$$\frac{d}{dt}\int_V udV = -\int_V \nabla\cdot\vec{S} = -\int_{\delta V}\vec{S}\cdot d\vec{A}$$

In this calculation the general orientation of the fields is not of interest, and we can take $\hat{k} = \hat{z}$ without loss of generality. In the vacuum $\vec{B} = \frac{1}{c}\hat{k}\times\vec{E}$, therefore in our example

$$\vec{E} = E_0^l(\vec{R})\begin{pmatrix}\cos(\omega^l t)\cos(2\beta^l)\\ \sin(\omega^l t)\sin(2\beta^l)\\ 0\end{pmatrix}, \qquad \vec{B} = \frac{E_0^l(\vec{R})}{c}\begin{pmatrix}-\sin(\omega^l t)\sin(2\beta^l)\\ \cos(\omega^l t)\cos(2\beta^l)\\ 0\end{pmatrix}.$$

Therefore the Poynting vector is

$$\vec{S} = \frac{E_0^l(\vec{R})}{c\mu_0}[\cos^2(\omega^l t)\cos^2(2\beta^l) + \sin^2(\omega^l t)\sin^2(2\beta^l)]\hat{z}$$

Since $\vec{S}$ is in the $\hat{z}$ direction only the integrals on over the bases of the cylindricl surface are nonzero, so

$$\int_{\delta V} \vec{S} \cdot d\vec{A} = \int_{\text{in}} \vec{S} \cdot \hat{z} da - \int_{\text{out}} \vec{S} \cdot \hat{z} da = 0$$

The power going into the cylinder is the same as the one that goes out, and it can be identified as

$$P(t, z) = \int_{\text{in}} \vec{S} \cdot \hat{z} da$$

Although we have used plane waves here, in the laboratory the beams have some intensity distribution through their cross section that goes to zero with the radial distance ρ. If we take $z = 0$ over the out surface we have

$$P(t) = \frac{E_0^l(\vec{R})}{c\mu_0}[\cos^2(\omega^l t)\cos^2(2\beta^l) + \sin^2(\omega^l t)\sin^2(2\beta^l)] \int_{\text{in}} D(\rho) dA.$$

Where $D(\rho)$ is some intensity distribution. Taking a time average $P = \frac{\omega}{2\pi}\int_0^{2\pi/\omega} P(t)dt$ we get

$$P = \frac{E_0^l(\vec{R})}{2c\mu_0} \int_{\text{in}} D(\rho) dA.$$

As a first approximation we can assume that the intensity distribution is constant within a radius $\rho = a$ and zero outside. In this case (known as a *top hat beam*) the integral becomes

$$P(t) = \frac{\pi E_0^2}{2c\mu_0} a^2 \qquad \Rightarrow \qquad E_0 = \sqrt{\frac{2c\mu_0 P}{\pi a^2}} = \sqrt{2c\mu_0 I} = \sqrt{\frac{2I}{\varepsilon_0 c}}, \tag{B.1}$$

where we have introduced the average intensity $I = P/\pi a^2$.

However, common laboratory beams are usually cannot be considered to have uniform intensity in this way. Another approximation is to use a Gaussian intensity distribution with some astigmatism so it has standard deviations σ_x and σ_y,

$$P = \frac{E_0^2}{2c\mu_0} \int_{\mathbb{R}^2} \exp\left(-\frac{x^2}{2\sigma_x^2} - \frac{y^2}{2\sigma_y^2}\right) dA = \frac{2\pi\sigma_x\sigma_y E_0^2}{c\mu_0} \qquad \Rightarrow \qquad E_0^l = \sqrt{\frac{c\mu_0 P^l}{4\pi\sigma_x^l\sigma_y^l}}. \tag{B.2}$$

There is extensive literature about gaussian beams (for instance [30]) and this is only an approximation to the magnitude of the electric field.

Appendix C

Explicit Matrix Form of Optical Bloch Equations

C.1 Independent Vector

In equations 2.7 the only terms proportional to ρ_{11} will come from the sum of the terms shown in blue

$$\dot{\tilde{\rho}}_{i1} = -\frac{ie}{\hbar}\sum_{l\in L_{i1}} E_0^l \vec{\varepsilon}^{\,l(+)}\cdot\vec{r}_{i1}\rho_{11} + \dots$$

We replace here $\rho_{11} = 1 - \sum_{n=2}^{N_e}\rho_{nn}$ and we get

$$\begin{aligned}\dot{\tilde{\rho}}_{i1} &= -\tfrac{ie}{\hbar}\left(\textstyle\sum_{l\in L_{i1}} E_0^l \vec{\varepsilon}^{\,l(+)}\cdot\vec{r}_{i1}\right)\left(1-\textstyle\sum_{n=2}^{N_e}\rho_{nn}\right)+\dots \\ &= -\left[\tfrac{ie}{\hbar}\textstyle\sum_{l\in L_{i1}} E_0^l \vec{\varepsilon}^{\,l(+)}\cdot\vec{r}_{i1}\right] + \left[\tfrac{ie}{\hbar}\textstyle\sum_{l\in L_{i1}} E_0^l \vec{\varepsilon}^{\,l(+)}\cdot\vec{r}_{i1}\right]\textstyle\sum_{n=2}^{N_e}\rho_{nn}+\dots\end{aligned}$$

so that the quantities in the first bracket are independent on any $\tilde{\rho}_{ab}$, and are precisely the components of the independent vector (with a minus sign). Using the part operator defined in chapter 2 we can see that

$$\begin{aligned} b^{\nu(i,1,s)} &= \mathfrak{Pa}\left(s, \tfrac{ie}{\hbar}\textstyle\sum_{l\in L_{i1}} E_0^l \vec{\varepsilon}^{\,l(+)}\cdot\vec{r}_{i1}\right) \\ &= \tfrac{e}{\hbar}\textstyle\sum_{l\in L_{i1}} E_0^l \mathfrak{Pa}(s, i\vec{\varepsilon}^{\,l(+)}\cdot\vec{r}_{i1}) \\ &= -s\tfrac{e}{\hbar}\textstyle\sum_{l\in L_{i1}} E_0^l \mathfrak{Pa}(-s, \vec{\varepsilon}^{\,l(+)}\cdot\vec{r}_{i1}) \qquad , \\ &= \begin{cases} -\tfrac{e}{\hbar}\textstyle\sum_{l\in L_{i1}} E_0^l \Im\mathfrak{m}(\vec{\varepsilon}^{\,l(+)}\cdot\vec{r}_{i1}) & \text{if} s=+1 \\ +\tfrac{e}{\hbar}\textstyle\sum_{l\in L_{i1}} E_0^l \Re\mathfrak{e}(\vec{\varepsilon}^{\,l(+)}\cdot\vec{r}_{i1}) & \text{if} s=-1 \end{cases} \end{aligned} \tag{C.1}$$

which is to say that the only b^ν that can be non-zero are those for $\nu(i,1,s)$ with $2 \le i \le N_e$.

C.2 Evolution Operator

We will now calculate the components $A_{\mu\nu}$ of the evolution operator (sometimes called superoperator) using the new indices

$$\dot{\tilde{\rho}}_{\mu(i,j,s)} = A_{\mu(i,j,s)\nu(a,b,r)}\tilde{\rho}_{\nu(a,b,r)} = b_{\nu(i,1,s)}.$$

Considering that the part operator satisfies

$$\mathfrak{Pa}(s,iz) = \begin{cases} \mathfrak{Re}(iz) & s=1 \\ \mathfrak{Im}(iz) & s=-1 \end{cases} = \begin{cases} -\mathfrak{Im}(z) & s=1 \\ +\mathfrak{Re}(z) & s=-1 \end{cases} = -s\mathfrak{Pa}(-s,z),$$

the real and imaginary parts of the equations

$$\begin{aligned}
\mathfrak{Pa}(s,\dot{\tilde{\rho}}_{ij}) = \mathfrak{Pa}\Bigg(s, \frac{ie}{\hbar}\Bigg[&\sum_k \sum_{l\in L_{ik}} E_0^l \left(\underset{k>j}{\delta}\left(\underset{k>i}{\delta}\vec{\varepsilon}^{\,l(-)}\cdot\vec{r}_{ik} + \underset{k<i}{\delta}\vec{\varepsilon}^{\,l(+)}\cdot\vec{r}_{ik}\right)\tilde{\rho}_{kj} + \underset{k<j}{\delta}(\vec{\varepsilon}^{\,l(+)}\cdot\vec{r}_{ik})\tilde{\rho}^*_{jk}\right) \\
&- \sum_k \sum_{l\in L_{kj}} E_0^l \left(\underset{k<i}{\delta}\left(\underset{k<j}{\delta}\vec{\varepsilon}^{\,l(-)}\cdot\vec{r}_{kj} + \underset{k>j}{\delta}\vec{\varepsilon}^{\,l(+)}\cdot\vec{r}_{kj}\right)\tilde{\rho}_{ik} + \underset{k>i}{\delta}(\vec{\varepsilon}^{\,l(+)}\cdot\vec{r}_{kj})\tilde{\rho}^*_{ki}\right) \\
&+ \sum_{l\in L_{ij}} E_0^l(\vec{\varepsilon}^{\,l(+)}\cdot\vec{r}_{ij})(\rho_{jj}-\rho_{ii})\Bigg]\Bigg) \\
&+ \Theta_{ij}\mathfrak{Pa}(s,i\tilde{\rho}_{ij}) - \frac{\gamma_{ij}}{2}\mathfrak{Pa}(s,\tilde{\rho}_{ij}) \\
= -\frac{se}{\hbar}\Bigg[&\sum_k \sum_{l\in L_{ik}} E_0^l\mathfrak{Pa}\left(-s, \underset{k>j}{\delta}\left(\underset{k>i}{\delta}\vec{\varepsilon}^{\,l(-)}\cdot\vec{r}_{ik} + \underset{k<i}{\delta}\vec{\varepsilon}^{\,l(+)}\cdot\vec{r}_{ik}\right)\tilde{\rho}_{kj} + \underset{k<j}{\delta}(\vec{\varepsilon}^{\,l(+)}\cdot\vec{r}_{ik})\tilde{\rho}^*_{jk}\right) \\
&- \sum_k \sum_{l\in L_{kj}} E_0^l\mathfrak{Pa}\left(-s, \underset{k<i}{\delta}\left(\underset{k<j}{\delta}\vec{\varepsilon}^{\,l(-)}\cdot\vec{r}_{kj} + \underset{k>j}{\delta}\vec{\varepsilon}^{\,l(+)}\cdot\vec{r}_{kj}\right)\tilde{\rho}_{ik} + \underset{k>i}{\delta}(\vec{\varepsilon}^{\,l(+)}\cdot\vec{r}_{kj})\tilde{\rho}^*_{ki}\right) \\
&+ \sum_{l\in L_{ij}} E_0^l\mathfrak{Pa}(-s,\vec{\varepsilon}^{\,l(+)}\cdot\vec{r}_{ij})(\rho_{jj}-\rho_{ii})\Bigg] \\
&- s\Theta_{ij}\mathfrak{Pa}(-s,\tilde{\rho}_{ij}) - \frac{\gamma_{ij}}{2}\mathfrak{Pa}(s,\tilde{\rho}_{ij}) \\
= s\frac{e}{\hbar}\Bigg[&\sum_k \sum_{l\in L_{kj}} E_0^l\mathfrak{Pa}\left(-s, \underset{k<ik<j}{\delta\delta}\vec{\varepsilon}^{\,l(-)}\cdot\vec{r}_{kj}\tilde{\rho}_{ik} + \underset{k<ik>j}{\delta\delta}\vec{\varepsilon}^{\,l(+)}\cdot\vec{r}_{kj}\tilde{\rho}_{ik} + \underset{k>i}{\delta}(\vec{\varepsilon}^{\,l(+)}\cdot\vec{r}_{kj})\tilde{\rho}^*_{ki}\right) \\
&- \sum_{l\in L_{ik}} E_0^l\mathfrak{Pa}\left(-s, \underset{k>jk>i}{\delta\delta}\vec{\varepsilon}^{\,l(-)}\cdot\vec{r}_{ik}\tilde{\rho}_{kj} + \underset{k>jk<i}{\delta\delta}\vec{\varepsilon}^{\,l(+)}\cdot\vec{r}_{ik}\tilde{\rho}_{kj} + \underset{k<j}{\delta}(\vec{\varepsilon}^{\,l(+)}\cdot\vec{r}_{ik})\tilde{\rho}^*_{jk}\right) \\
&+ \sum_{l\in L_{ij}} E_0^l\mathfrak{Pa}(-s,\vec{\varepsilon}^{\,l(+)}\cdot\vec{r}_{ij})(\rho_{ii}-\rho_{jj})\Bigg] \\
&- s\Theta_{ij}\mathfrak{Pa}(-s,\tilde{\rho}_{ij}) - \frac{\gamma_{ij}}{2}\mathfrak{Pa}(s,\tilde{\rho}_{ij})
\end{aligned}$$

And if we write this in the new notation we get

$$\begin{aligned}
\mathfrak{Pa}(s,\dot{\tilde{\rho}}_{ij}) = s\frac{e}{\hbar}\Bigg[\sum_k \sum_{l\in L_{kj}} E_0^l \Bigg(& \underset{k<i}{\delta}\underset{k<j}{\delta}\mathfrak{Pa}(-s,(\vec{\varepsilon}^{\,l(-)}\cdot\vec{r}_{kj})(\tilde{\rho}_{\nu(i,k,1)}+i\tilde{\rho}_{\nu(i,k,-1)})) \\
& + \underset{k<i}{\delta}\underset{k>j}{\delta}\mathfrak{Pa}(-s,(\vec{\varepsilon}^{\,l(+)}\cdot\vec{r}_{kj})(\tilde{\rho}_{\nu(i,k,1)}+i\tilde{\rho}_{\nu(i,k,-1)})) \\
& + \underset{k>i}{\delta}\mathfrak{Pa}(-s,(\vec{\varepsilon}^{\,l(+)}\cdot\vec{r}_{kj})(\tilde{\rho}_{\nu(k,i,1)}-i\tilde{\rho}_{\nu(k,i,-1)}))\Bigg) \\
- \sum_{l\in L_{ik}} E_0^l \Bigg(& \underset{k>j}{\delta}\underset{k>i}{\delta}\mathfrak{Pa}(-s,(\vec{\varepsilon}^{\,l(-)}\cdot\vec{r}_{ik})(\tilde{\rho}_{\nu(k,j,1)}+i\tilde{\rho}_{\nu(k,j,-1)})) \\
& + \underset{k>j}{\delta}\underset{k<i}{\delta}\mathfrak{Pa}(-s,(\vec{\varepsilon}^{\,l(+)}\cdot\vec{r}_{ik})(\tilde{\rho}_{\nu(k,j,1)}+i\tilde{\rho}_{\nu(k,j,-1)})) \\
& + \underset{k<j}{\delta}\mathfrak{Pa}(-s,(\vec{\varepsilon}^{\,l(+)}\cdot\vec{r}_{ik})(\tilde{\rho}_{\nu(j,k,1)}-i\tilde{\rho}_{\nu(j,k,-1)}))\Bigg) \\
+ \sum_{l\in L_{ij}} & E_0^l\mathfrak{Pa}(-s,\vec{\varepsilon}^{\,l(+)}\cdot\vec{r}_{ij})(\rho_{\nu(i,i)}-\rho_{\nu(j,j)})\Bigg] \\
- s\Theta_{ij}\mathfrak{Pa}(-s,(\tilde{\rho}_{\nu(i,j,1)}+i\tilde{\rho}_{\nu(i,j,-1)})) & - \frac{\gamma_{ij}}{2}\mathfrak{Pa}(s,(\tilde{\rho}_{\nu(i,j,1)}+i\tilde{\rho}_{\nu(i,j,-1)}))
\end{aligned}$$

and considering that

$$\mathfrak{Pa}(-s,iz) = \begin{cases} \Re\mathfrak{e}(iz) & s=-1 \\ \Im\mathfrak{m}(iz) & s=+1 \end{cases} = \begin{cases} \Re\mathfrak{e}(z) & s=+1 \\ -\Im\mathfrak{m}(z) & s=-1 \end{cases} = s\mathfrak{Pa}(s,z)$$

we finally get

$$\begin{aligned}
\dot{\tilde{\rho}}_{\mu(i,j,s)} = \tfrac{se}{\hbar}\Big[\textstyle\sum_k \sum_{l\in L_{kj}} E_0^l \Big(& \underset{k<i}{\delta}\underset{k<j}{\delta}(\mathfrak{Pa}(-s,\vec{\varepsilon}^{\,l(-)}\cdot\vec{r}_{kj})\tilde{\rho}_{\nu(i,k,1)} + s\mathfrak{Pa}(s,\vec{\varepsilon}^{\,l(-)}\cdot\vec{r}_{kj})\tilde{\rho}_{\nu(i,k,-1)}) \\
& + \underset{k<i}{\delta}\underset{k>j}{\delta}(\mathfrak{Pa}(-s,\vec{\varepsilon}^{\,l(+)}\cdot\vec{r}_{kj})\tilde{\rho}_{\nu(i,k,1)} + s\mathfrak{Pa}(s,\vec{\varepsilon}^{\,l(+)}\cdot\vec{r}_{kj})\tilde{\rho}_{\nu(i,k,-1)}) \\
& + \underset{k>i}{\delta}\quad(\mathfrak{Pa}(-s,\vec{\varepsilon}^{\,l(+)}\cdot\vec{r}_{kj})\tilde{\rho}_{\nu(k,i,1)} - s\mathfrak{Pa}(s,\vec{\varepsilon}^{\,l(+)}\cdot\vec{r}_{kj})\tilde{\rho}_{\nu(k,i,-1)})\Big) \\
- \textstyle\sum_{l\in L_{ik}} E_0^l \Big(& \underset{k>j}{\delta}\underset{k>i}{\delta}(\mathfrak{Pa}(-s,\vec{\varepsilon}^{\,l(-)}\cdot\vec{r}_{ik})\tilde{\rho}_{\nu(k,j,1)} + s\mathfrak{Pa}(s,\vec{\varepsilon}^{\,l(-)}\cdot\vec{r}_{ik})\tilde{\rho}_{\nu(k,j,-1)}) \\
& + \underset{k>j}{\delta}\underset{k<i}{\delta}(\mathfrak{Pa}(-s,\vec{\varepsilon}^{\,l(+)}\cdot\vec{r}_{ik})\tilde{\rho}_{\nu(k,j,1)} + s\mathfrak{Pa}(s,\vec{\varepsilon}^{\,l(+)}\cdot\vec{r}_{ik})\tilde{\rho}_{\nu(k,j,-1)}) \\
& + \underset{k<j}{\delta}\quad(\mathfrak{Pa}(-s,\vec{\varepsilon}^{\,l(+)}\cdot\vec{r}_{ik})\tilde{\rho}_{\nu(j,k,1)} - s\mathfrak{Pa}(s,\vec{\varepsilon}^{\,l(+)}\cdot\vec{r}_{ik})\tilde{\rho}_{\nu(j,k,-1)})\Big) \\
+ \textstyle\sum_{l\in L_{ij}} & E_0^l\mathfrak{Pa}(-s,\vec{\varepsilon}^{\,l(+)}\cdot\vec{r}_{ij})(\rho_{\nu(i,i)}-\rho_{\nu(j,j)})\Big] \\
-s\Theta_{ij}\tilde{\rho}_{\nu(i,j,-s)} - \tfrac{\gamma_{ij}}{2}\tilde{\rho}_{\nu(i,j,s)} & \\
+\textstyle\sum_{a>b}\gamma_{ab}\Big[(\delta_{ib}\delta_{bj}-\delta_{ia}\delta_{aj})\rho_{\nu(a,a,s)} - \tfrac{1}{2}\Big[\sum_{d\neq a}\delta_{ia}\delta_{dj}\tilde{\rho}_{\nu(a,d,s)} + \sum_{c\neq a}\delta_{ic}\delta_{aj}\tilde{\rho}_{(c,a,s)}\Big]\Big] & .
\end{aligned} \tag{C.2}$$

An explicit expression for $A_{\mu\nu}$ might be obtained from here as was done for the independent vector, but it is much easier to determine for each $\mu(i,j,s)$ with $i>j$ which are the $\nu(a,b,s)$ that satisfy the necessary conditions indicated by the δ symbols and add the corresponding elements to

$A_{\mu\nu}$.

One has to consider that this expression is valid for any $\dot{\tilde{\rho}}_{\mu(i,j,s)}$ that does not depend on ρ_{11}. In the case where $j = 1$ the second term in the seventh row of 2.10 is proportional to $\rho_{11} = 1 - \sum_{n=2}^{N_e} \rho_{\nu(n,n)}$ and that term must be replaced by

$$\dot{\tilde{\rho}}_{\mu(i,1,s)} = s\frac{e}{\hbar} \sum_{l \in L_{i1}} E_0^l \mathfrak{Pa}[-s, \vec{\varepsilon}^{\,\mathbf{l}(+)} \cdot \vec{r}_{i1}] \left(\sum_{n=2}^{N_e} \rho_{\nu(n,n)} \right).$$

That is, one must add $s\frac{e}{\hbar} \sum_{l \in L_{i1}} E_0^l \mathfrak{Pa}[-s, \vec{\varepsilon}^{\,\mathbf{l}(+)} \cdot \vec{r}_{i1}]$ in $A_{\mu(i,1,s)\nu(n,n)}$ for each population $\rho_{\nu(n,n)}$ and each $2 \leq i \leq N_e$.

Appendix D

Reduction of the dipole operator

The Wigner-Eckhart theorem states that [17]

$$\langle N_i L_i J_i I F_i M_i | T^1_p(\widehat{\vec{r}}) | N_j L_j J_j I F_j M_j \rangle \equiv (-1)^{F_i - M_i} \begin{pmatrix} F_i & 1 & F_j \\ -M_i & p & M_j \end{pmatrix} (N_i L_i J_i I F_i || T^1(\widehat{\vec{r}}) || N_j L_j J_j I F_j) \tag{D.1}$$

where $(F_i||T^1(\widehat{\vec{r}})||F_j) \equiv (N_i L_i S J_i I F_i||T^1(\widehat{\vec{r}})||N_j L_j S J_j I F_j)$ is the reduced matrix element, and $\begin{pmatrix} F_i & 1 & F_j \\ -M_i & p & M_j \end{pmatrix}$ is a Wigner 3-j symbol defined [17] as

$$\begin{pmatrix} j_1 & j_2 & j_3 \\ m_1 & m_2 & m_3 \end{pmatrix} = (-1)^{j_1 - j_2 - m_3} (2j_2+1)^{-1/2} (j_1 m_1 j_2 m_2 | j_1 j_2 j_3 - m_3)$$

where $(j_1 m_1 j_2 m_2 | j_1 j_2 j_3 - m_3)$ is a Clebsch-Gordan coefficient, defined as the coefficients of an eigenstate $|\gamma j_1 j_2 j m\rangle$ of total angular momentum $\overrightarrow{\hat{j}} = \overrightarrow{\hat{j}}_1 + \overrightarrow{\hat{j}}_2$ in the decoupled basis

$$|\gamma j_1 j_2 j m\rangle = \sum_{m_1 m_2} (j_1 m_1 j_2 m_2 | j_1 j_2 j m) |\gamma j_1 m_1 j_2 m_2\rangle.$$

These may be computed in general through the formula [17]

$$\begin{aligned}(j_1 m_1 j_2 m_2 | j_1 j_2 j m) = \delta_{m_1+m_2,m} &\sqrt{\frac{(2j+1)(j_1+j_2-j)!(j_1-j_2+j)!(-j_1+j_2+j)!}{(j_1+j_2+j+1)!}} \\ &\times \sqrt{(j_1+m_1)!(j_1-m_1)!(j_2+m_2)!(j_2-m_2)!(j+m)!(j-m)!} \\ &\times \sum_z (-1)^z \frac{1}{(j_1+j_2-j-z)!(j_1-m_1-z)!(j_2+m_2-z)!(j-j_2+m_1+z)!(j-j_1-m_2+z)!}\end{aligned}$$

where z runs over all values that correspond to positive integer values of the arguments of the factorials.

In general if a spherical tensor $T^k(A)$ of rank k acts only on part 1 o in the coupled scheme, it's reduced matrix element satisfies [17]

$$(\gamma j_1 j_2 j||T^k(A)||\gamma' j_1' j_2' j') = (-1)^{j_1+j_2'+j'+k}\sqrt{(2j_2'+1)(2j_2+1)}\left\{\begin{array}{ccc} j_1 & j & j_2' \\ j' & j_1' & k \end{array}\right\}(\gamma j_1||T^k(A)||\gamma' j_1'),$$

where $\left\{\begin{array}{ccc} j_1 & j & j_2' \\ j' & j_1' & k \end{array}\right\}$ is a 6-j Wigner symbol, defined [17] as

$$\begin{aligned}\left\{\begin{array}{ccc} j_1 & j_2 & j_{12} \\ j_3 & J & j_{23} \end{array}\right\} &= (-1)^{j_1+j_2+j_3+J}[(2j_{12}+1)(2j_{23}+1)]^{-1/2} \\ &\times \sum_{m_1 m_2}(j_1 m_1 j_2 m_2|j_1 j_2 j_{12} m_1+m_2) \\ &\times (j_{12} m_1+m_2 j_3 M-m_1-m_2|j_{12} j_3 J M) \\ &\times (j_2 m_2 j_3 M-m_1-m_3|j_2 j_3 j_{23} M-m_1) \\ &\times (j_1 m_1 j_{23} M-m_1|j_1 j_{23} J M)\end{aligned}$$

Since the operator $\overrightarrow{\hat{r}}$ acts only on the L and J parts of the states, but not on the S or I parts, it is possible to decouple the S and I parts in the reduced matrix element. Therefore, our reduced matrix element is

$$\begin{aligned}(N_i L_i J_i I F_i||T^1(\widehat{\vec{r}})||N_j L_j J_j I F_j) &= (-1)^{J_i+I+F_j+1}\sqrt{(2F_j+1)(2F_i+1)}\left\{\begin{array}{ccc} J_i & F_i & I \\ F_j & J_j & 1 \end{array}\right\} \\ &\times (N_i L_i J_i||T^1(\widehat{\vec{r}})||N_j L_j J_j),\end{aligned}$$

and the matrix elements are

$$\begin{aligned}\langle N_i L_i J_i F_i M_i|T_p^1(\widehat{\vec{r}})|N_j L_j J_j F_j M_j\rangle &= (-1)^{F_i-M_i+J_i+I+F_j+1}\sqrt{(2F_j+1)(2F_i+1)} \\ &\times \left(\begin{array}{ccc} F_i & 1 & F_j \\ -M_i & p & M_j \end{array}\right)\left\{\begin{array}{ccc} J_i & F_i & I \\ F_j & J_j & 1 \end{array}\right\}(N_i L_i J_i||T^1(\widehat{\vec{r}})||N_j L_j J_j)\end{aligned} \tag{D.2}$$

The reduced matrix elements are not symmetric under exchange of their arguments, but rather follow the symmetry relation [17]

$$(N_i L_i J_i||T^1(\widehat{\vec{r}})||N_j L_j J_j) = (-1)^{J_i-J_j}(N_j L_j J_j||T^1(\widehat{\vec{r}})||N_i L_i J_i)^*, \tag{D.3}$$

although they will be taken to be real in this thesis.

Similarly, the L and S parts can be decoupled as

$$\begin{aligned}\langle N_i L_i J_i F_i M_i | T^1_p(\widehat{\vec{r}}) | N_j L_j J_j F_j M_j \rangle &= 2(-1)^{F_i - M_i + J_i + I + F_j + L_i + S_j + J_j + 2} \sqrt{(2F_j+1)(2F_i+1)} \\ &\times \begin{pmatrix} F_i & 1 & F_j \\ -M_i & p & M_j \end{pmatrix} \begin{Bmatrix} J_i & F_i & I \\ F_j & J_j & 1 \end{Bmatrix} \begin{Bmatrix} L_i & J_i & 1/2 \\ J_j & L_j & 1 \end{Bmatrix} \\ &\times (N_i L_i || T^1(\widehat{\vec{r}}) || N_j L_j).\end{aligned}$$

And these reduced matrix elements follow the symmetry relation

$$(N_i L_i || T^1(\widehat{\vec{r}}) || N_j L_j) = (-1)^{L_i - L_j} (N_j L_j || T^1(\widehat{\vec{r}}) || N_i L_i)^*.$$

Appendix E

Calculation of Reduced Matrix Elements

The reduced matrix elements might be calculated from first principles, but that is outside the scope of this thesis. Instead we will derive an expression to calculate them from the decay frequencies of the states. These decay frequencies can be found in the literature, in particular in the references in table 3.1.

The Einstein A_{ij} coefficients connecting magnetic states are the same as the spontaneous decay frequencies γ_{ij} mentioned in chapter 2, and they are related to the matrix elements of $\overrightarrow{r}$ through [47]

$$\gamma_{ij} = A_{ij} = \frac{\omega_{ij}^3 e^2}{3\pi\hbar c^3 \varepsilon_0} \sum_p \left| \langle N_i L_i J_i F_i M_i | T_p^1(\widehat{r}) | N_j L_j J_j F_j M_j \rangle \right|^2 . \tag{E.1}$$

The reduced matrix elements satisfy [17]

$$\sum_{mm'} \sum_p \left| \langle \gamma j m | T_p^1(\vec{r}) | \gamma' j' m' \rangle \right|^2 = (j \| T_p^1(\widehat{r}) \| j'),$$

therefore

$$\sum_{M_i M_j} \gamma_{ij} = \frac{\omega_{ij}^3 e^2}{3\pi\hbar c^3 \varepsilon_0} \sum_{M_i M_j} \sum_p \left| \langle N_i L_i J_i F_i M_i | T_p^1(\widehat{\vec{r}}) | N_j L_j J_j F_j M_j \rangle \right|^2$$

$$= \frac{\omega_{ij}^3 e^2}{3\pi\hbar c^3 \varepsilon_0} |(N_i L_i J_i I F_i || T^1(\widehat{\vec{r}}) || N_j L_j J_j I F_j)|^2$$

$$= \frac{\omega_{ij}^3 e^2}{3\pi\hbar c^3 \varepsilon_0} (2F_j + 1)(2F_i + 1) \left\{ \begin{array}{ccc} J_i & F_i & I \\ F_j & J_j & 1 \end{array} \right\}^2 |(N_i L_i J_i || T^1(\widehat{\vec{r}}) || N_j L_j J_j)|^2$$

$$\sum_{M_j} \gamma_{ij} = \frac{\omega_{ij}^3 e^2}{3\pi\hbar c^3 \varepsilon_0} (2F_j + 1) \left\{ \begin{array}{ccc} J_i & F_i & I \\ F_j & J_j & 1 \end{array} \right\}^2 |(N_i L_i J_i || T^1(\widehat{\vec{r}}) || N_j L_j J_j)|^2$$

$$\sum_{F_j M_j} \gamma_{ij} = \frac{\omega_{ij}^3 e^2}{3\pi\hbar c^3 \varepsilon_0} |(N_i L_i J_i || T^1(\widehat{\vec{r}}) || N_j L_j J_j)|^2 \sum_{F_j} (2F_j + 1) \left\{ \begin{array}{ccc} J_i & F_i & I \\ F_j & J_j & 1 \end{array} \right\}^2 .$$

But 6j symbols satisfy [17]

$$(2j'' + 1) \sum_j (2j + 1) \left\{ \begin{array}{ccc} j' & j_1 & j_2 \\ j & j_3 & j_4 \end{array} \right\} \left\{ \begin{array}{ccc} j'' & j_1 & j_2 \\ j & j_3 & j_4 \end{array} \right\} = \delta_{j' j''}.$$

Therefore

$$\sum_{F_j} (2F_j + 1) \left\{ \begin{array}{ccc} J_i & F_i & I \\ F_j & J_j & 1 \end{array} \right\}^2 = \frac{1}{2J_i + 1},$$

from which it follows

$$\sum_{F_j M_j} \gamma_{ij} = \frac{\omega_{ij}^3 e^2}{3\pi\hbar c^3 \varepsilon_0} \frac{1}{2J_i + 1} |(N_i L_i J_i || T^1(\widehat{\vec{r}}) || N_j L_j J_j)|^2.$$

It is important to notice that this sum is not over all F_j or all M_j but only over those that are associated with the reduced matrix element $(N_i L_i J_i || T^1(\widehat{\vec{r}}) || N_j L_j J_j)$. Therefore, this sum is not the total decay frequency Γ_i of a state $|i\rangle$ to any allowed lower transition, but rather, the total decay frequency Γ_{ij} to the fine multiplet $|N_j L_j J_j\rangle$. In other words

$$\Gamma_{ij} = \frac{\omega_{ij}^3 e^2}{3\pi\hbar c^3 \varepsilon_0} \frac{1}{2J_i + 1} |(N_i L_i J_i || T^1(\widehat{\vec{r}}) || N_j L_j J_j)|^2, \tag{E.2}$$

which allows us to obtain the reduced matrix element as

$$(N_i L_i J_i || T^1(\overrightarrow{\hat{r}}) || N_j L_j J_j) = \left(\frac{3\pi\hbar c^3 \varepsilon_0}{\omega_{ij}^3 e^2} (2J_i + 1) \Gamma_{ij} \right)^{1/2}. \tag{E.3}$$

Appendix F

Electric-dipole Selection Rules

As seen in appendix D, the matrix elements of the dipole operator can be decoupled as

$$\begin{aligned}\langle N_i L_i J_i F_i M_i | T^1_p(\widehat{\vec{r}}) | N_j L_j J_j F_j M_j \rangle = 2(-1)^{F_i - M_i + J_i + I + F_j + L_i + S_j + J_j + 2} \sqrt{(2F_j+1)(2F_i+1)} \\ \times \begin{pmatrix} F_i & 1 & F_j \\ -M_i & p & M_j \end{pmatrix} \begin{Bmatrix} J_i & F_i & I \\ F_j & J_j & 1 \end{Bmatrix} \begin{Bmatrix} L_i & J_i & 1/2 \\ J_j & L_j & 1 \end{Bmatrix} \\ \times (N_i L_i || T^1(\widehat{\vec{r}}) || N_j L_j)\end{aligned}$$

A condition for the 3-j symbol to be non-zero is that the upper row satisfies the triangle condition $|F_i - F_j| \leq 1 \leq F_i + F_j$. The first of these inequalities implies the selection rule $\Delta M = 0, \pm 1$. Since F are integer numbers, the second inequality gives the selection rule that if $F_i = 0$ then $F_j \geq 1$. Also, $|M_i| \leq F_i$ and $|M_j| \leq F_j$.

Another condition for the 3-j symbol to be non-zero is that the lower row satisfies $-M_i + p + M_j = 0$, meaning that light polarization p can only induce transitions satisfying $p = M_i - M_j$.

If all the arguments in the lower row of the 3-j symbol are zero, then it is zero unless the sum of the arguments of the upper row is an even number. Therefore $F_i + F_j + 1$ must be even, which in turn implies that $\Delta F = \pm 1$. This argument can be summarized by the rule: if $M_i = M_j = 0$ then $\Delta F = \pm 1$.

The 6-j symbols are unchanged if the upper and lower arguments of two columns are exchanged. If we do this for the second and third column of the first 6-j symbol we get $\begin{Bmatrix} J_i & J_j & 1 \\ F_j & F_i & I \end{Bmatrix}$. The 6-j symbol is non-zero only if the upper row satisfies the triangle condition $|J_i - J_j| \leq 1 \leq J_i + J_j$. The first inequality gives the selection rule $\Delta J = 0, \pm 1$, and the second inequality is always satisfied because J is always semi-integer.

Exchanging upper and lower arguments in the second 6-j symbol we get $\begin{Bmatrix} L_i & L_j & 1 \\ J_j & J_i & 1/2 \end{Bmatrix}$,

from which the selection rule $\Delta L = 0, \pm 1$ can be similarly deduced. Since L takes integer values, the selection rule: if $L_i = 0$ then $L_j \geq 1$ is implied.

Another condition that must be satisfied is that the parity of the wave functions ϕ_i, ϕ_j of states $|i\rangle, |j\rangle$ must be opposite. This is because the operator $\widehat{\vec{r}}$ is odd, and if the parity of the wavefunctions is the same, the matrix element $\langle i|\widehat{\vec{r}}|j\rangle = \int \phi_i^* \widehat{\vec{r}} \phi_j dV$ is zero. Since the electrons in the closed shells of alkali atoms have zero contribution to the total angular momentum, it follows that the ϕ_i are linear combinations of the form

$$\phi_i(r, \theta, \varphi) = \sum_m c_m Y_{L_i}^m(\theta, \varphi),$$

where $Y_{L_i}^m(\theta, \varphi)$ is a spherical harmonic. In other words there will be no contribution of wavefunctions with $l \neq L_i$ from electrons other than the valence electron. The parity of the spherical harmonics is $\pi(Y_l^m) = (-1)^l$, and hence $\pi(\phi_i) = (-1)^{L_i} = (-1)^{-L_i}$. The matrix elements are non-zero only if

$$\pi(\phi_i \widehat{\vec{r}} \phi_j) = 1 = \pi(\phi_i)\pi(\widehat{\vec{r}})\pi(\phi_j) = (-1)^{-L_i+1+L_j},$$

which implies $\Delta L = \pm 1$. The electric dipole selection rules are summarized in table F.1.

$\Delta L = \pm 1$
$\Delta J = 0, \pm 1$
$\Delta F = 0, \pm 1$
if $F_i = 0$ then $F_j \geq 1$
$\lvert M_i \rvert \leq F_i$ & $\lvert M_j \rvert \leq F_j$
if $M_i = M_j = 0$ then $\Delta F = \pm 1$
$p = M_i - M_j$

Table F.1: Electric dipole selection rules.

Notice that these are all necessary, but not sufficient conditions.

Bibliography

[1] Alexander M. Akulshin, Russell J. McLean, Andrei I. Sidorov, and Peter Hannaford. Coherent and collimated blue light generated by four-wave mixing in rb vapour. *Opt. Express*, 17(25):22861–22870, Dec 2009.

[2] E. Anderson, Z. Bai, J. Dongarra, A. Greenbaum, A. McKenney, J. Du Croz, S. Hammerling, J. Demmel, C. Bischof, and D. Sorensen. Lapack: A portable linear algebra library for high-performance computers. In *Proceedings of the 1990 ACM/IEEE Conference on Supercomputing*, Supercomputing '90, pages 2–11, Los Alamitos, CA, USA, 1990. IEEE Computer Society Press.

[3] E. Arimondo, M. Inguscio, and P. Violino. Experimental determinations of the hyperfine structure in the alkali atoms. *Rev. Mod. Phys.*, 49:31–75, Jan 1977.

[4] S. H. Autler and C. H. Townes. Stark effect in rapidly varying fields. *Phys. Rev.*, 100:703–722, Oct 1955.

[5] R C Barret. Theory of the hyperfine structure of free atoms. *Physics Bulletin*, 24(4):237, 1973.

[6] Hans Albrecht Bethe and Edwin E Salpeter. *Quantum mechanics of one- and two-electron atoms*. Plenum, New York, NY, 1977. Based on an article publ. in Handbuch der Physik Bd.35, 1957.

[7] Karl Blum. *Density matrix theory and applications; 3rd ed.* Springer Series on Atomic Optical and Plasma Physics. Springer, Berlin, 2012.

[8] K.-J. Boller, A. Imamoğlu, and S. E. Harris. Observation of electromagnetically induced transparency. *Phys. Rev. Lett.*, 66:2593–2596, May 1991.

[9] G. Boole. *A Treatise on the Calculus of Finite Differences*. Macmillan, 1860.

[10] M. Folk G. Goucher Brown, S. A and R. Rew. "software for portable scientific data management". *Computers in Physics*, 7:304–308, May-Jun 1993.

[11] G Camy, B Decomps, J-L Gardissat, and C J Bordé. Frequency stabilization of argon lasers at 582.49 thz using saturated absorption in 127 i 2. *Metrologia*, 13(3):145, 1977.

[12] F. S. Cataliotti, C. Fort, T. W. Hänsch, M. Inguscio, and M. Prevedelli. Electromagnetically induced transparency in cold free atoms: Test of a sum rule for nonlinear optics. *Phys. Rev. A*, 56:2221–2224, Sep 1997.

[13] F S Cataliotti, C Fort, M Prevedelli, and M Inguscio. Full resolution of the autler-townes zeeman multiplet for cold cesium atoms in three-level ∧-type configuration. *Canadian Journal of Physics*, 75(11):767–773, 1997.

[14] Steven Chu, J. E. Bjorkholm, A. Ashkin, and A. Cable. Experimental observation of optically trapped atoms. *Phys. Rev. Lett.*, 57:314–317, Jul 1986.

[15] Steven Chu, L. Hollberg, J. E. Bjorkholm, Alex Cable, and A. Ashkin. Three-dimensional viscous confinement and cooling of atoms by resonance radiation pressure. *Phys. Rev. Lett.*, 55:48–51, Jul 1985.

[16] Alan Corney. *Atomic and Laser Spectroscopy*. Oxford University Press, first edition, 1977.

[17] A R Edmonds. *Angular momentum in quantum mechanics*. Investigations in physics, 4.; Investigations in physics, no. 4. Princeton, N.J., Princeton University Press, 1957.

[18] A. Einstein. Über die von der molekularkinetischen theorie der wärme geforderte bewegung von in ruhenden flüssigkeiten suspendierten teilchen. *Annalen der Physik*, 322(8):549–560, 1905.

[19] Richard M. Stallman et al. Gnu compiler collection. 2013.

[20] Michael Fleischhauer, Atac Imamoglu, and Jonathan P. Marangos. Electromagnetically induced transparency: Optics in coherent media. *Rev. Mod. Phys.*, 77:633–673, Jul 2005.

[21] Christopher J. Foot. *Atomic Physics*. Oxford University Press, first edition, 2005.

[22] Joseph Fraunhofer. "bestimmung des brechungs- und des farben-zerstreuungs - vermögens verschiedener glasarten, in bezug auf die vervollkommnung achromatischer fernröhre" (determination of the refractive and color-dispersing power of different types of glass, in relation to the improvement of achromatic telescopes. (Bd. 5), 1817.

[23] David J. Fulton, Sara Shepherd, Richard R. Moseley, Bruce D. Sinclair, and Malcolm H. Dunn. Continuous-wave electromagnetically induced transparency: A comparison of v, Λ, and cascade systems. *Phys. Rev. A*, 52:2302–2311, Sep 1995.

[24] Julio Gea-Banacloche, Yong-qing Li, Shao-zheng Jin, and Min Xiao. Electromagnetically induced transparency in ladder-type inhomogeneously broadened media: Theory and experiment. *Phys. Rev. A*, 51:576–584, Jan 1995.

[25] Vladislav Gerginov, Andrei Derevianko, and Carol E. Tanner. Observation of the nuclear magnetic octupole moment of ^{133}Cs. *Phys. Rev. Lett.*, 91:072501, Aug 2003.

[26] E. Gomez, F. Baumer, A. D. Lange, G. D. Sprouse, and L. A. Orozco. Lifetime measurement of the 6*s* level of rubidium. *Phys. Rev. A*, 72:012502, Jul 2005.

[27] Ramiz Hamid, Mustafa Çetintaş, and Mehmet Çelik. Polarization resonance on s–d two-photon transition of rb atoms. *Optics Communications*, 224(4–6):247 – 253, 2003.

[28] T. W. Hänsch, M. D. Levenson, and A. L. Schawlow. Complete hyperfine structure of a molecular iodine line. *Phys. Rev. Lett.*, 26:946–949, Apr 1971.

[29] S. E. Harris, J. E. Field, and A. Imamoğlu. Nonlinear optical processes using electromagnetically induced transparency. *Phys. Rev. Lett.*, 64:1107–1110, Mar 1990.

[30] E. Hecht. *Optics*. Pearson education. Addison-Wesley, 2002.

[31] Santiago Hernández Gómez. Sistema para producir estados de rydberg en rubidio atómico a temperatura ambiente con tres fotones, 2014.

[32] Ingolf Volker Hertel and Claus-Peter Schulz. *Atoms, Molecules and Optical Physics 1*. Springer Berlin Heidelberg, 2015.

[33] R. Jáuregui. Control of atomic transition rates via laser-light shaping. *Phys. Rev. A*, 91:043842, Apr 2015.

[34] Eric Jones, Travis Oliphant, Pearu Peterson, et al. SciPy: Open source scientific tools for Python, 2001–. [Online; accessed 2016-03-02].

[35] Ravi Kumar, Vandna Gokhroo, Kieran Deasy, and Síle Nic Chormaic. Autler-townes splitting via frequency up-conversion at ultralow-power levels in cold ^{87}Rb atoms using an optical nanofiber. *Phys. Rev. A*, 91:053842, May 2015.

[36] Leonti Labzowsky, Igor Goidenko, and Pekka Pyykkö. Estimates of the bound-state {QED} contributions to the g-factor of valence ns electrons in alkali metal atoms. *Physics Letters A*, 258(1):31 – 37, 1999.

[37] Ira N. Levine. *Quantum chemistry /*. Prentice Hall,, Englewood Cliffs, N.J. :, 4th ed. edition, c1991.

[38] Jongseok Lim, Han-gyeol Lee, and Jaewook Ahn. Review of cold rydberg atoms and their applications. *Journal of the Korean Physical Society*, 63(4):867–876, 2013.

[39] Oscar López-Hernández, Santiago Hernández-Gómez, Francisco Sebastián Ponciano-Ojeda, Cristian Mojica-Casique, Ricardo Colín-Rodríguez, Jesús Flores-Mijangos, Daniel Sahagún, Fernando Ramírez-Martínez, and José Jiménez-Mier. A laser spectroscopy system with combined absorption, polarization rotation and fluorescence detection to study two photon transitions in atomic rubidium. *Journal of Applied Research and Technology*, 13(6):543 – 550, 2015. Lasers in Optics.

[40] Adela Marian, Matthew C. Stowe, Daniel Felinto, and Jun Ye. Direct frequency comb measurements of absolute optical frequencies and population transfer dynamics. *Phys. Rev. Lett.*, 95:023001, Jul 2005.

[41] D. McGloin, M. H. Dunn, and D. J. Fulton. Polarization effects in electromagnetically induced transparency. *Phys. Rev. A*, 62:053802, Oct 2000.

[42] Nobel Media. "hans g. dehmelt - biographical", 2014.

[43] T. Meijer, J. D. White, B. Smeets, M. Jeppesen, and R. E. Scholten. Blue five-level frequency-upconversion system in rubidium. *Opt. Lett.*, 31(7):1002–1004, Apr 2006.

[44] H.J. Metcalf and P. van der Straten. *Laser Cooling and Trapping*. Graduate Texts in Contemporary Physics. Springer New York, 2001.

[45] Cristian Adán Mojica Casique. Control digital de los láseres de enfriamiento y atrapamiento utilizados en una trampa magneto-óptica. Master's thesis, Posgrado en Ciencias (Física), 2011.

[46] Han Seb Moon and Heung-Ryoul Noh. Polarization dependence of double-resonance optical pumping and electromagnetically induced transparency in the $5S_{1/2} - 5P_{3/2} - 5D_{5/2}$ transition of ^{87}rb atoms. *Phys. Rev. A*, 84:033821, Sep 2011.

[47] Willis E. Lamb Murray Sargend III, Malan O. Scully. *Laser Physics*. Addison-Wesley Publishing Company, first edition, 1978.

[48] Wolfgang Paul. Electromagnetic traps for charged and neutral particles. *Rev. Mod. Phys.*, 62:531–540, Jul 1990.

[49] Wolfgang Paul and Helmut Steinwedel. Ein neues massenspektrometer ohne magnetfeld. *Zeitschrift für Naturforschung A*, pages 448–450, 1946.

[50] C P Pearman, C S Adams, S G Cox, P F Griffin, D A Smith, and I G Hughes. Polarization spectroscopy of a closed atomic transition: applications to laser frequency locking. *Journal of Physics B: Atomic, Molecular and Optical Physics*, 35(24):5141, 2002.

[51] N. Bohr Dr. phil. I. on the constitution of atoms and molecules. *Philosophical Magazine Series 6*, 26(151):1–25, 1913.

[52] N. Bohr Dr. phil. Xxxvii. on the constitution of atoms and molecules. *Philosophical Magazine Series 6*, 26(153):476–502, 1913.

[53] William H. Press, Saul A. Teukolsky, William T. Vetterling, and Brian P. Flannery. *Numerical Recipes 3rd Edition: The Art of Scientific Computing*. Cambridge University Press, New York, NY, USA, 3 edition, 2007.

[54] E. L. Raab, M. Prentiss, Alex Cable, Steven Chu, and D. E. Pritchard. Trapping of neutral sodium atoms with radiation pressure. *Phys. Rev. Lett.*, 59:2631–2634, Dec 1987.

[55] R. K. Rew and G. P. Davis. "netcdf: An interface for scientific data access". *IEEE Computer Graphics and Applications*, 10:76–82, Jul 1990.

[56] Simon Rochester. Atomic Density Matrix package for Mathematica. http://rochesterscientific.com/ADM/.

[57] R. E. Ryan, L. A. Westling, and H. J. Metcalf. Two-photon spectroscopy in rubidium with a diode laser. *J. Opt. Soc. Am. B*, 10(9):1643–1648, Sep 1993.

[58] M. S. Safronova, Carl J. Williams, and Charles W. Clark. Relativistic many-body calculations of electric-dipole matrix elements, lifetimes, and polarizabilities in rubidium. *Phys. Rev. A*, 69:022509, Feb 2004.

[59] S. Sanguinetti, E. Murè, and P. Minguzzi. Detection of a two-photon transition by stimulated emission: Amplification and circular birefringence. *Phys. Rev. A*, 75:023408, Feb 2007.

[60] J. E. Sansonetti. Wavelengths, transition probabilities, and energy levels for the spectra of rubidium rb i through rb xxxvii. *National Institute of Standards and Technology, Gaithersburg, MD*, 20899, 2005.

[61] José Ricardo Santillán Díaz. Caracterización de la trampa magneto-óptica del instituto de ciencias nucleares de la unam. Master's thesis, Posgrado en Ciencias (Física), 2015.

[62] A. L. Schawlow and C. H. Townes. Infrared and optical masers. *Phys. Rev.*, 112:1940–1949, Dec 1958.

[63] D. Sesko, C. G. Fan, and C. E. Wieman. Production of a cold atomic vapor using diode-laser cooling. *J. Opt. Soc. Am. B*, 5(6):1225–1227, Jun 1988.

[64] D. Sheng, A. Pérez Galván, and L. A. Orozco. Lifetime measurements of the $5d$ states of rubidium. *Phys. Rev. A*, 78:062506, Dec 2008.

[65] Bruce W. Shore. *The Theory of Coherent Atomic Excitation*, volume 1, 2. John Wiley & Sons, 1990.

[66] Paul Siddons, Charles S Adams, Chang Ge, and Ifan G Hughes. Absolute absorption on rubidium d lines: comparison between theory and experiment. *Journal of Physics B: Atomic, Molecular and Optical Physics*, 41(15):155004, 2008.

[67] P. W. Smith and R. Hänsch. Cross-relaxation effects in the saturation of the 6328-å neon-laser line. *Phys. Rev. Lett.*, 26:740–743, Mar 1971.

[68] D Touahri, O Acef, A Clairon, J.-J Zondy, R Felder, L Hilico, B de Beauvoir, F Biraben, and F Nez. Frequency measurement of the 5s12(f = 3)-5d52(f = 5) two-photon transition in rubidium. *Optics Communications*, 133(1-6):471 – 478, 1997.

[69] S. van der Walt, S. C. Colbert, and G. Varoquaux. The numpy array: A structure for efficient numerical computation. *Computing in Science Engineering*, 13(2):22–30, March 2011.

[70] Silvije Vdović, Ticijana Ban, Damir Aumiler, and Goran Pichler. *EIT* at transition in a mismatched v-type rubidium system. *Optics Communications*, 272(2):407 – 413, 2007.

[71] Andrejs Vorozcovs, Matthew Weel, Scott Beattie, Saviour Cauchi, and A. Kumarakrishnan. Measurements of temperature scaling laws in an optically dense magneto-optical trap. *J. Opt. Soc. Am. B*, 22(5):943–950, May 2005.

[72] C. D. Wallace, T. P. Dinneen, K. Y. N. Tan, A. Kumarakrishnan, P. L. Gould, and J. Javanainen. Measurements of temperature and spring constant in a magneto-optical trap. *J. Opt. Soc. Am. B*, 11(5):703–711, May 1994.

[73] C. Wieman and T. W. Hänsch. Doppler-free laser polarization spectroscopy. *Phys. Rev. Lett.*, 36:1170–1173, May 1976.

[74] William Hyde Wollaston. A method of examining refractive and dispersive powers, by prismatic reflection. *Philosophical Transactions of the Royal Society of London*, 92:365–380, 1802.

[75] Min Xiao, Yong-qing Li, Shao-zheng Jin, and Julio Gea-Banacloche. Measurement of dispersive properties of electromagnetically induced transparency in rubidium atoms. *Phys. Rev. Lett.*, 74:666–669, Jan 1995.

[76] H.-I. Yoo and J.H. Eberly. Dynamical theory of an atom with two or three levels interacting with quantized cavity fields. *Physics Reports*, 118(5):239 – 337, 1985.

[77] Chengjie Zhu, Chaohua Tan, and Guoxiang Huang. Crossover from electromagnetically induced transparency to autler-townes splitting in open v-type molecular systems. *Phys. Rev. A*, 87:043813, Apr 2013.

Index